Characterising rocks dredged from the Gulden Draak microcontinent

Robyn Gardner
Student # 40923258
GEOS899 Research Project
Due: 30th June 2012

MACQUARIE UNIVERSITY GEMOC

STATEMENT OF ORIGINALITY

All the work submitted in this thesis is the original work of the author except were otherwise acknowledged. No part of this thesis has previously been submitted to any other university or institution.

_____ _____

Signed – Robyn Gardner Date

ABSTRACT

Gulden Draak is a bathymetric feature 2-3 kilometres below the surface of the Indian Ocean 2,000 kilometres west of Perth, Western Australia. Four samples were selected from the continental rocks dredged from the knoll, three orthogneisses and one paragneiss. Minerals and textures indicate the samples were subjected to amphibolite to granulite facies metamorphism in multiple metamorphic events. U-Pb and Lu-Hf isotope analysis shows the samples have undergone a complex history of emplacement, metamorphism and partial remelting. The orthogneisses were originally emplaced prior to 2800 Ma, 1290 Ma and 1200 Ma respectively. Two samples, an orthogneiss and the paragneiss have Archaean age zircon cores. These events have been correlated with the Nornalup Complex in the Albany-Fraser Orogen formed as the Mawson and Yilgarn cratons collided. All samples were subsequently impacted by the Kuunga Orogen at ~500Ma: by isotope resetting, zircon partial melting and recrystallisation, growth of new metamorphic rims and/or lead loss. Lead loss evidence for the rifting event at ~136 Ma is also seen. At the time of the Gondwana breakup Gulden Draak was located south of the Naturaliste Plateau very close to the Greater India-Antarctica-Western Australia triple point.

ACKNOWLEDGEMENTS

In any venture such as this research the key to success is being part of a great team that works together: we've had that team every step of the way.

I'd like to thank the Sydney University Earthbyte group for organising the research project and inviting us to join their cruise. The captain and crew of the RV Southern Surveyor did a great job, their skill and patience achieved an amazing haul of rocks on each dredge run. Without them there would be no rocks to investigate. Thanks also to the support team from CSIRO who overcame the logistical and technical difficulties at sea and made the cruise such a success.

A special thanks to my supervisor, Nathan Daczko for his time, patience, insights and boundless enthusiasm without which the research would not have progressed so well. And also a special thanks to Madi who analysed the first Batavia Knoll dredge. We shared the path as we collected the rocks and worked in parallel on our rocks on our return - we made a great team.

Also, thanks to the support staff at the Geochemical Analysis Unit within the GEMOC (the ARC National Key Centre for Geochemical Evolution and Metallogeny of Continents) facility at Macquarie University: Manal for thin sections, Peter for whole rock analysis, Steve for selFrag support, Kevin for the EMP, Will for the U-Pb and Norm for his general oversight and Lu-Hf analyses - I learnt a huge amount, and really appreciate the time you spent explaining the processes to me.

I'd also like to say a general thanks to the staff of the Department of Earth and Planetary Sciences at Macquarie University. The passion shown by the lecturers, particularly Tracy, Dick, Kelsie, Nathan, Simon and Sandra inspired me (and many others I know) to continue my studies.

And of course thanks to my family and friends who have all been putting up with my rock stories and have been very supportive all along the way - without you I wouldn't be here today.

TABLE OF CONTENTS

LIST OF FIGURES

LIST OF TABLES

CHAPTER 1: INTRODUCTION

The bathymetry of the Indian Ocean holds many clues for the movement northward of Greater India (Figure 1-1). The Perth Abyssal Plain is one area which has only a small number of magnetometer cruise tracks and the submerged knolls of Gulden Draak and Batavia have never been closely investigated. The cruise of the RV Southern Surveyor in October/November 2011 (ss2011_06) remedied this situation.

The Earthbyte group from Sydney University have been researching the rifting events occurring during the breakup of Gondwana for a number of years, including the pre-breakup configuration of the continents and the size of Greater India prior to the collision and subduction events forming the Himalayan mountains.

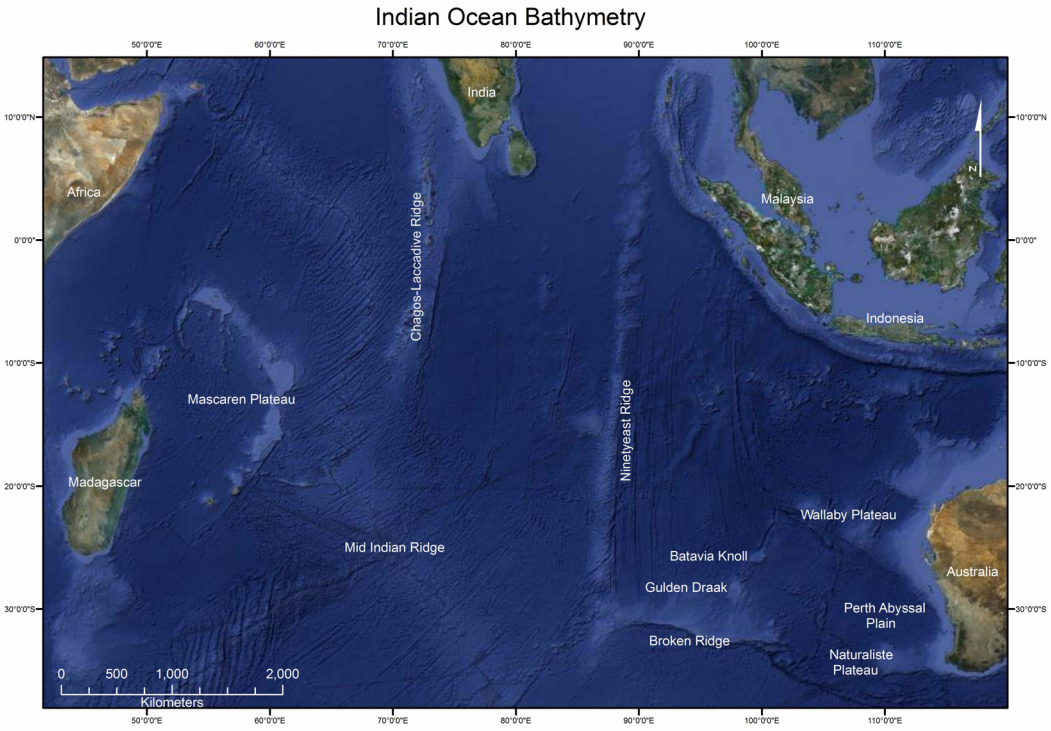

Figure 1-1: Indian Ocean bathymetry and location of Gulden Draak (Google Earth, 2012)

1.1 BACKGROUND

The purpose of the cruise was primarily to gather magnetic anomaly data perpendicular to the spreading ridge to determine the chronology of the oceanic crust development in the Perth Abyssal Plain. In addition dredging of rocks from Batavia Knoll, Gulden Draak and Dirk Hartog Ridge was undertaken to determine the oceanic or continental nature of the bathymetry features. Figure 1-2 shows the ships track of the voyage. Approximately 3.000 km of magnetometer data was collected during the voyage.

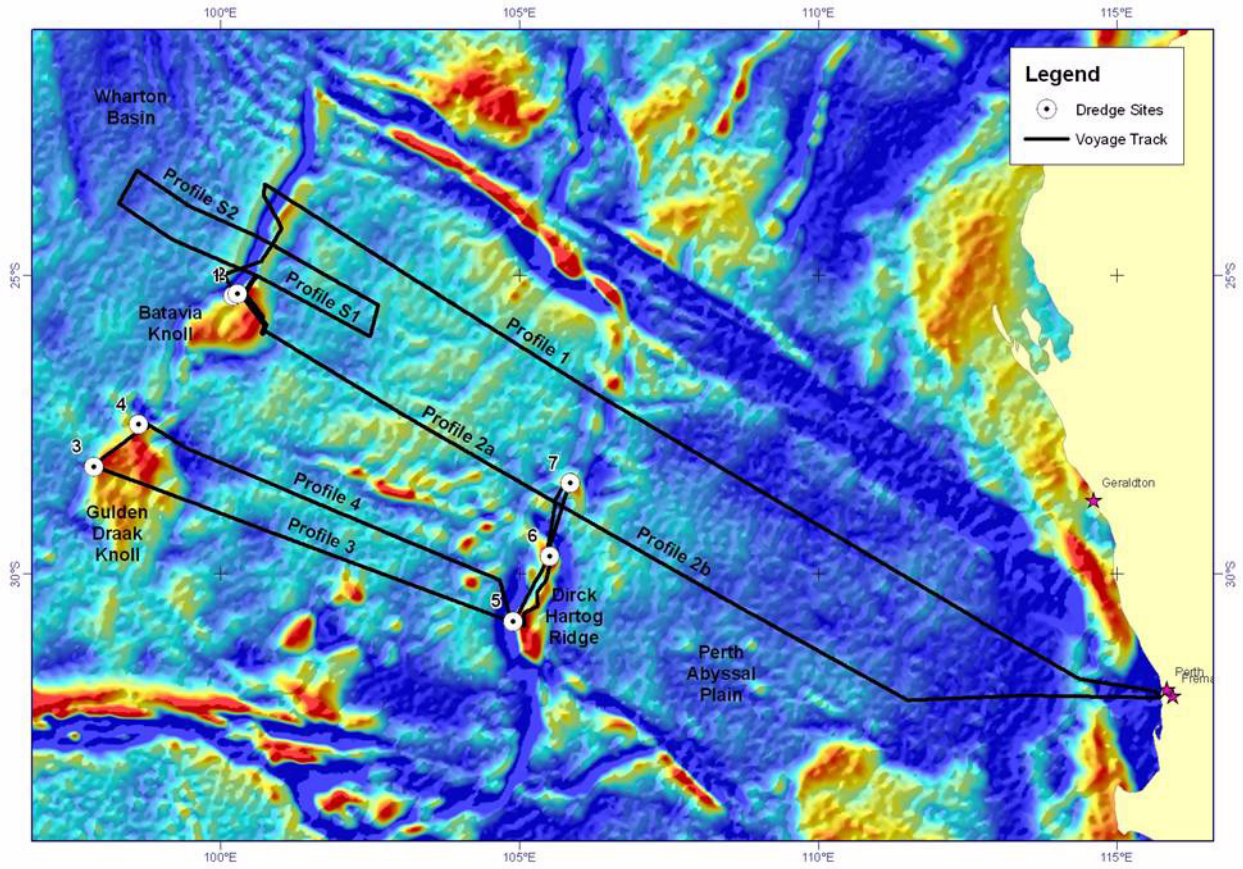

Figure 1-2: Gravity map of south eastern Indian Ocean showing the voyage track and dredge sites (Williams, 2012)

With the first look at the rocks from the dredges on Batavia Knoll and Gulden Draak it was immediately evident that both knolls were continental crust. This paper investigates the rocks from the first dredge run on Gulden Draak which was the third of the cruise.

1.2 RESEARCH PAPER OVERVIEW

This chapter serves to introduce the general area of research, background and aims of the cruise. Chapter 2 gives a brief overview of the complex geological history relevant to the dredged rocks and the location of Gulden Draak, with Chapter 3 providing more details of the dredging location and processes.

Chapter 4 starts the investigation of the rock samples with a petrographic description of the samples concentrating on the minerals present: their texture and modes. All samples are metamorphic. Chapter 5 further elucidates the mineralogy of the samples using electron microprobe (EMP) analysis and allows some conclusions to be made on the formation conditions of the rocks. In contrast, Chapter 6 investigates the whole rock chemistry of the major and minor elements, allowing classification of the protolith of the samples.

Chapter 7 begins the analysis of the zircons in the samples by grouping the zircons by morphology and investigating their chemistry via EMP analysis. Zones within the zircons are investigated to determine the zircon history using U-Pb isotope systematics in Chapter

8 and Lu-Hf isotope systematics in Chapter 9. This is used in conjunction with the knowledge gained in the previous chapters to infer a history for each sample.

An overall summary of the geochronology is included Chapter 10 with correlation of the samples to the geohistory from Chapter 2 and the implications of this for the amalgamation and breakup of Gondwana.

CHAPTER 2: REGIONAL GEOLOGY

In this chapter the geological history of the area of south Western Australia, Antarctica and India is reviewed to give some background to the origin of the rocks dredged from Gulden Draak. The complex history discussed here is reflected in the complexities of the rock samples investigated.

2.1 GEOHISTORY

The western and southern edges of Australia have undergone a complex series of tectonic events involving the collision of the Archaean Yilgarn, Pilbara and Gawler terranes of south and western Australia with the Mawson in East Antarctica and the Dharwar craton in India to form the supercontinents of Rodinia and Gondwana.

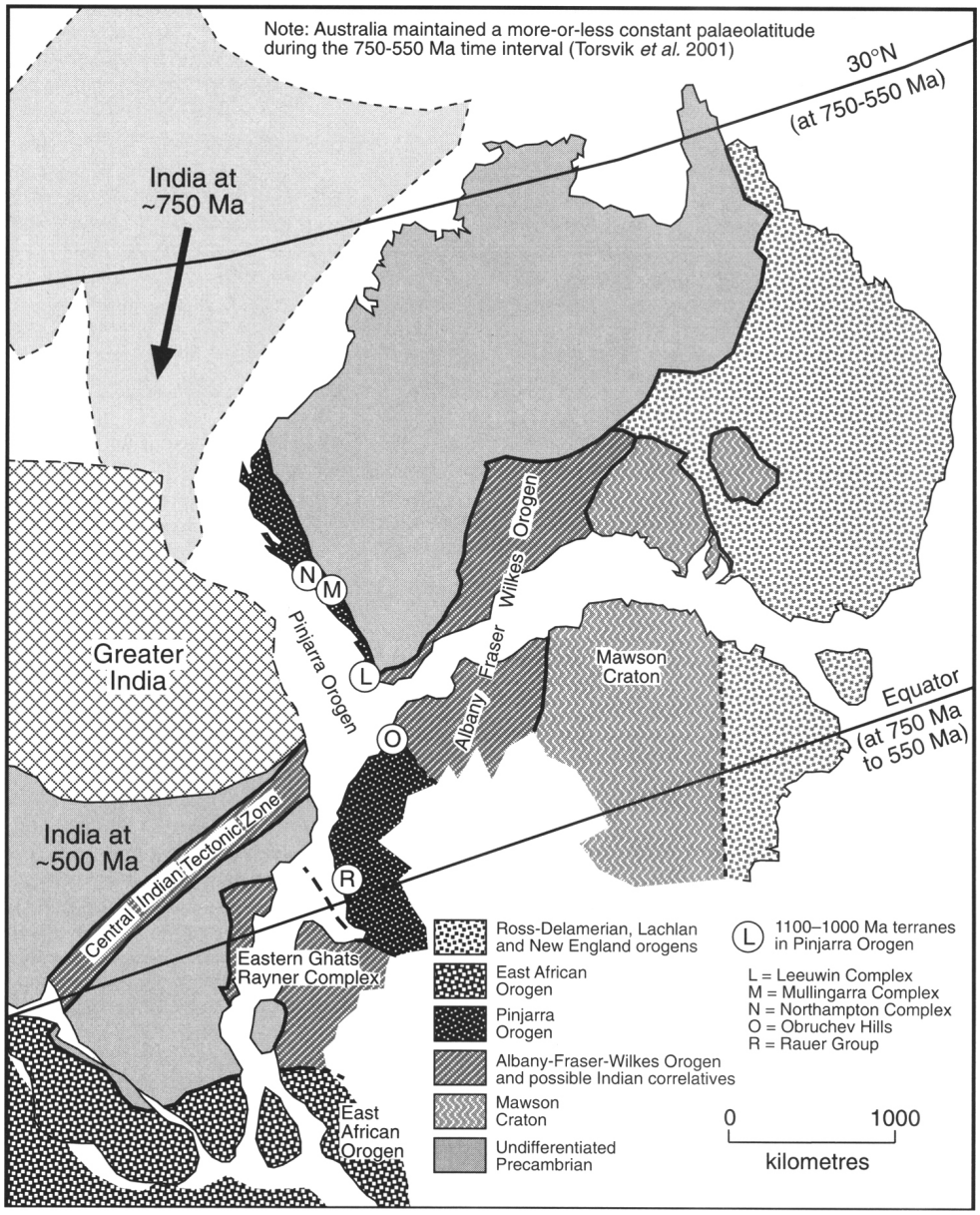

Figure 2-1: Mesoproterozoic orogen correlation for eastern Gondwana (Fitzsimons, 2003, Figure 11)

As the cratons collide orogenic belts are formed. The subsequent breakup of Gondwana has meant the orogens need to be correlated between the currently existing land masses (Figure 2-1).

2.1.1 Albany-Fraser complex

During the Mesoproterozoic the Mawson and Yilgarn cratons collided forming the Albany-Fraser Orogen (Figure 2-2) (Fitzsimons, 2003). The remnants of three main belts within the orogen can be seen on the southern Western Australian coast. The orogen is truncated to the west by the Pinjarra Orogen at the Darling Fault.

The first of the belts, the Biranup complex, is in faulted contact with the Yilgarn craton and could be either reworked Yilgarn craton or a series of accreted terranes (Nelson et al., 1995). It is dominated by interleaved felsic orthogneisses which have undergone granulite facies metamorphism of ages in the ranges 2700-2600 Ma, 1700-1600 Ma and ~1300 Ma (Nelson et al., 1995).

The Fraser complex is the second of the belts and is a number of meta-gabbro and pyroxene granulite slices formed ~1300 Ma in an oceanic arc subduction zone (Fitzsimons, 2003).

The third main belt is the Nornalup complex which is considered by Boger (2011) to be the leading edge of the Mawson craton. It is dominated by Recherche granite formed ~1300 Ma which has intruded into sedimentary units now visible as psammitic and pelitic paragneisses, thought to be similar to the Malcolm Gneiss found to the south of the Nornalup complex which has detrital zircon populations from 2750 to 2020 Ma (Fitzsimons, 2003).

Two stages of tectonism is thought to have occurred in the Nornalup complex. The first, associated with granulite facies metamorphism 1345 to 1260 Ma and the second, associated with amphibolite facies metamorphism from 1215 to 1140 Ma. The Mount Ragged metasediments were deformed by the second stage of metamorphism, so are thought to have been deposited over the Recherche granites, between the two stages (Clark et al., 2000).

Halpin et al., (2008) correlate the southern margin of the Naturalise Plateau with the Albany-Fraser Orogen. The orogen is also thought to extend into Eastern Antarctica with correlations of the Nornalup Complex to the Windmill Islands and of the Biranup Complex to Bunger Hills (Duebendorfer, 2002, Fitzsimons 2003). The extension of the Albany-Fraser into the Central Indian Tectonic Zone as suggested by Fitzsimons in Figure 2-1 is not substantiated by recent geochonology work on the granulite belts by Vansutre and Hari (2010).

2.1.2 Pinjarra Orogen

To avoid confusion of terminology, the use of ‘Pinjarra Orogen’ in this paper, refers to the tectonic events from approximately 1080 to 900 Ma. The Darling Fault (Figure 2-2) defines the eastern edge of the Pinjarra Orogen which extends up the Western Australian coast for approximately 1,500 km (Fitzsimons, 2003). Today it is largely covered by sedimentary basin rocks, with relatively small outcrops including the Leeuwin complex, but is believed to have divided East Gondwana in two during the Mesoproterozoic (Fitzsimons, 2003). The cause of the Pinjarra Orogen is contentious with Fitzsimons (2003) suggesting the terranes seen are allochthonous, while Boger (2011) suggests it is a collisional orogeny, though of

which cratons is unknown. The orogen is associated with granulite facies metamorphism and is dated from 1080 Ma to 1060 Ma with igneous intrusions occurring until approximately 900 Ma (Boger, 2011).

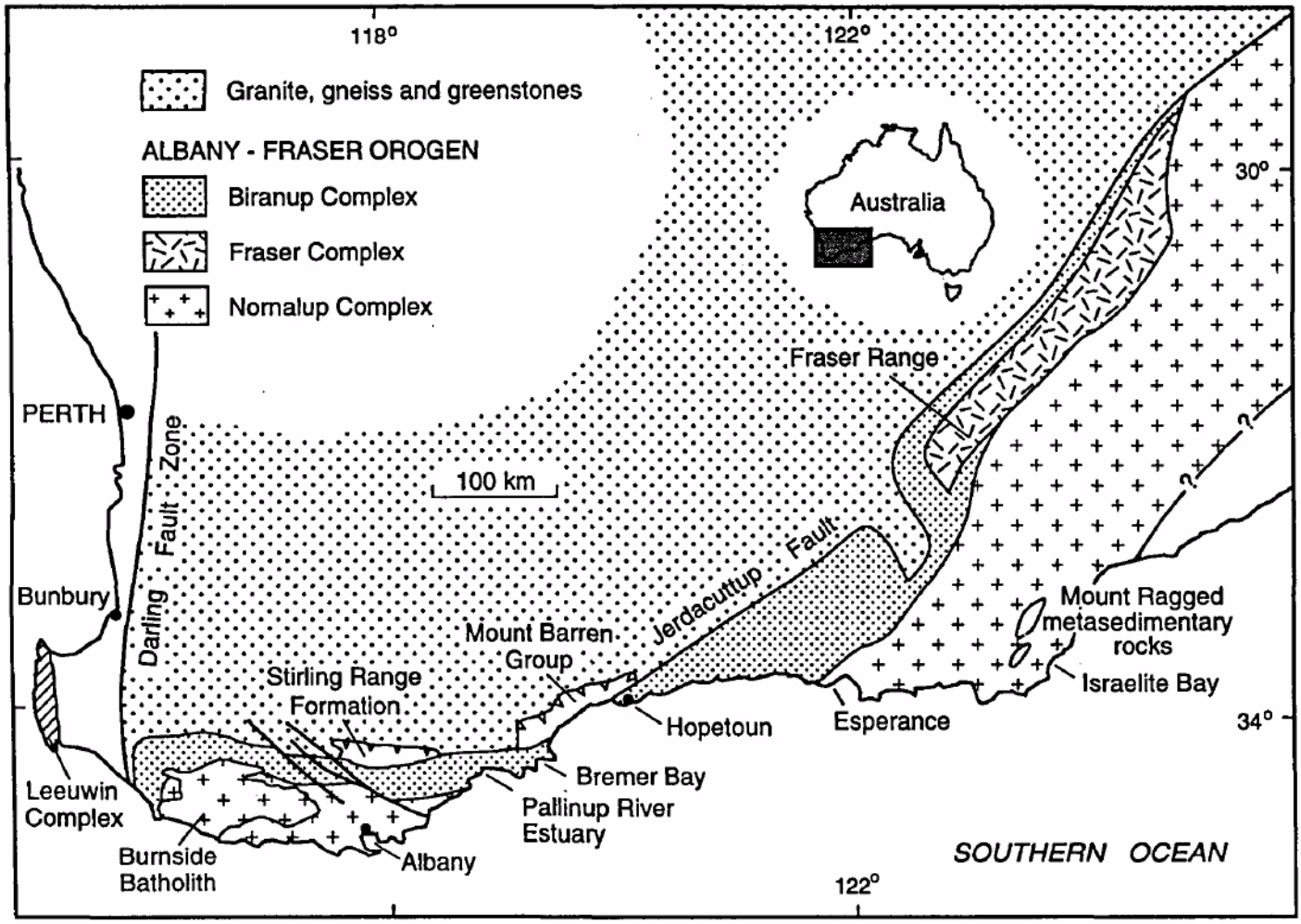

Figure 2-2: Albany-Fraser Orogen (Nelson et al., 1995 Figure 1)

Boger (2011) correlates the Pinjarra Orogen with Obruchev Hills situated between the Scott and Denman glaciers in Antarctica, while Halpin et al., (2005) report Pinjarra Orogen ages for reworked Archaean continental crust from the Rayner complex.

The Eastern Ghats area of India also displays reworked continental crust of Pinjarra Orogen age (Dobmeier & Raith, 2003), and is generally correlated with the Rayner Complex in Antarctica (Fitzsimons, 2003, Halpin et al., 2005) (Figure 2-1). The extent of Greater India close to the West Australian coast is a topic of current debate due to the complexities of unravelling the collision of the Greater Indian continent with Eurasia (Müller, 2010).

2.1.3 Kuunga Orogen

Meert (2002) has suggested that the amalgamation of eastern Gondwana resulted from a series of tectonic collisions starting with the East Africa Orogen from approximately 750Ma and ending with the Kuunga Orogen which lasted from 570 to 530 Ma (Figure 2-3). The Kuunga Orogen reactivated the Pinjarra Orogen, including the Darling Fault along the

eastern edge, resetting isotopes and causing zircon and monazite regrowth to different degrees depending on location across the orogen (Meert, 2002).

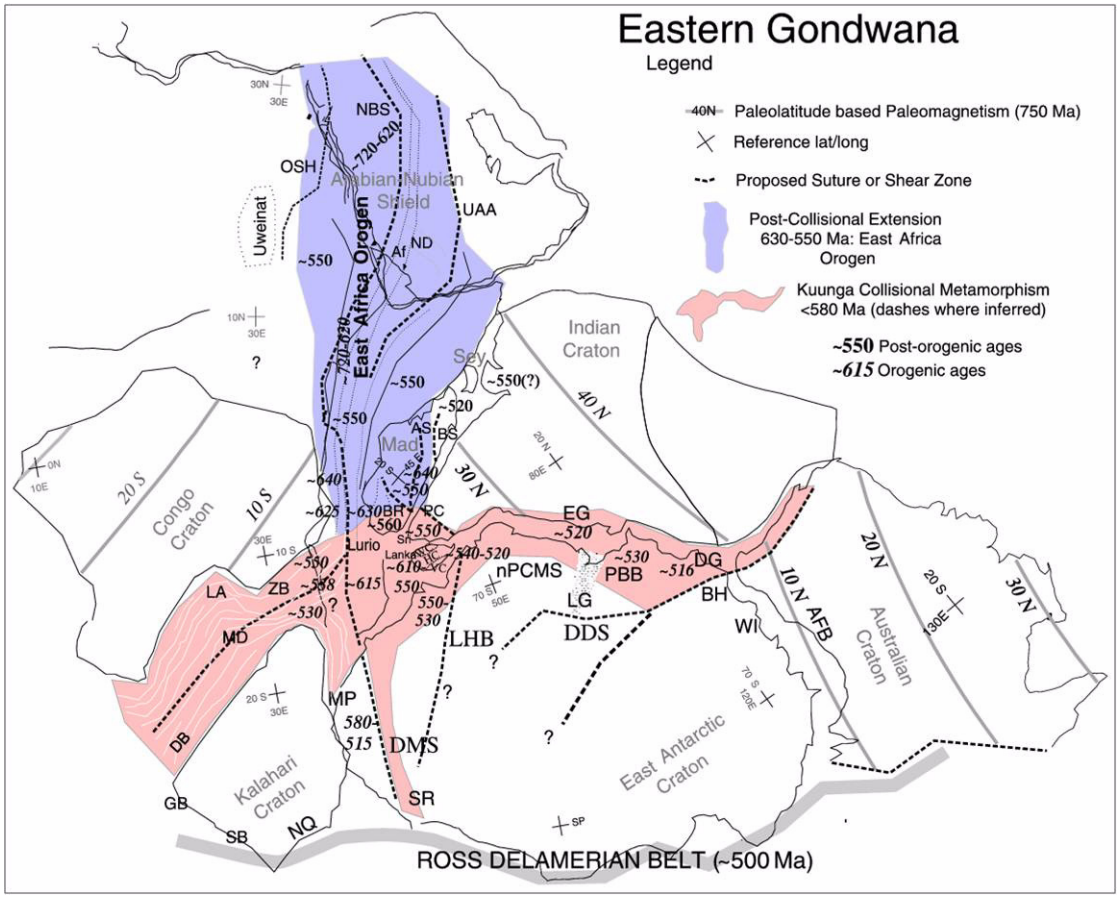

Figure 2-3: Kuunga Orogen: eastern Gondwana amalgamation (Meert, 2002 Figure 10) Abbreviations per Table Appx-1

Chatterjee et al. (2007) dated two sites in the Shillong-Meghalaya gneissic complex (SMGC) in north eastern India. Sonapahar to the east of the Nongchram Fault has ages of approximately 500 Ma, which they correlate with Prydz Bay in the Antarctic while the Garo-Goalpara Hills rocks, west of the fault are less deformed and give much older ages, around 1600 Ma. Chatterjee et al., (2007) suggest the Nongchram Fault correlates with the western edge of the suture formed during the Pinjarra Orogen which was reactivated during the Kuunga orogen.

2.1.4 Gondwana breakup

In the Gibbons et al. (2012) reconstruction of the breakup of Gondwana, reproduced in Figure 2-4 (Gibbons et al., 2012 Figure 5b), Gulden Draak originally resided to the south of the Naturaliste Plateau connected to Greater India which started rifting off the Perth margin from 136 Ma. It was rifted to its current location by a spreading ridge located at the Dirk Hartog Ridge (red-brown line in Figure 2-4) and was transferred back to the Australian plate during a ridge jump estimated by Gibbons et al. (2012) to have occurred ~108 Ma.

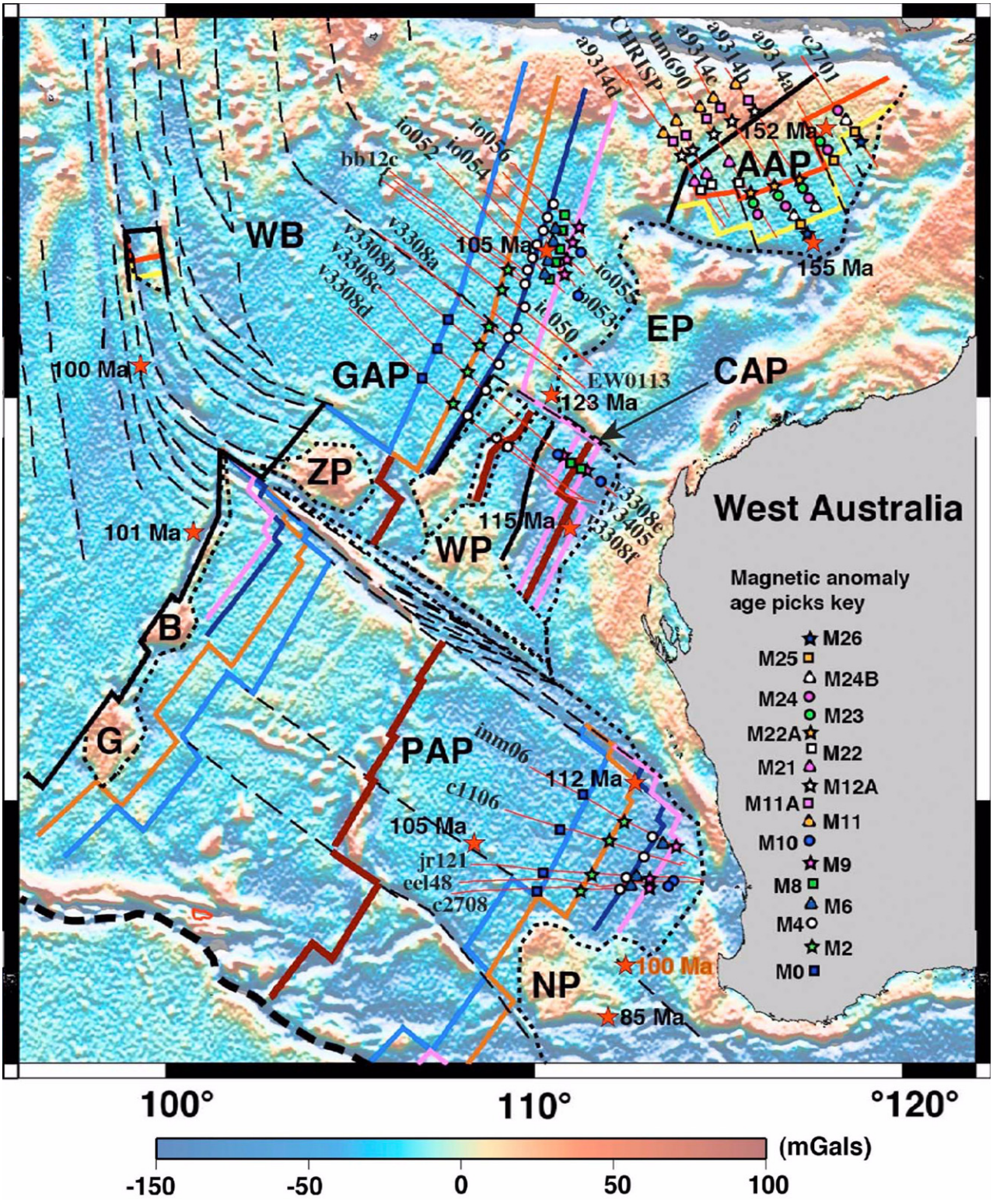

Figure 2-4: East Gondwana rifting model with isochrons and ships tracks on free air gravity field. For full details see Gibbons et al. (2012, Figure 5b) Abbreviations in Table Appx-2

CHAPTER 3: FIELDWORK

The samples were collected as part of a three week cruise on the R.V. Southern Surveyor departing Fremantle on 20th October 2011 and returning 9th November 2011 (ss2011-v06). The R.V. Southern Surveyor was run by CSIRO on behalf of the National Maritime Facility. Dredged samples were taken at two locations each on Batavia Knoll and Gulden Draak (Figure 3-1) and three locations along Dirk Hartog Ridge (Figure 1-2).

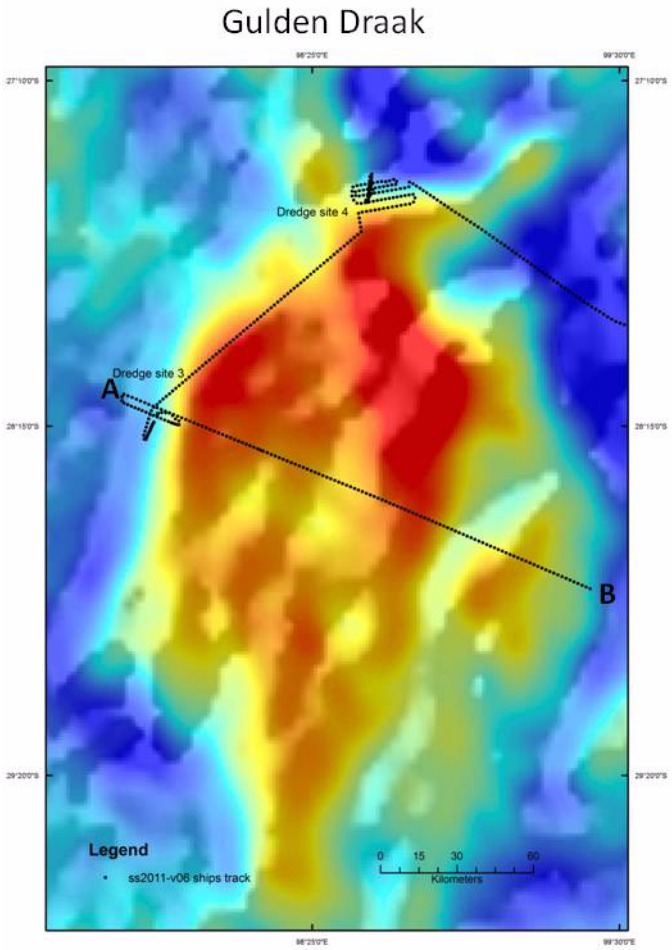

Figure 3-1: Gravity map of Gulden Draak showing ships track. A-B: profile in Figure 3-2 (Williams, 2012)

The eastern side of Gulden Draak was found to have a smooth profile (Figure 3-2) which is unsuitable for dredging. The steeper bathymetry on the western side was swath mapped for potential dredging sites by CSIRO staff (Tara Martin) using a Simrad EM300 multibeam echo sounder and Seafloor Information System software. The dredge site was selected where the sea floor was less than 3,000m under the ocean surface and the dredge could be dragged up a slope, while the ship headed into the wind at very low speed, approximately 1 knot (Figure 3-3). For the first Gulden Draak dredge run the dredge was run out on 3,500 meters of cable and dragged between 28 17.251 S 97.52.078 E and 28 15.092S 97 51.048E on a heading of 191^{o} from a depth of 2800m to 2500m.

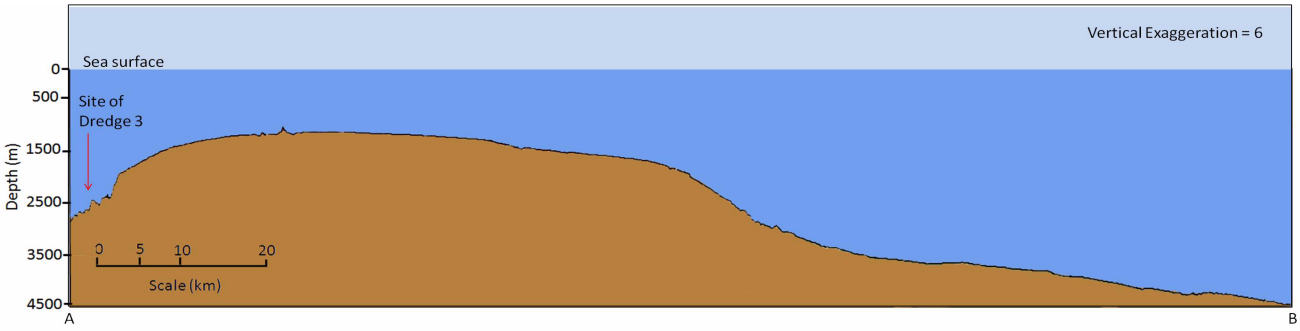

Figure 3-2: Gulden Draak profile (produced from Caris© output)

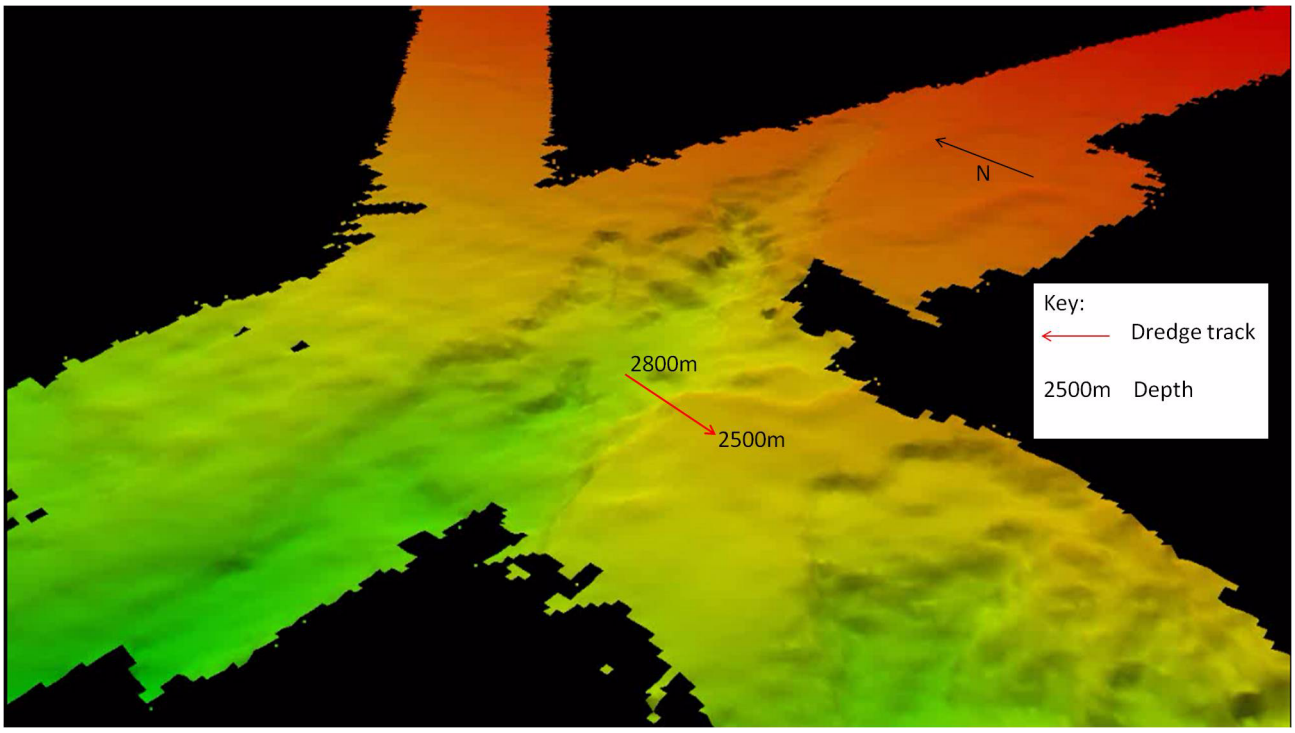

Figure 3-3: Dredge site 3 on Gulden Draak, modified from Caris© output (Martin, 2011)

Once the dredge was retrieved, the rocks in the dredge basket were sorted on the benches in the ship's wet laboratory. The cobbles, boulders and fresh samples were cut using the on-board rock saw and examined. The samples were labelled, photographed and stored for shipment. Twenty six samples from dredge 3 were kept, ranging from granite gneisses (DR3-1, DR3-2 and DR3-6) and those interpreted as Gondwana basement rocks (DR3-15) to sandstones (DR3-18 to 26) and altered basalts (DR3-12 and DR3-13). A full list of the samples from dredge 3 is included in Appendix B.

Field relationships for the rocks retrieved cannot be determined, however, the swath data (Figure 3-3) shows the area has similar features to a gully on land and that the dredge was dragged up the side of the gully.

CHAPTER 4: PETROGRAPHY

This chapter examines the hand samples and thin sections of five selected samples to do the initial determination of the rock type, make comparisons between the samples and make suggestions for the protolith and metamorphism experienced by each sample. This information is used as input to subsequent analysis in the following chapters.

4.1 METHOD

The Twenty six samples kept from the first Gulden Draak dredge run were initially cut using the rock saw on board the RV Southern Surveyor. The most interesting samples, likely to provide good analysis candidates were selected. Ten polished thin sections were made at the Geochemical Analysis Unit (GAU) in the Earth and Planetary Sciences Department within Macquarie University, Sydney Australia. The sedimentary samples (sandstones and siltstones) and altered basalts were not thin sectioned. The thin sections were examined on a petrographic microscope. Five of the ten thin sectioned samples were selected for detailed analysis.

4.2 RESULTS

4.2.1 DR3-1: Two feldspar-quartz orthogneiss

The DR3-1 sample is a rounded boulder of approximately 40cm diameter coated in a thin layer of dark mineral we have taken to be manganese (Mn). It has bands of coarse and fine crystals (Figure 4-1 A).

Figure 4-1: Hand samples of DR3-1 (A), DR3-2 (B) and DR3-6 (C) (coin is 31mm) (Halpin, 2011)

The band of large crystals (Figure 4-2, slide is slightly thicker than 30μm) has a mode of 50% K-feldspar, 40% quartz, 5% plagioclase and 5% opaques. The plagioclase is seen predominantly in perthitic intergrowths in host K-feldspar crystals. Approximately 10% of the K-feldspar is microcline, that is, has a tartan texture under XPL. The K-feldspar crystals are up to 4mm with curved or irregular shapes, with some displaying plagioclase films. The quartz grains are up to 2.5mm with polygonal to irregular shapes. Some of the quartz grains display undulose extinction and have subgrains. The opaques are bright grey under reflected light and are up to 2.5mm.

The transition between the fine and coarse bands is abrupt, however, the crystals are interlocking. In the finer grained band there is slightly more quartz (at mode 42%) and opaques (at mode 6%) than in the larger crystal band. K-feldspar and plagioclase are slightly reduced at modes 48% and 4% respectively, but still form perthitic textures. The quartz and feldspar crystals are much smaller at up to 0.5mm and the opaques are up to 0.25mm.

Minor zircon, apatite and epidote are also found in the thin section, but there is no evidence of any micas or any mafic minerals.

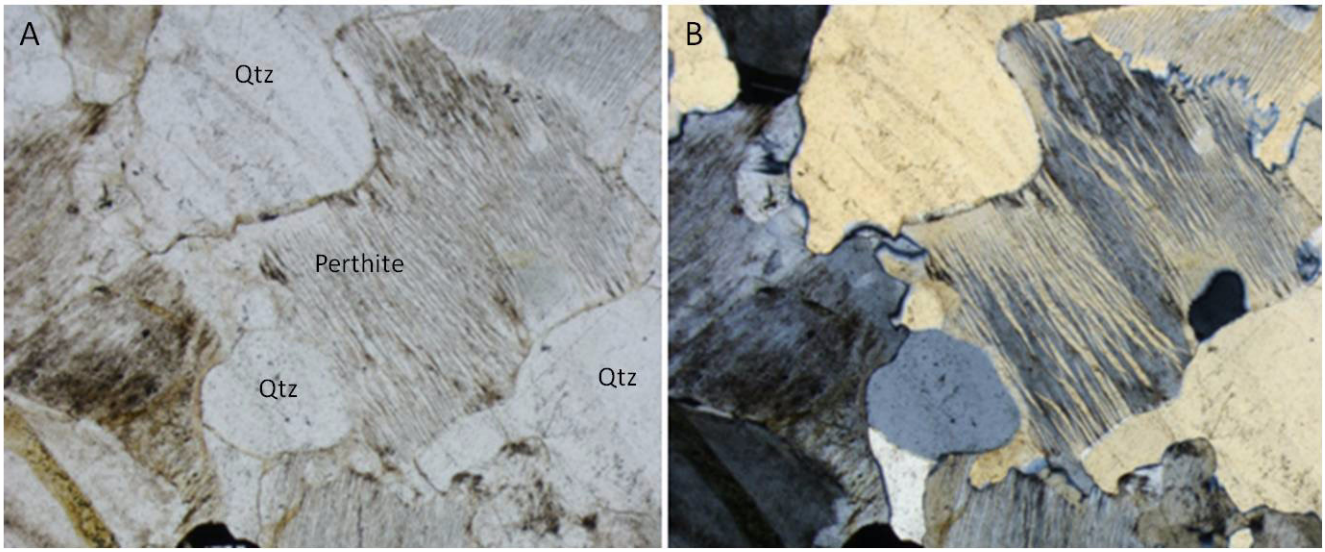

Figure 4-2: Sample DR3-1 thin section showing perthitic textures A: PPL, B:XPL; FOV 1.5mm (abbreviations per Table Appx-3)

4.2.2 DR3-2: Quartz-feldspar-biotite orthogneiss

Sample DR3-2 is a rounded slab 24 cm wide, 8 cm deep and approximately 40cm long with Mn more heavily deposited on one side and an 8cm edge showing a fresh face where it has been broken from the outcrop during dredging (Figure 4-1B). The sample has horizontal internal alteration planes. The mode of the sample is 40% plagioclase, 25% quartz, 24% K-feldspar, 10% biotite and 1% opaques with minor zircons and monazite. The plagioclase forms polygonal to irregular crystals to 2.5mm and appears as exsolution inclusions in K-feldspar. Much of the plagioclase is being altered to sericite (fine grained muscovite) (Figure 4-3). The process has proceeded almost to completion in some crystals. The K-feldspar appears as crystals with irregular boundaries, but these are smaller, to 1mm and are mostly microcline. The quartz crystals also have polygonal to irregular boundaries. The crystals are up to 3mm and show distinct subgrains and undulose extinction. There are minor

myrmekites of quartz and plagioclase. The biotite is subhedral to 0.3mm with much of it being altered to chlorite.

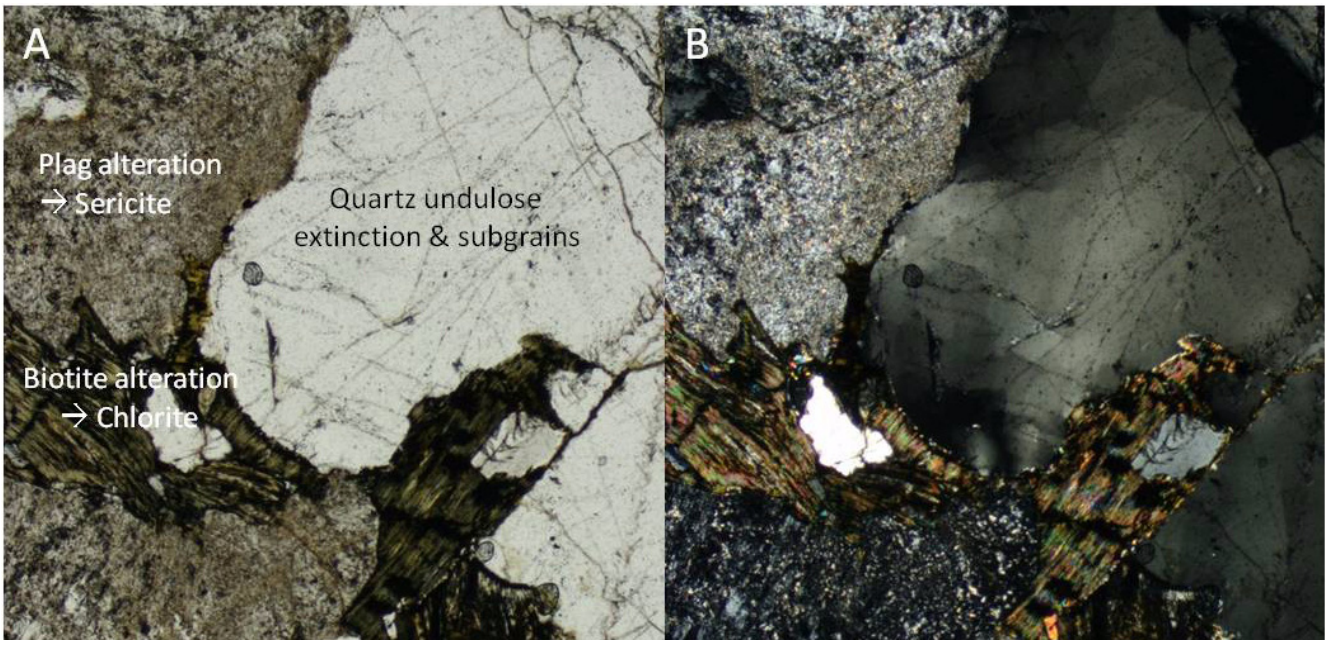

Figure 4-3: Sample DR3-2 thin section showing biotite and plagioclase alteration and quartz undulose extinction A: PPL, B:XPL; FOV 1.5mm

4.2.3 DR3-6: Two feldspar-quartz orthogneiss

Sample DR3-6 is a rounded cobble of approximately 20cm diameter (Figure 4-1C) with a thin layer of Mn deposition. It has a mode of 43% K-feldspar, 40% quartz, 10% plagioclase 7% opaques with minor accessory minerals of zircon and apatite (Figure 4-4).

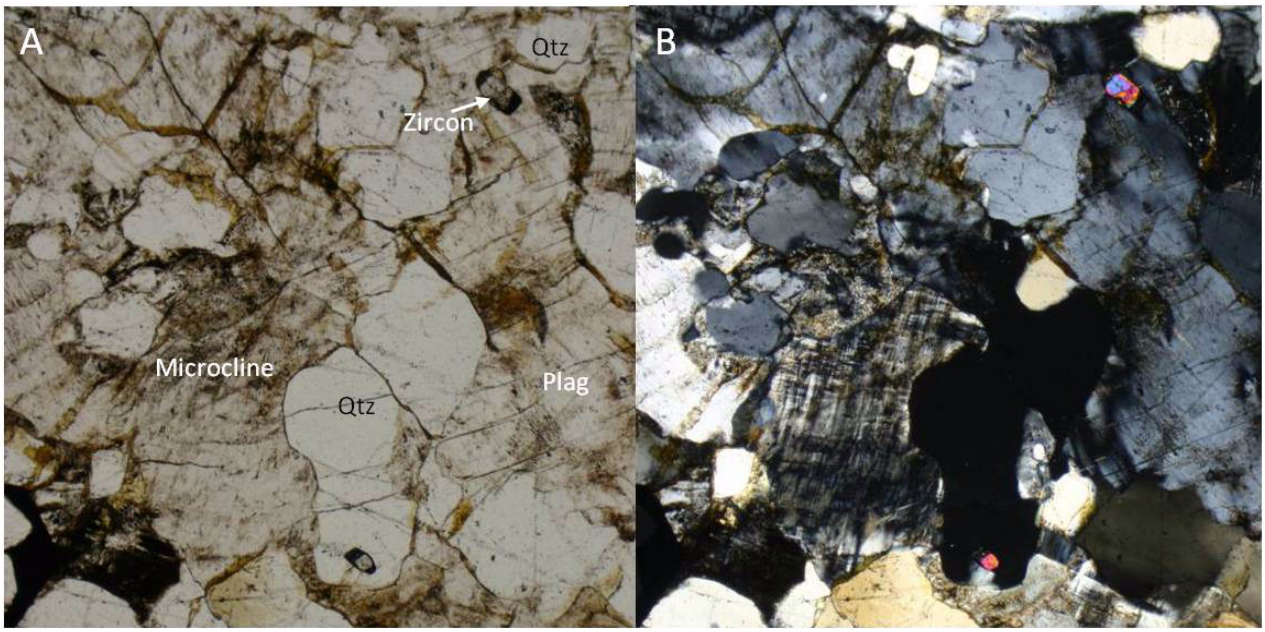

Figure 4-4: Sample DR3-6 thin section showing microcline K-feldspar A: PPL, B:XPL; FOV 1.5mm

The foliation in the samples is defined by linear aggregations of quartz and feldspar crystals. The quartz crystals are irregular to polygonal in shape, up to 5mm and display undulose extinction and subgrain boundaries. A small number of quartz and feldspar crystals have tight dihedral angles. K-feldspar, as microcline, is up to 5mm, displays irregular to polygonal shapes and has flame structures of plagioclase and inclusions of exsolution plagioclase and quartz (Figure 4-5). Plagioclase is seen mostly as flames and intergrowths with K-feldspar, however, where it was discrete crystals and inclusions of up to 1mm these are in the process of being altered to sericite. There are minor occurrences of myrmekite intergrowths of quartz with plagioclase. The opaques are up to 1mm and define the foliation in the sample. They appear in the interstitial spaces between the other minerals.

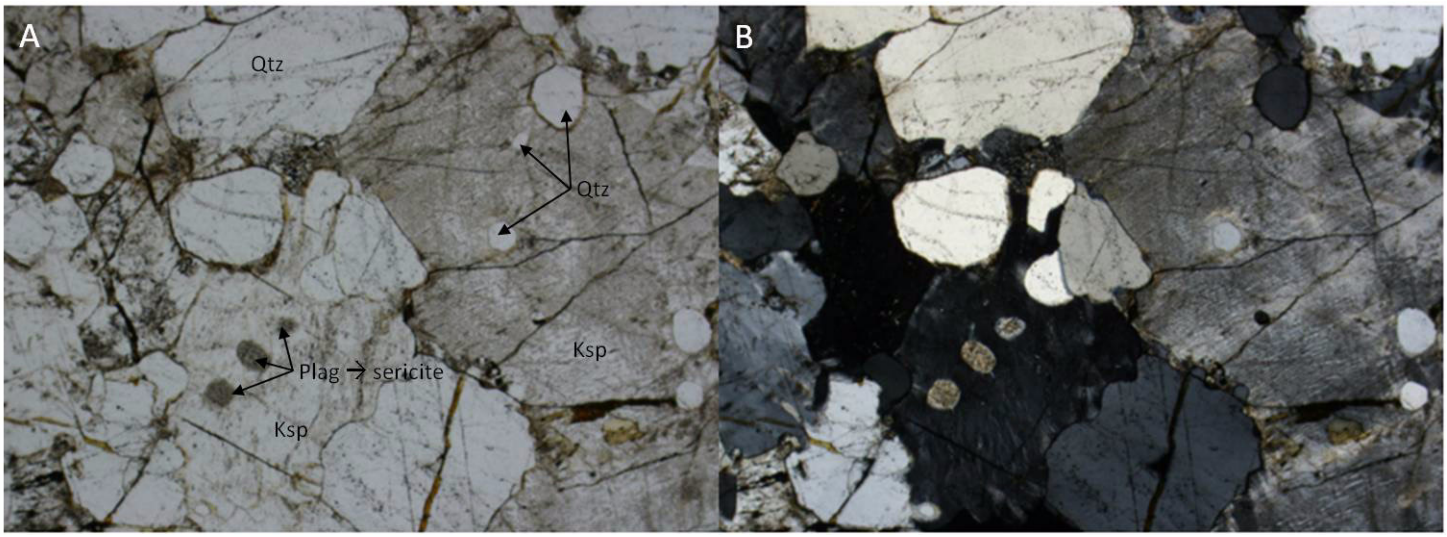

Figure 4-5: Sample DR3-6 thin section showing circular quartz and plagioclase in K-feldspar A: PPL, B:XPL; FOV 2mm

4.2.4 DR3-15: Garnet-sillimanite-biotite paragneiss

Sample DR3-15 is a large block approximately 1m wide which has Mn deposited on all sides except for one fresh face where it was broken from the outcrop during dredging. It has been subsequently sawn into pieces (Figure 4-6A). Many crystals of garnet to 5 mm are visible in the hand sample, and weathering can be seen throughout the rock.

The mode of the sample is 30% quartz, 25% plagioclase, 15% pinite, 12% garnet, 12% K-feldspar, 5% biotite, and 1% opaques with minor zircon, monazite and sillimanite. Poikiloblasts of subhedral pink garnets to 5mm have armoured relict inclusions of quartz, plagioclase, biotite and opaques. Larger inclusions are in a band towards the edge of the garnet (Figure 4-7). The foliation is defined by an isotropic replacement texture of pinite (mica and clay minerals) associated with the garnets which forms long undulating strings through the sample (Figure 4-7). Veins of pinite and sericite also occur throughout the sample. Within the pinite are some residual sillimanite crystals (Figure 4-8). On the edge of the pinite, quartz and plagioclase are elongate (Figure 4-9). Quartz grains to 4mm may be polygonal, elongate or irregular in shape, with some displaying undulose extinction and evidence of grain boundary migration.

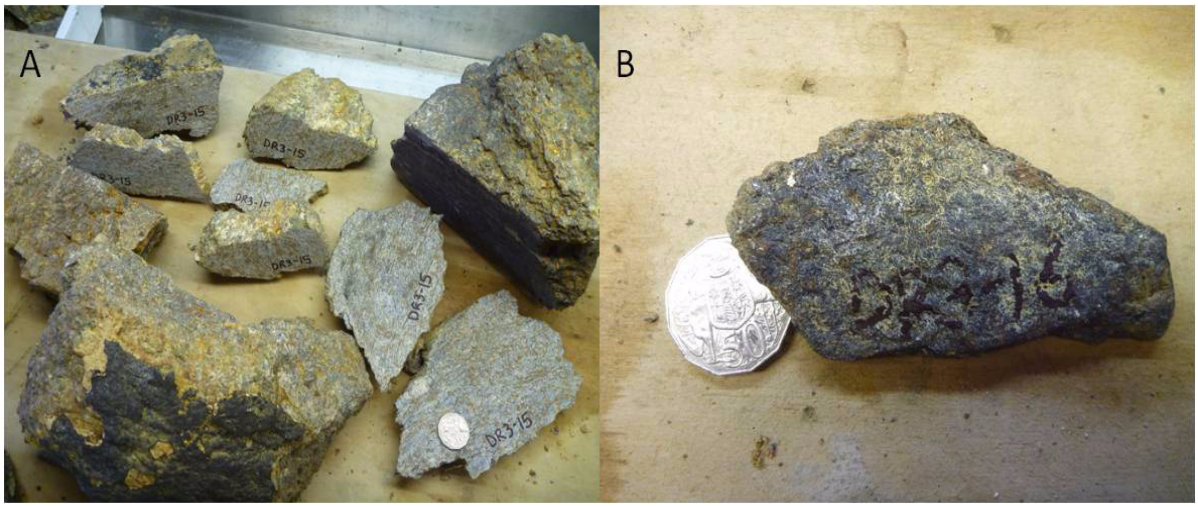

Figure 4-6: Hand samples of DR3-15 (A) and DR3-16 (B) coin is 31mm (Halpin, 2011)

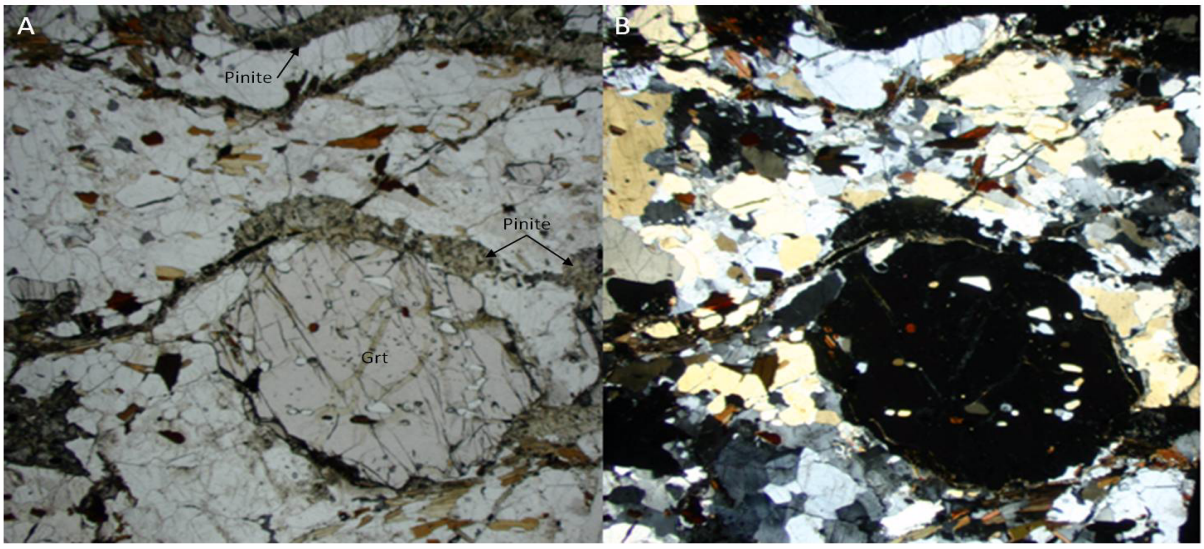

Figure 4-7: Sample DR3-15 thin section showing garnet poikiloblast and pinite A: PPL, B:XPL; FOV 5mm

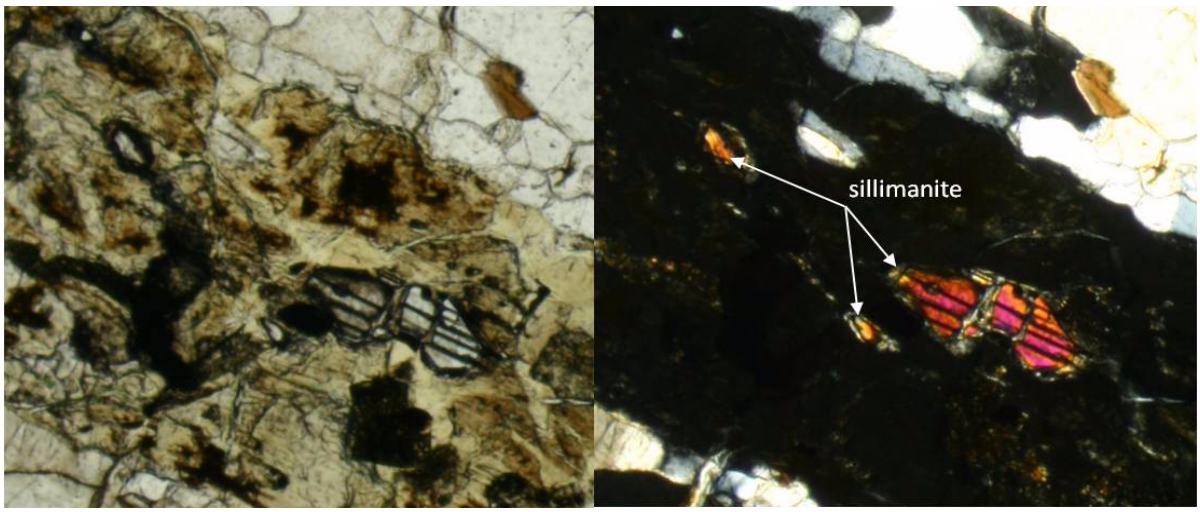

Figure 4-8: Sample DR3-15 thin section showing sillimanite in pinite A: PPL, B:XPL; FOV 0.8mm

Plagioclase occurs as discrete crystals with distinct twining to 4mm, as flames and perthite textures with K-feldspar and as interstitial plagioclase being altered to sericite. Polygonal to anhedral K-feldspar crystals to 4mm are in close association with plagioclase and quartz. Biotite is being altered where it is near the pinite strings (Figure 4-10).

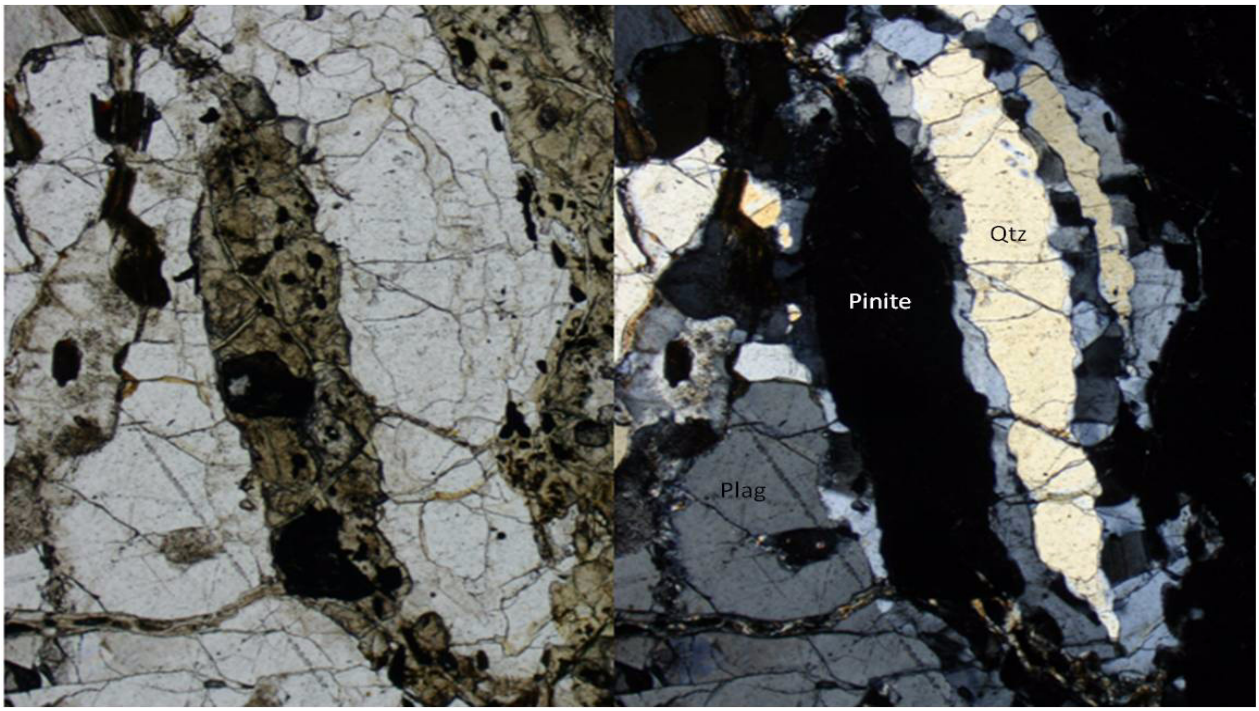

Figure 4-9: Sample DR3-15 thin section showing pinite with elongate quartz and plagioclase A: PPL, B:XPL; FOV 2.5mm

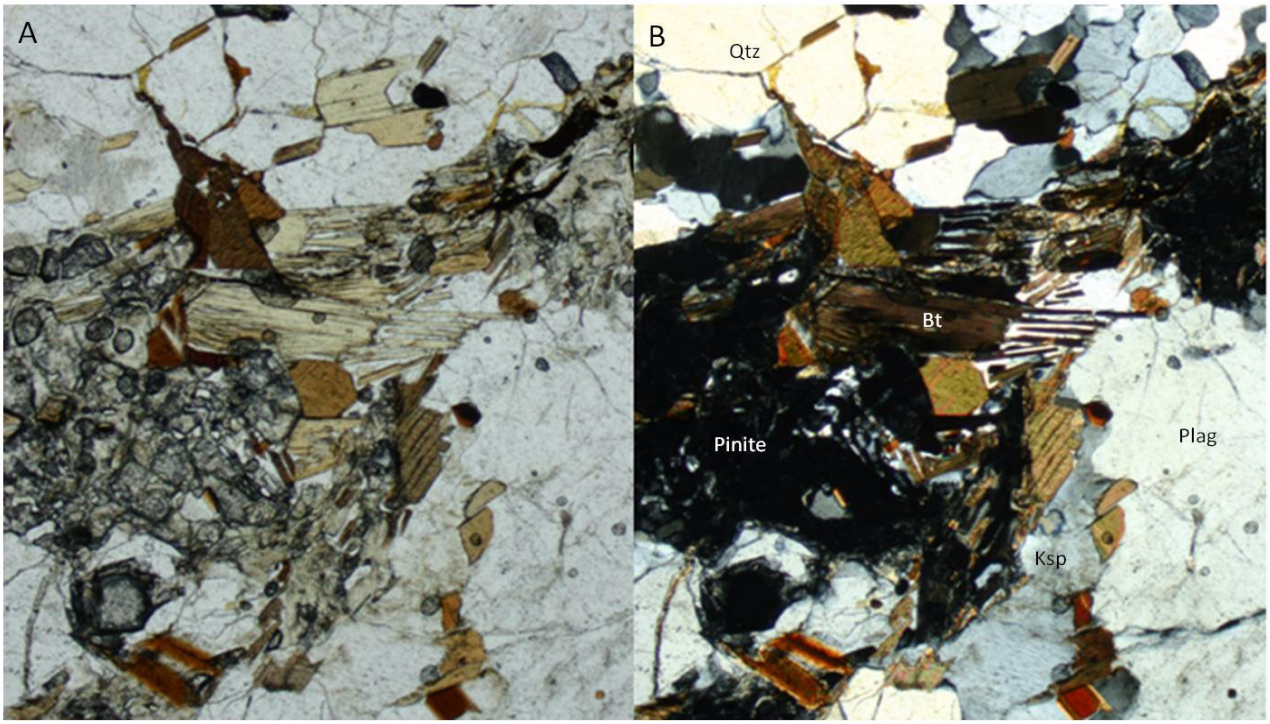

Figure 4-10: Sample DR3-15 thin section showing biotite and pinite A: PPL, B:XPL; FOV 2mm

4.2.5 DR3-16: Two pyroxene-pargasite orthogneiss

DR3-16 is a small mafic sample approximately 11cm x 5cm x 1.5cm (Figure 4-6B) with a foliation defined by the orthopyroxene and amphibole minerals. The mode is 30% plagioclase, 30% orthopyroxene, 25% amphibole, 10% clinopyroxene and 5% biotite with minor opaques. Orthopyroxene forms strips up to 3mm long of subhedral crystal aggregates which appear heavily fractured (Figure 4-11). By contrast the clinopyroxene appears as larger discrete subhedral crystals to 1.5mm.

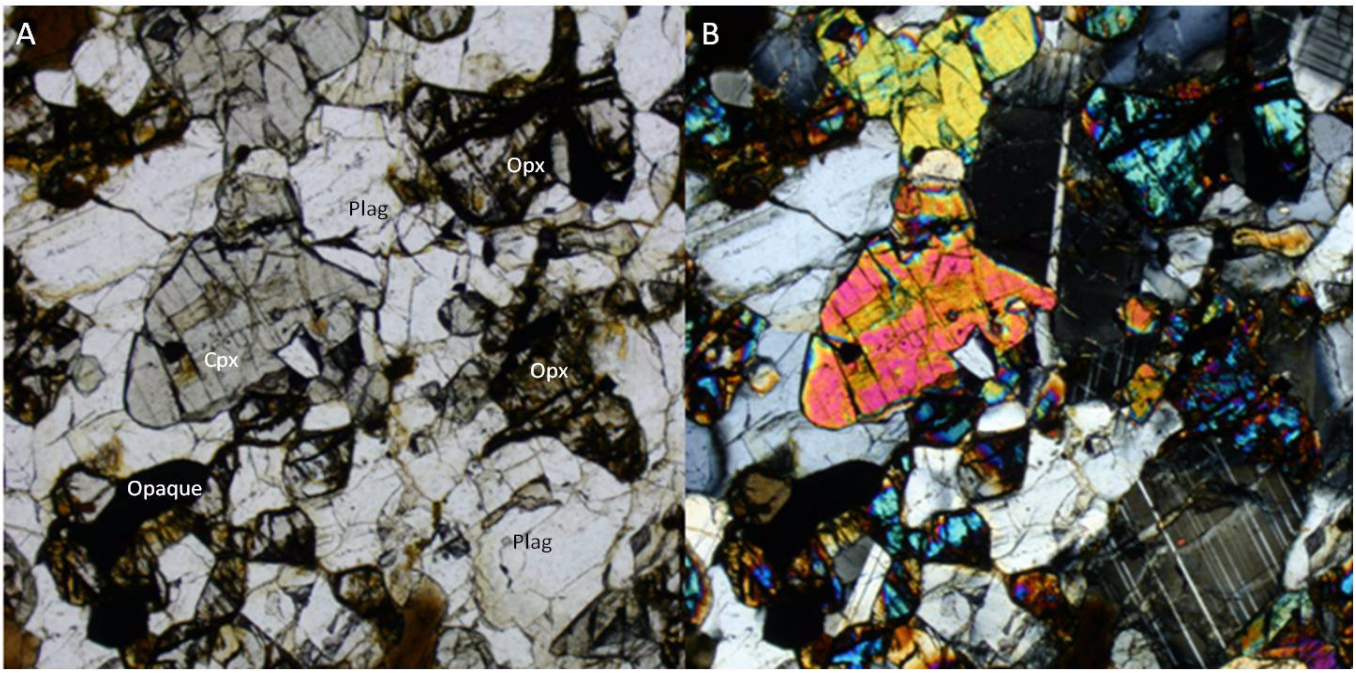

Figure 4-11: Sample DR3-16 thin section showing orthopyroxene and clinopyroxene A: PPL, B:XPL; FOV 1.5mm

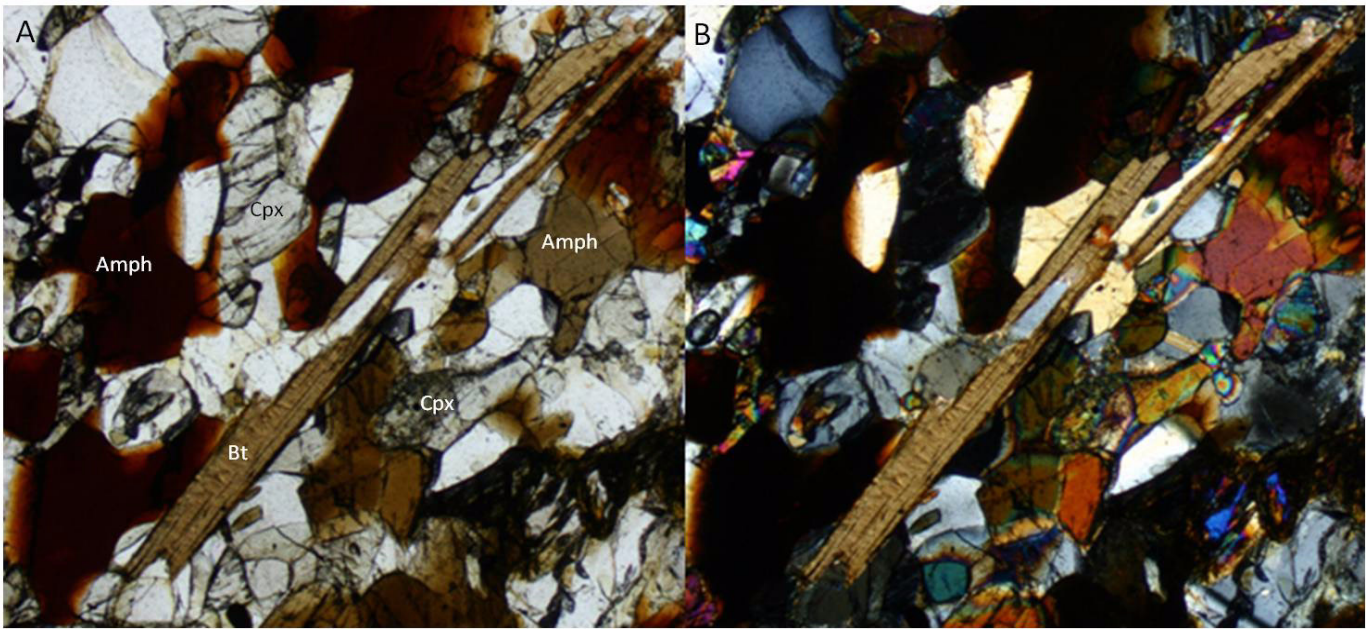

Figure 4-12: Sample DR3-16 thin section showing amphibole and biotite A: PPL, B:XPL; FOV 2mm

Brown amphibole has irregular shapes and blurred edges forming subhedral crystals to 2mm (Figure 4-12) in close proximity to plagioclase which forms 0.5mm crystals with distinct twinning and some alteration to sericite. Plagioclase is polygonal to 1mm, displays twinning and forms inclusions in some pyroxenes and amphibole. Biotite forms euhedral crystals to 3mm which display rounded terminations indicating it is being consumed.

4.3 DISCUSSION

Metamorphic textures and foliation are evident in all samples. The presence of foliation suggests both deformation and metamorphism have a tectonic origin. In samples DR3-1, DR3-2, DR3-6 and DR3-16 the foliation is subtle, defined by the aggregation of crystals into elongated strings. By contrast, DR3-15 is strongly foliated. The garnets display a band of inclusions towards the edge of the crystal (Figure 4-7). The random orientation of the inclusions and the strong deflection of the pinite around the garnets suggests the garnets were formed prior to the deformation event (Passchier & Trouw, 1996). In addition, DR3-15 appears to have undergone a high strain event as Figure 4-7 shows the garnet is a σ-type mantled porphyroblast displaying weak asymmetry (Passchier & Trouw, 1996). The quartz to the left and right of the garnet in Figure 4-7 appears to have formed in a pressure shadow.

The mineral assemblage of DR3-15 (garnet, quartz, plagioclase biotite and sillimanite) suggests this sample is a sedimentary mud rock metamorphosed in the granulite facies (Blatt & Tracy, 1996) The residual sillimanite suggests it was extensive throughout the sample, but has now been altered to form the pinite seen in the sample.

Sample DR3-16 has brown amphibole which is typical of high temperature metamorphism (Raase, 1974), orthopyroxene, clinopyroxene and plagioclase. This combination of minerals suggests that this sample had a mafic igneous protolith metamorphosed in the granulite facies (Blatt & Tracy, 1996).

DR3-2 and DR3-6 both show evidence of plagioclase being altered to sericite though this is more pronounced in DR3-2 (Figure 4-3) where the alteration is obvious in the hand sample. The mineral assemblage of DR3-2 suggests a granite protolith, while the absence of biotite in DR3-1 and DR3-6 suggests these two could have either a sedimentary or igneous protolith. The the size and rounded shapes of DR3-1 and DR3-6 suggest they formed in-situ on a cobble beach which are common in areas of tectonic uplift (Daczko, 2012).

CHAPTER 5: MINERAL CHEMISTRY

This chapter expands on Chapter 4 classifying the individual minerals, investigating mineral associations not seen using the petrographic microscope and further comparing the samples to determine where similarities and differences occur. The implications of these aspects for the original protolith and metamorphic history of each sample is considered, particularly where this was ambiguous after the petrography examination.

5.1 METHOD

Interesting structures and minerals within the thin sections were examined using the Cameca SX100 electron microprobe (EMP) at the GAU within the GEMOC facility at Macquarie University. The EMP has five crystal spectrometers and an energy dispersive system used to measure the Kα X-ray signals of K, Ca, Na, Fe, Mn, Al, Si, P, Cr, Mg, Ti, Ni and Cl (set up per Table 5-1). Electrons were accelerated from a tungsten filament at 15 KeV, providing a beam current of 20 nAmps onto a spot size as small as possible: less than 1 μm. A count time of 10 seconds for the peak with 5 seconds either side of the peak was used. The EMP was calibrated using the following standards: Na on albite, Ca on $CaSi0_3$, K on orthoclase, Fe on iron, Mn on spessartine garnet, Al on kyanite, P on apatite, Cr on chromium, Cl on chlorapatite and Si and Mg on olivine. Oxygen was inferred using stoichiometry.

Detector	Elements analysed
1: LTAP	Na Kα, Al Kα, P Kα, Mg Kα
2: TAP	Si Kα
3: LPET	K Kα, Ca Kα, Ti Kα, Cl Kα
4: TAP	-
5: LLIF	Fe Kα, Mn Kα, Cr Kα, Ni Kα

Table 5-1: EMP mineral analysis: wavelengths and crystals

The theoretical lower level of detection (LLD) calculated using the peak and background counts and %rsd (percentage relative standard deviation) was provided by the Macquarie University laboratory (Table 5-2). Photomicrographs and backscattered electron (BSE) images were taken of the analysed parts of the thin sections.

Element	LLD (wt%)	% rsd
SiO_2	0.03	0.27
TiO_2	0.02	0.19
Al_2O_3	0.01	0.18
Cr_2O_3	0.04	0.56
FeO	0.03	0.34
MnO	0.03	0.55
MgO	0.03	0.22
CaO	0.02	0.27
Na_2O	0.02	0.56
K_2O	0.01	0.49
NiO	0.03	0.30
P_2O_5	0.01	0.65
Cl	0.01	0.82

Table 5-2: LLD for each element oxide

Analyses with anomalous totals were discarded. Biotite samples with less than Ca + Na + K = 1.8 (cations based on 22 Oxygen) were rejected as the breakdown to chlorite is underway. The mineral at each analysed spot was determined by calculating cation data and using stoichiometry.

Element maps were taken of the garnet in DR3-15 and a sample of matrix in DR3-2. The same Cameca SX100 EMP equipment was used, however, the laser and detector set up was as described in Table 5-3. This provided 5 element maps for each analysis run, allowing the subtle variation of elements within and across the minerals to be seen.

Element Map	DR3-15 Garnet	DR3-2 Feldspar
# Steps	512 x 512	512 x 512
Step size	13 µm	5 µm
Map size	6.5 mm^2	2.5 mm^2
Beam current	100nA	20nA
Beam size	focused	focused
Dwell time	20nsec	5nsec
detector 1: LTAP	K Kα	K Kα
detector 2: TAP	Si Kα	Al Kα
detector 3: LPET	Ca Kα	Ca Kα
detector 4: TAP	Mg Kα	Na Kα
detector 5: LLIF	Fe Kα	Fe Kα

Table 5-3: EMP element maps: wavelength and crystals

5.2 RESULTS

For comparison purposes all the samples have been included in a plagioclase ternary diagram (Figure 5-1) and two graphs of the opaque minerals. The first showing the solid solution between haematite (Fe_2O_3), ilmenite ($FeTiO_3$) and rutile (TiO_2) minerals (Figure 5-2) and the second showing their relationship with Mn (Figure 5-3). The biotites of samples DR3-2, DR3-15 and DR3-16 have been included in graphs showing the relationship between iron (Fe) and magnesium (Mg) (Figure 5-4) and titanium (Ti) vs XFe (Figure 5-5).

$$XFe = \frac{Fe}{Fe + Mg}$$ (Fe and Mg cation numbers based on 22 oxygen)

The results of the individual samples is documented with reference to these and other specific graphs and figures. The results are interpreted in the discussion section.

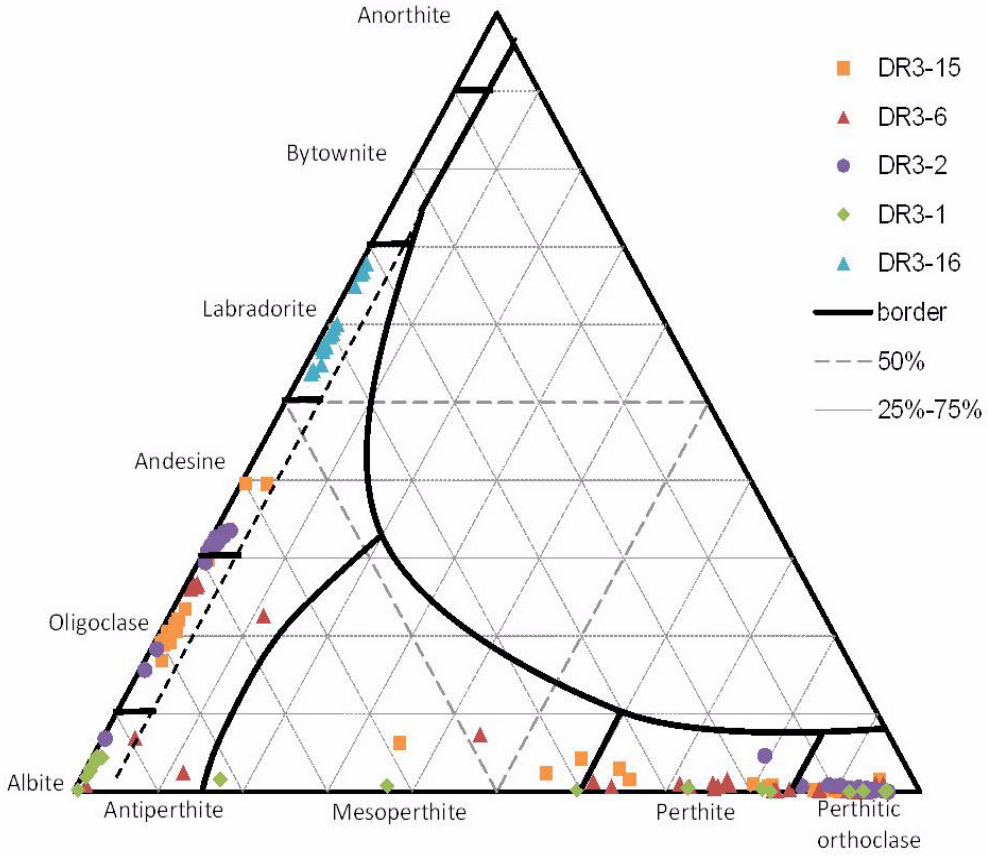

Figure 5-1: DR3 feldspar ternary diagram

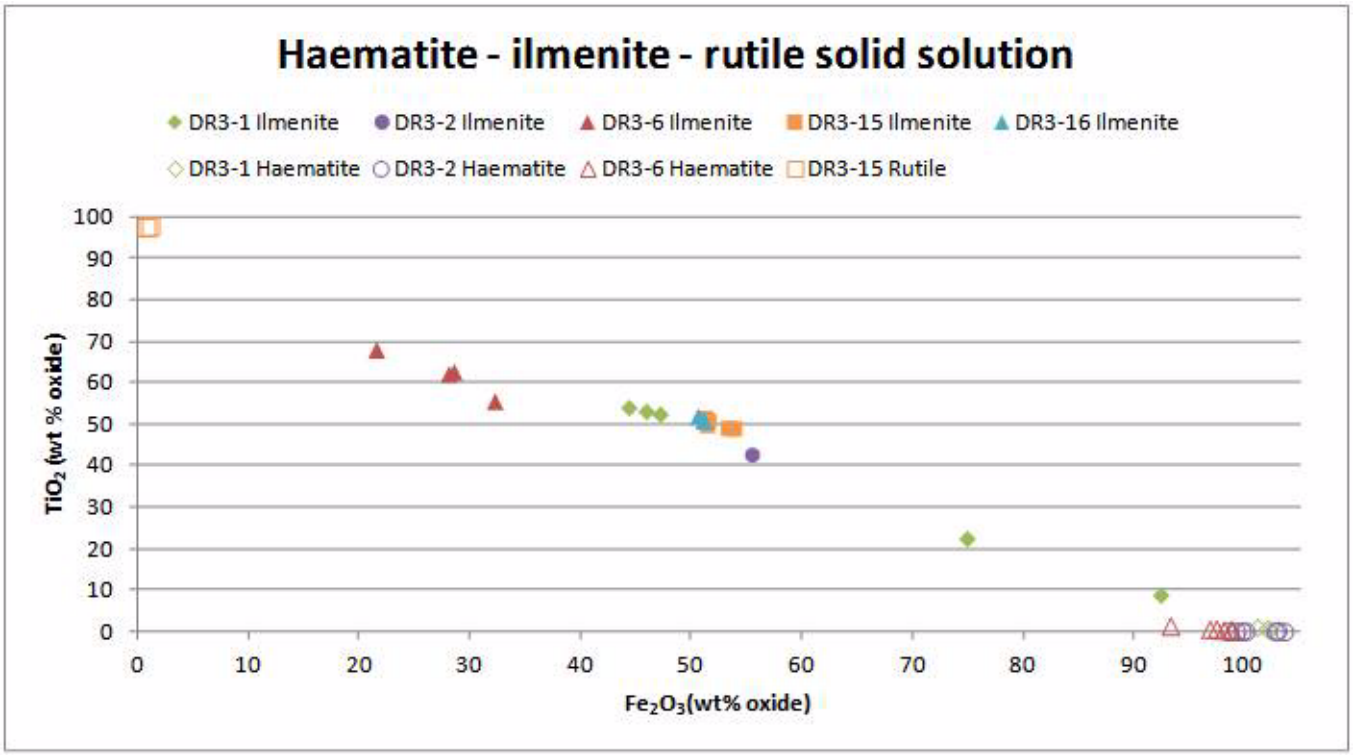

Figure 5-2: DR3 graph showing haematite-ilmenite-rutile solid solution

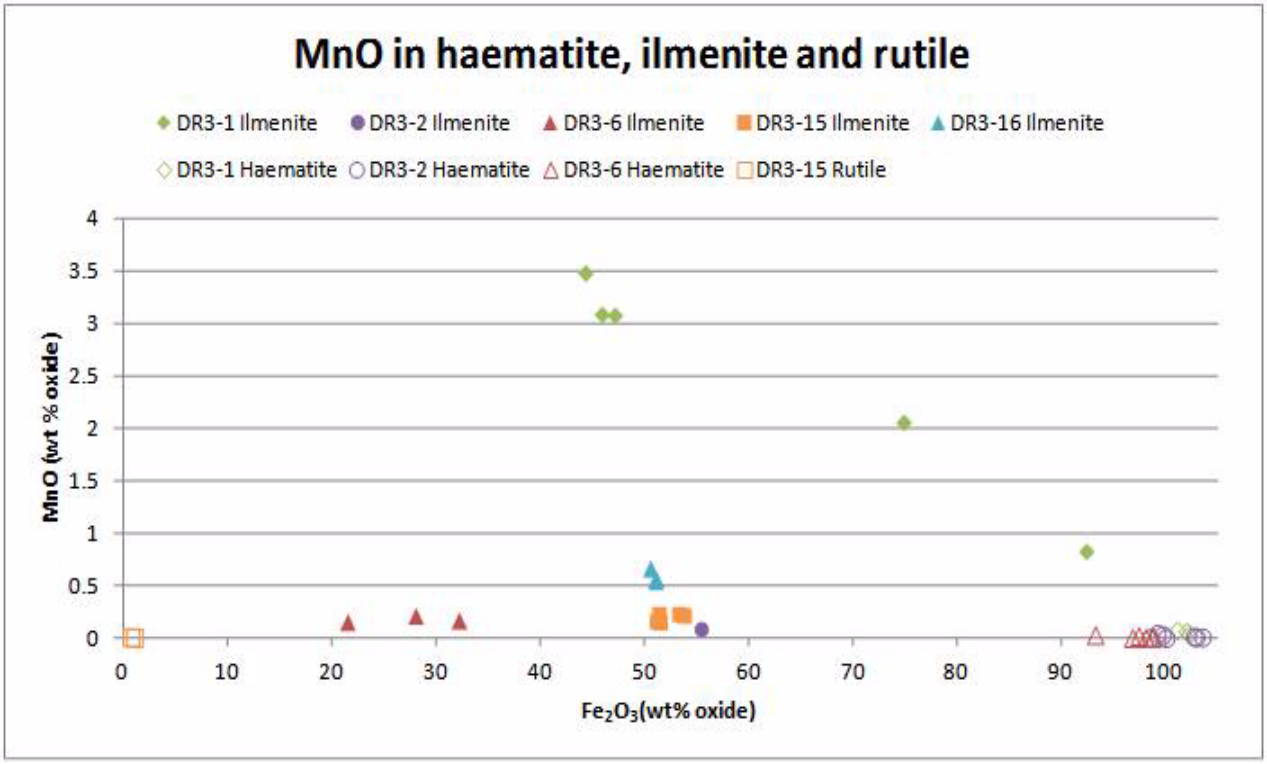

Figure 5-3: DR3 graph of opaque minerals: Fe_2O_3 vs. MnO

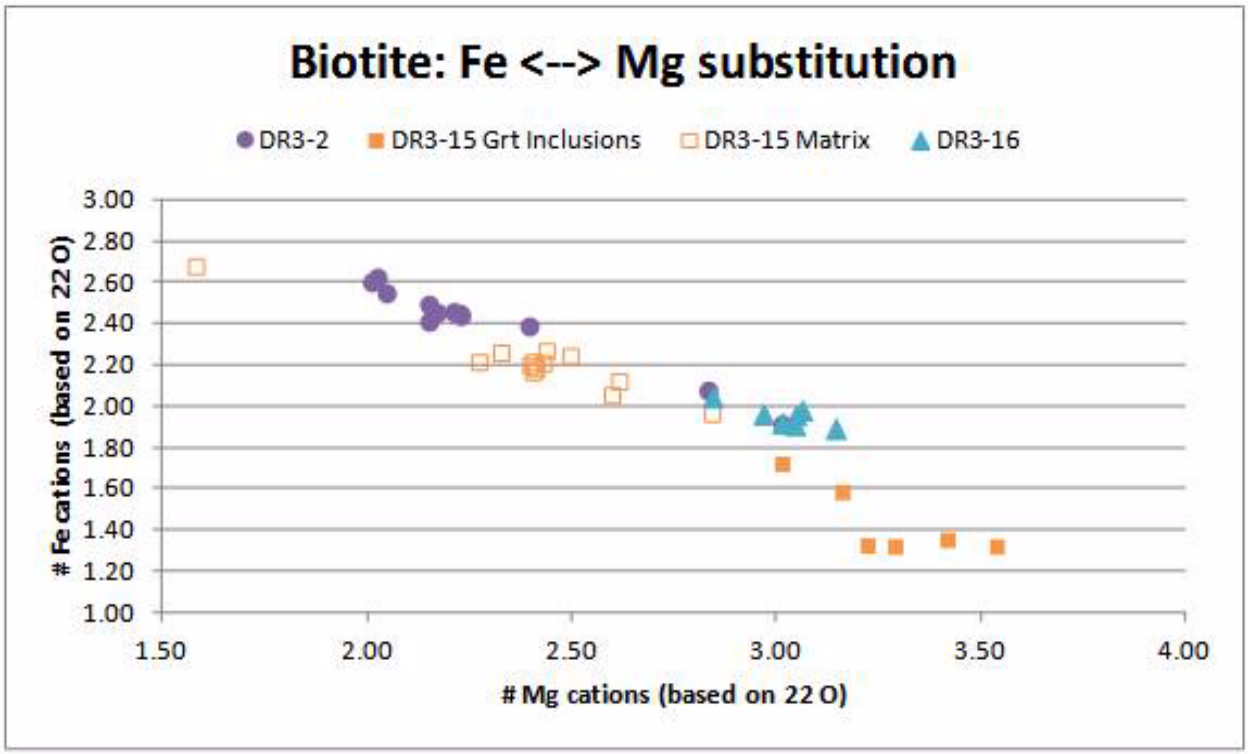

Figure 5-4: DR3 graph of biotites: Mg vs. Fe cations

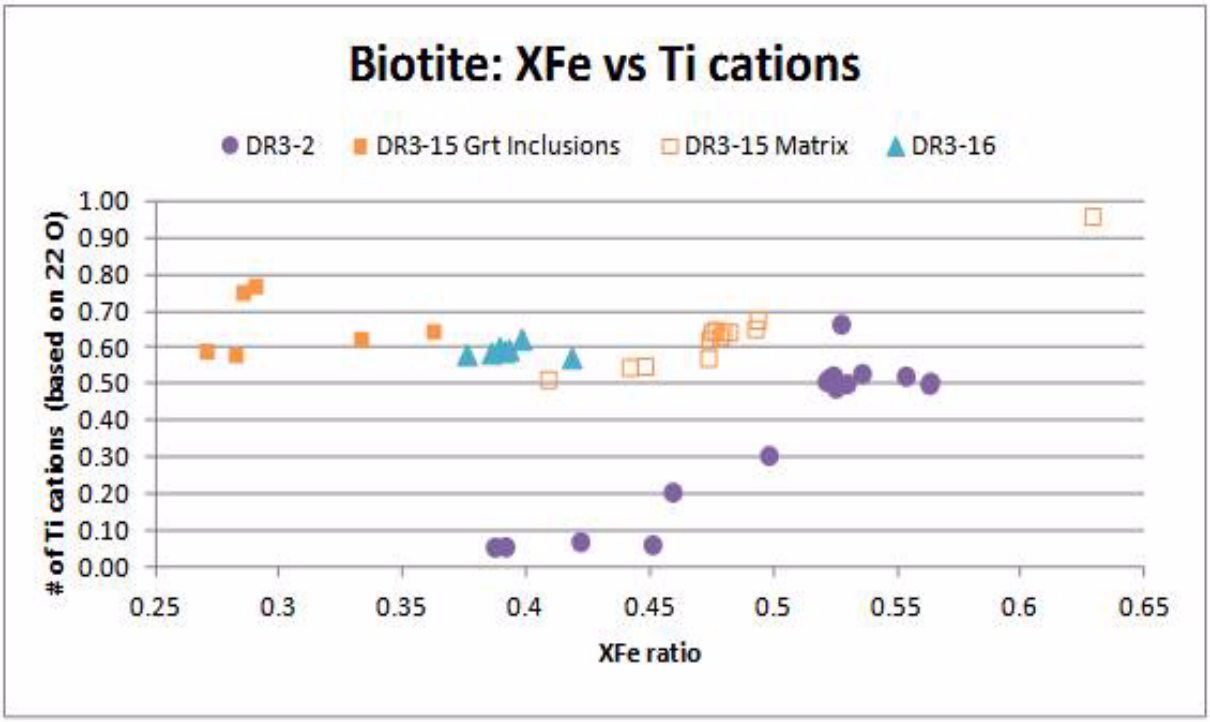

Figure 5-5: DR3 graph of biotites: XFe vs. Ti cations

5.2.1 DR3-1: Two feldspar-quartz orthogneiss

Figure 5-1 shows the plagioclase in sample DR3-1 is albite, the sodium (Na) end member with very little anorthite, the calcium (Ca) end member influence. Figure 5-1 also shows a spread of spot analyses across the base of the ternary diagram from albite to orthoclase, the potassium (K) end member. It is likely that the spot samples that fall within the mesoperthite and perthite regions of the graph are areas of mixed albite and K-feldspar as the flames of albite are very fine (Figure 5-6) within the K-feldspar crystals. The backscatter image in Figure 5-6 shows albite rims around the K-feldspar and the extensive fine perthite flame structures. These textures occur in both the large and small crystal domains, and no zoning of the crystals was found.

The opaques have formed from an exsolution of ilmenite ($FeTiO_3$) and haematite (Fe_2O_3). Figure 5-6 shows the lamellae that have formed. Mn is preferentially included in the ilmenite (Figure 5-3) with concentrations up to 3.470 wt% MnO. Haematite has concentrations of MnO to only 0.075 wt% oxide. The samples in Figure 5-2 showing compositions intermediate between ilmenite and haematite are most likely due to the analysis spot being across an ilmenite/haematite boundary within the opaque.

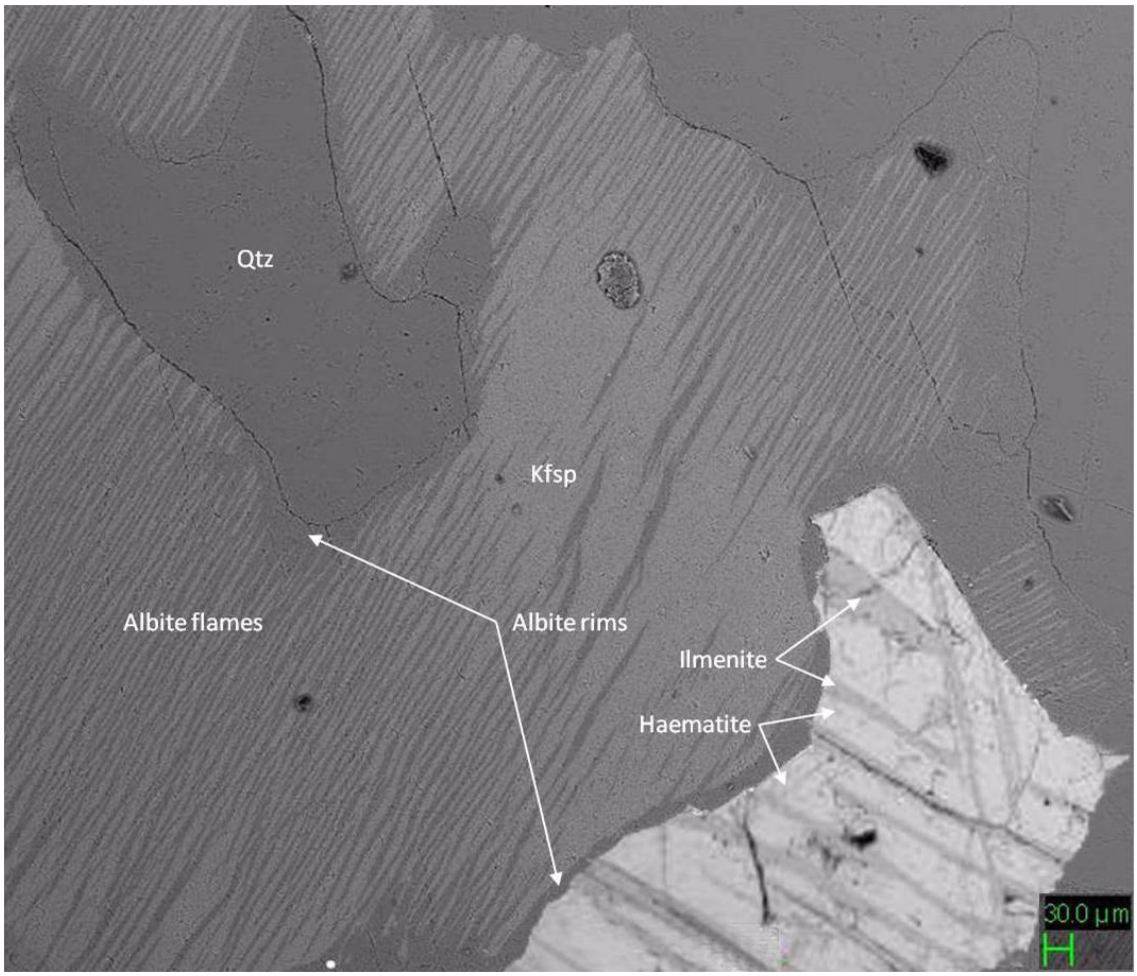

Figure 5-6: DR3-1 backscatter image of mineral textures (abbreviations per Table Appx-3)

5.2.2 DR3-2: Quartz-feldspar-biotite orthogneiss

Figure 5-1 shows the plagioclase seen in sample DR3-2 is predominantly oligoclase to andesine in composition. There is no obvious zoning across the plagioclase or K-feldspars, though Figure 5-7 shows an example of the subtle variation in the Na, K and Ca concentrations occurring across the feldspars and a small myrmekite intergrowth of plagioclase (oligoclase/andesine) and quartz. The K-feldspar crystals (light grey scale in the K element map Figure 5-7 C(i)) are relatively clean in PPL. The plagioclase displays a subtle increase in K and decrease in Ca element concentrations (Figure 5-7 C(i) and C(ii)) corresponding with increased alteration to sericite, that is, darker colours in the PPL and XPL images. The spot analyses in these areas are those in the albite to oligoclase regions in Figure 5-1. The Na element map (Figure 5-7 C(iii)) highlights minor Na rich albite flames in the K-feldspar crystal, but otherwise shows very little variation in concentration.

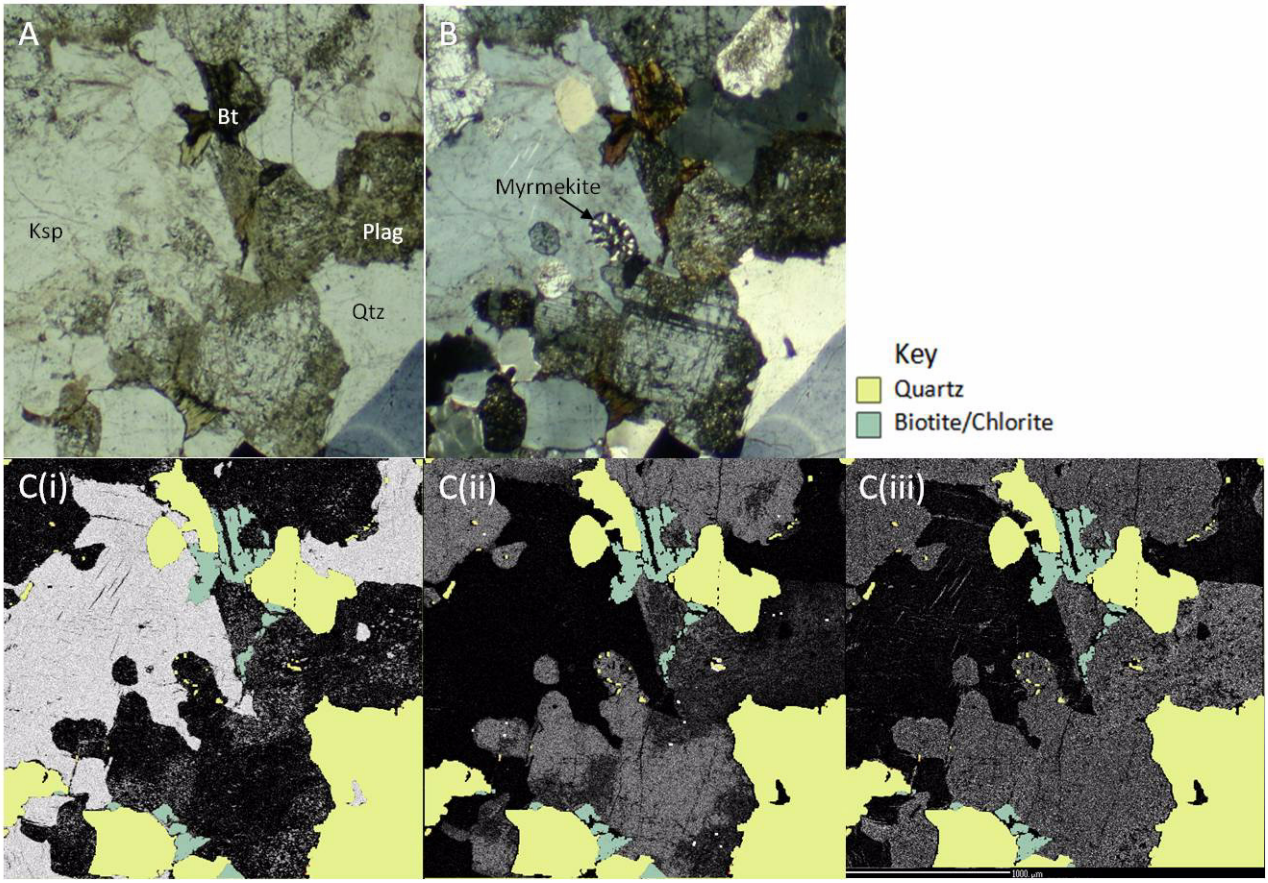

Figure 5-7: DR3-2 feldspar element maps A: PPL photo B: XPL photo (bottom right is marker pen) C(i): K element map C(ii): Ca element map C(iii) Na element map. Contrast has been modified to highlight subtle element variations

The biotite in sample DR3-2 is being altered to chlorite. Three samples of biotite were rejected as their Ca+Na+K total was less than 1.8 cations based on 22 O and two samples classified as chlorite were analysed. Domainal variation is seen within the biotites (Figures 5-8 and 5-9), however, this is not consistent core to rim, nor obviously associated with the replacement textures (Figure 5-10). A variety of other biotite spot analyses are plotted as orange circles on Figures 5-9 and 5-10. Figure 5-5 shows the Ti concentration is quite variable, but is correlated with the Fe concentration: Ti decreases as XFe decreases.

The haematite phase in DR3-2 does not have the strong lamellae structure of ilmenite seen in DR3-1. Ilmenite is however, present in smaller blebs within the larger haematite areas. Mn is only slightly concentrated into the ilmenite phase (Figure 5-3). Monazite and glomeroporphyritic zircons can also be seen in the backscatter images.

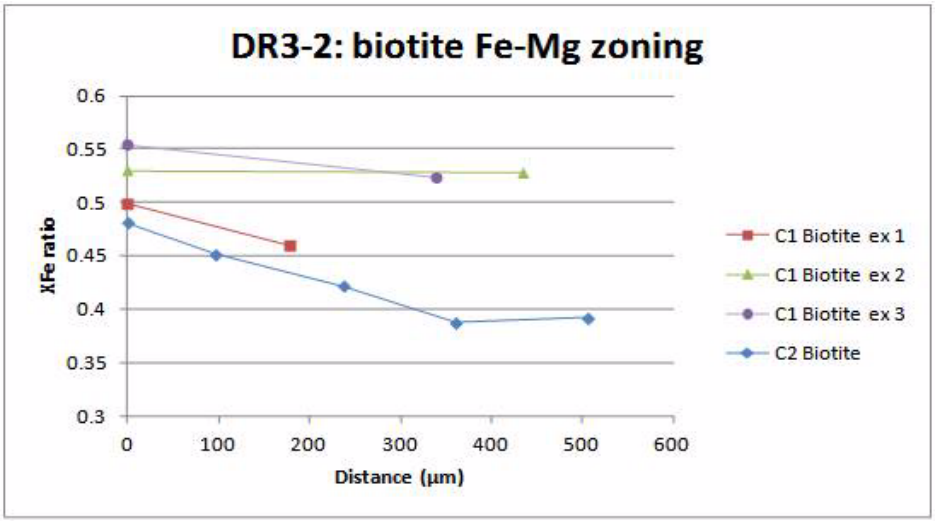

Figure 5-8: DR3-2 examples of XFe zoning in biotites (C1: Circle 1)

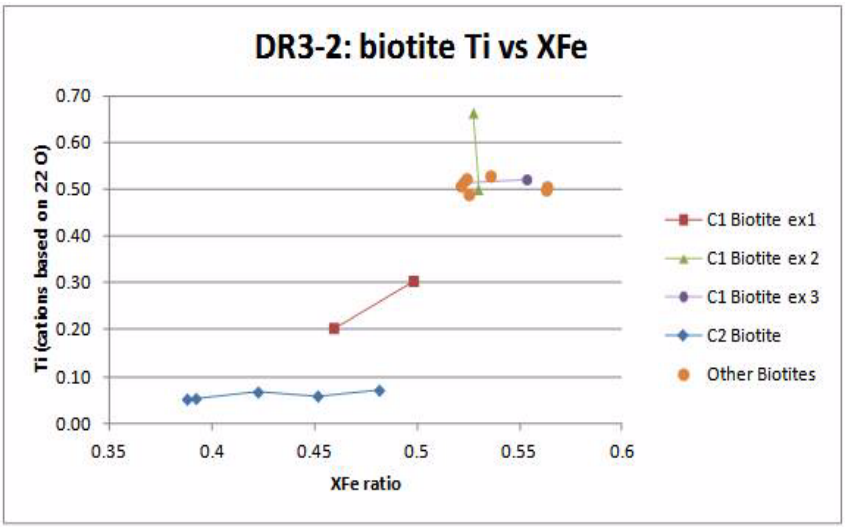

Figure 5-9: DR3-2 XFe ratio vs. Ti cations

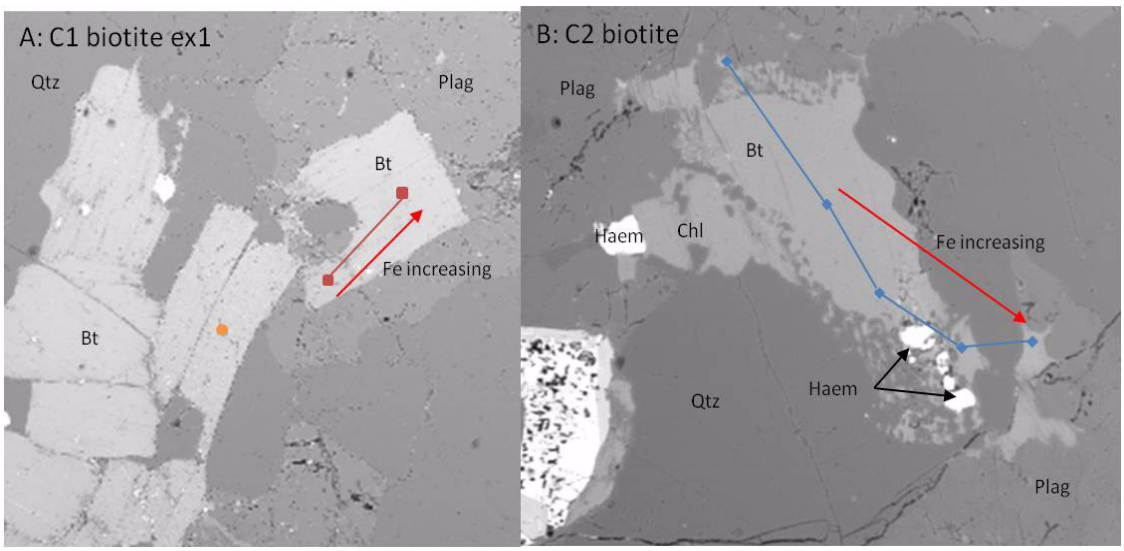

Figure 5-10: DR3-2 biotite examples. Backscatter images, key as for Figure 5-9

5.2.3 DR3-6: Two feldspar-quartz orthogneiss

Figure 5-1 indicates DR3-6 has orthoclase, albite and oligoclase feldspars. The samples spread across the base of the diagram in the perthite and mesoperthite regions are most likely analyses where the spot overlapped a flame of albite in the K-feldspar crystal as there are complex exsolution and diffusion textures in the K-feldspar (Figure 5-11). K-feldspar crystals have albite rims and include blebs of quartz. These features are similar to DR3-1, however, DR3-6 also includes discrete plagioclase crystals which are classified as oligoclase in Figure 5-1. The oligoclase crystals show no zoning though where they abut the K-feldspar crystals there does appear to be some diffusion of K^+ ions into the plagioclase, though this may also be due to an analysis spot with mixed minerals.

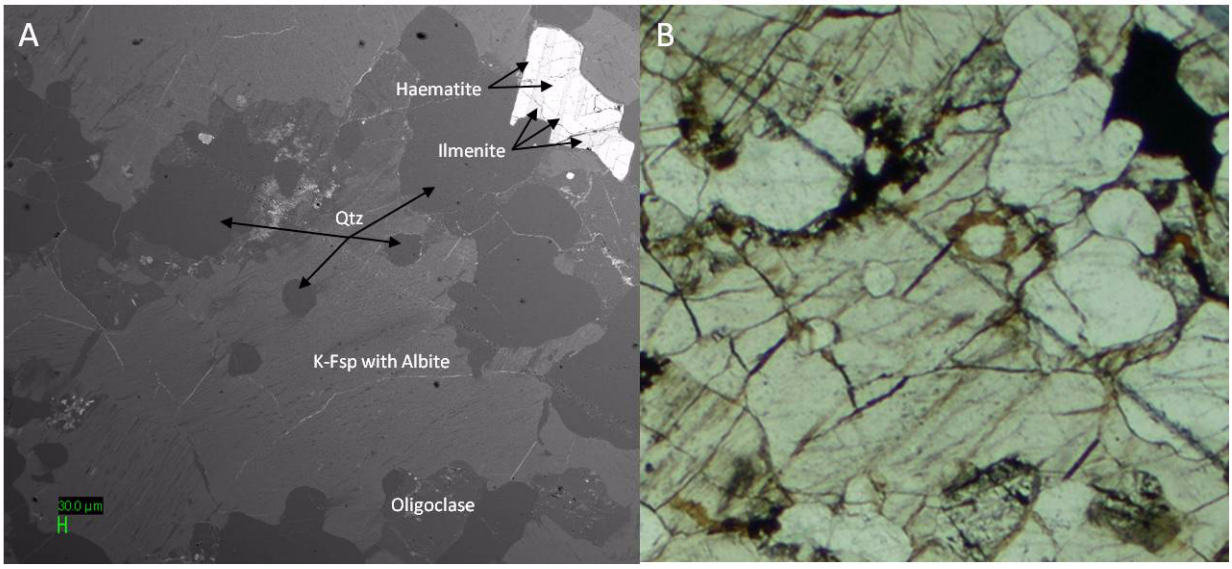

Figure 5-11: DR3-6 mineral textures A: backscatter image B: PPL

Similarly to DR3-1 the opaques are haematite with exsolved lamellae of ilmenite though the concentration of TiO_2 is high at 63 to 68 wt% oxide. All ilmenite sample spots were taken from lamellae associated with haematite. This may indicate an analysis site of mixed ilmenite and haematite origin, or a higher concentration of TiO_2 in the opaque oxide prior to the exsolution process occurring. There is a minor increase in Mn in the ilmenite (Figure 5-3).

5.2.4 DR3-15: Garnet-sillimanite-biotite paragneiss

The bulk of the plagioclase in sample DR3-15 is in the matrix and is classified as oligoclase in the feldspar ternary (Figure 5-1). The andesine spots are all taken from plagioclase inclusions within the garnets. Similarly to the earlier samples, the K-feldspar falling in the perthite and mesoperthite area of Figure 5-1 are most likely analysis spots over a plagioclase flame within a K-feldspar crystal. In this sample the flames are not as prevalent and are much finer. Figure 5-12 shows a quartz and oligoclase core with a rim of oligoclase and small intergrowths of K-feldspar.

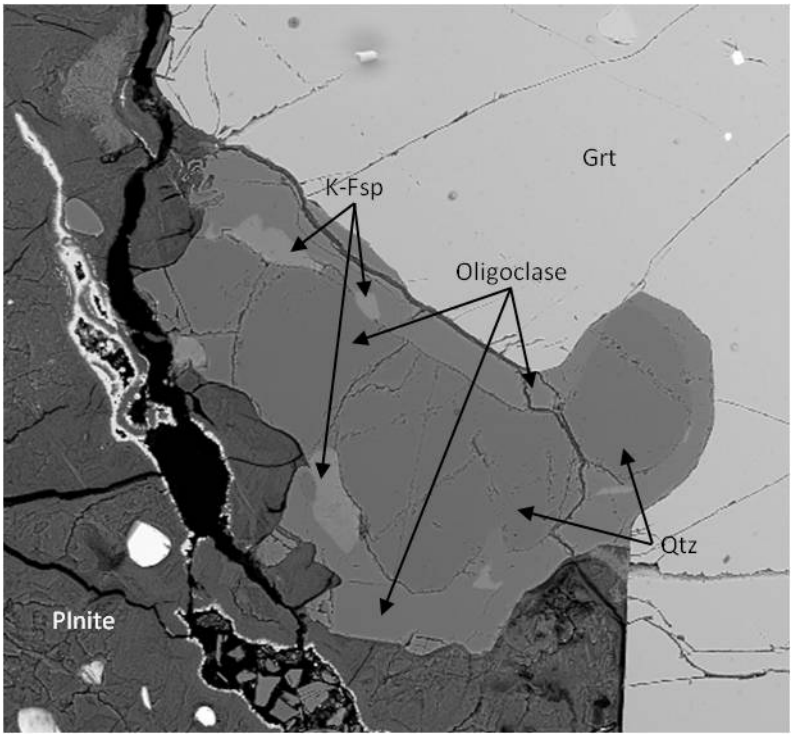

Figure 5-12: DR3-15 quartz, oligoclase, K-feldspar texture

The garnets in DR3-15 are classified as pyrope-rich almandine as they have $Alm_{60-72}Pyr_{22-33}Grs_{2-10}Sps_{1-2}$ (Figure 5-13). The center of the garnets has a slightly higher grossular (Ca) concentration. A traverse (Figure 5-14) shows subtle zoning with higher concentrations of Fe and lower Ca on the edges of the garnets (Figure 5-15 A(i) & (ii) and B). Mg also appears to be zoned similarly to Ca with higher concentrations on the edge of the garnet crystal (Figure 5-15A(iii)). Adding the matrix garnets to the zoning graphs (Figure 5-16) shows that there are two periods of garnet growth with substitution occurring as the Fe concentration increases. The first, seen in the samples from the centre of the garnets is richer in Ca and Mg and has Fe substituting for Ca, while the second, which includes the edge of the traverse and the other garnet edge samples is higher in Fe and Mn and shows Fe substituting for Mg.

The garnets in DR3-15 have many inclusions, with a band of larger inclusions towards the edge (Figure 5-14). The inclusions include andesine plagioclase, rutile in the centre with ilmenite towards the edge, biotite, quartz and monazite.

The biotites that occur as inclusions in the garnets are in the band towards the edge of the garnet, rather than the core of the garnet. Figure 5-4 shows that the inclusions are appreciably higher in Mg and lower in Fe than the biotites in the matrix. The analysis site associated with the anomalously high Fe concentration is near the pinite in the matrix.

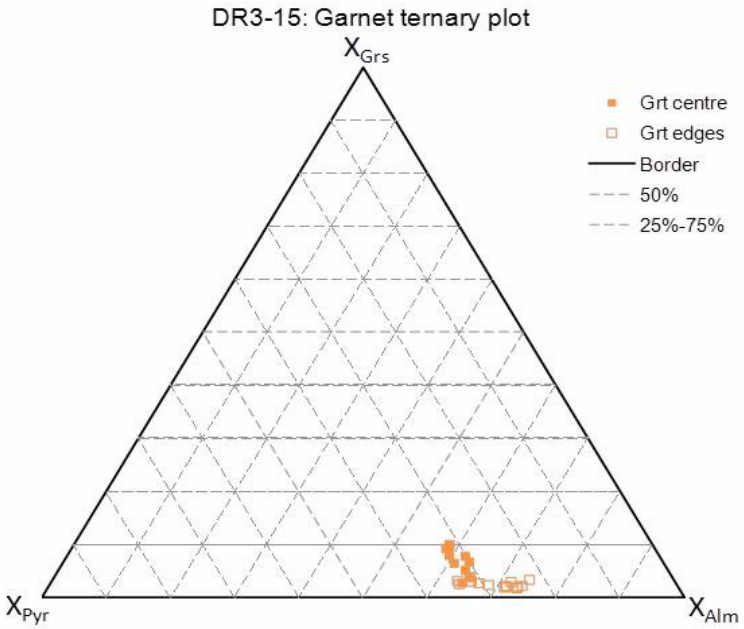

Figure 5-13: DR3-15 garnet ternary plot

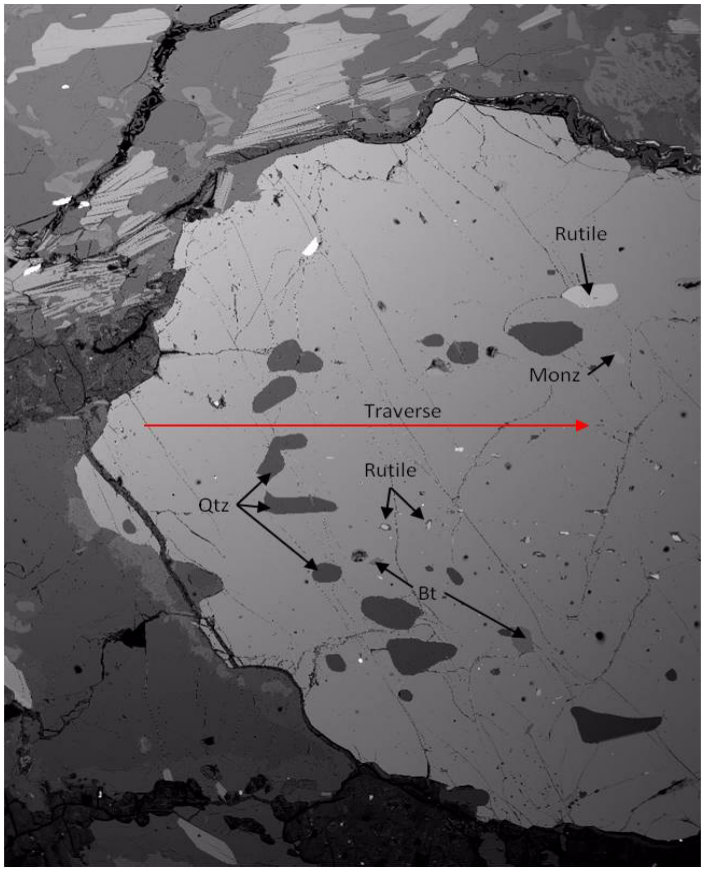

Figure 5-14: DR3-15 backscatter image of garnet inclusions

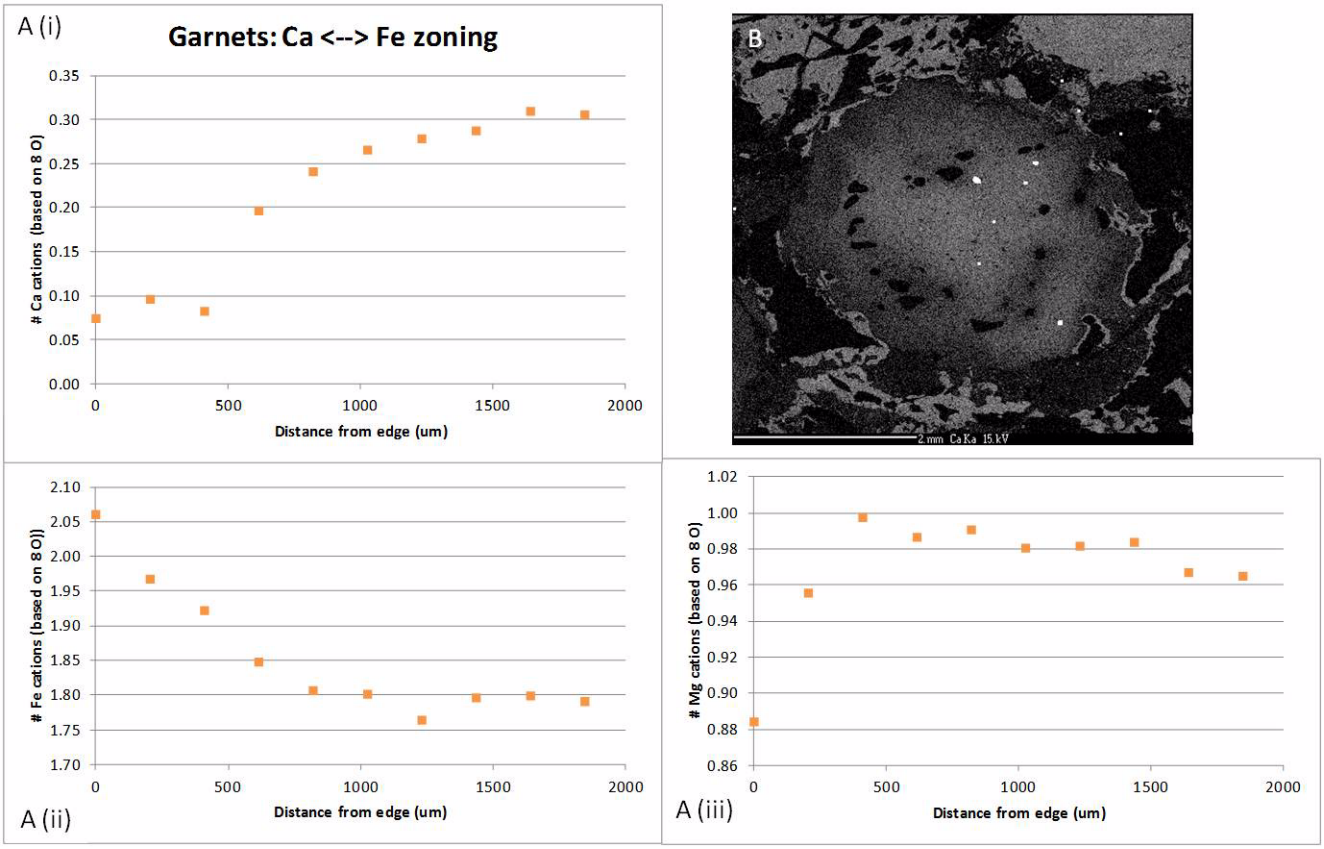

Figure 5-15: DR3-15 garnet zoning - Ca, Fe and Mg substitution A: Graphs of garnet traverse B: Ca element map showing zoning (contrast has been modified to highlight subtle element variations; bright spots are monazite)

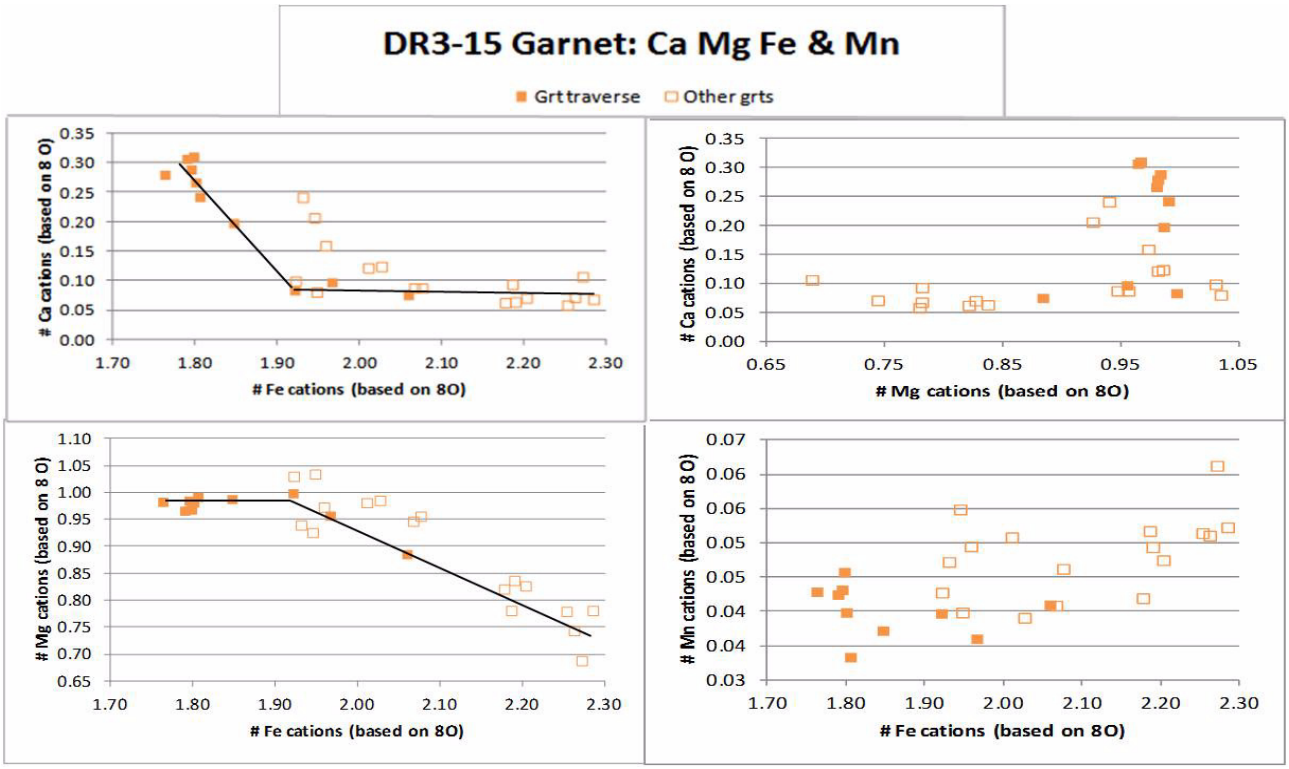

Figure 5-16: DR3-15 garnet growth relationship between Fe, Ca, Mg & Mn

5.2.5 DR3-16: Two pyroxene-pargasite orthogneiss

The plagioclase in sample DR3-16 is all classified as labradorite on the plagioclase ternary diagram in Figure 5-1. The samples with slightly higher Ca concentrations (sample sites are highlighted with a red star in Figures 5-17 and 5-18) are either surrounded by or adjacent to amphibole. There is one sample with increased Ca however, (Figure 5-17) which is surrounded by orthopyroxene.

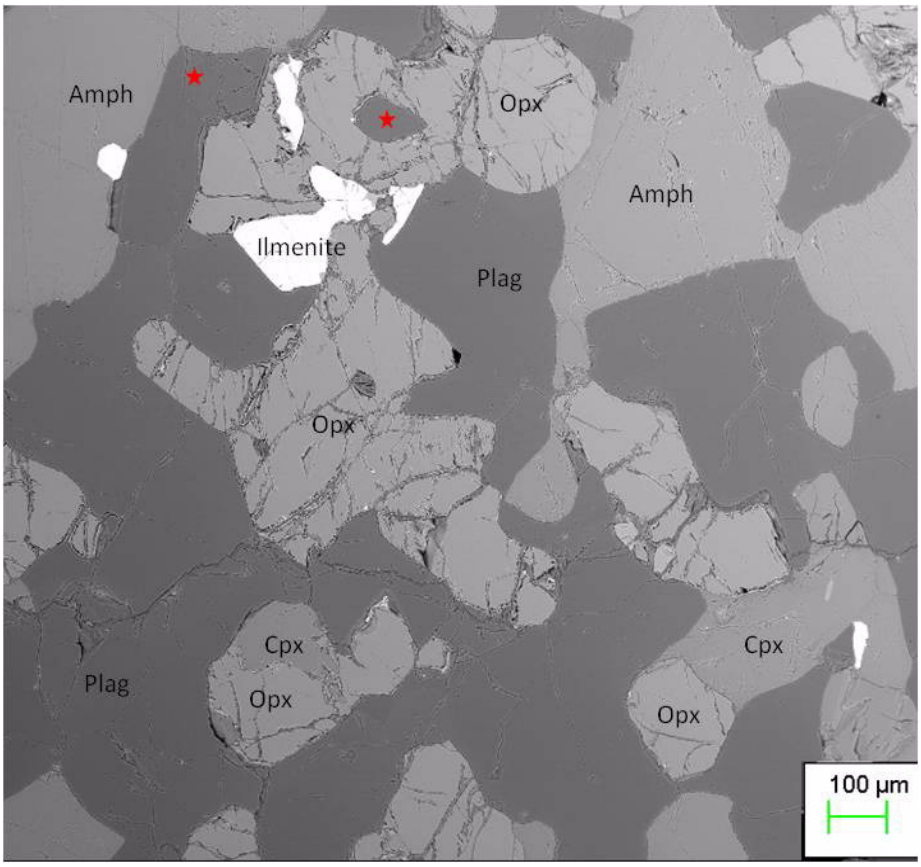

Figure 5-17: DR3-16 mineral textures: plagioclase, amphibole and pyroxenes. Red stars are higher Ca concentration labradorite plagioclase analysis sites

The amphiboles show some zoning across their length. A traverse (Figure 5-18) indicates that the end of the amphibole closest to the high Ca plagioclase is also marginally higher in Ca. Figure 5-19 shows that this end of the amphibole also has a marked increase in Al, Fe, Ti and Na and a decrease in Mg and Si (Si not shown). Graphing the elements against Si (Figure 5-20) shows that as Si increases there is a trend to decreased Al, Fe, Ca, Na, K and Ti which reflects the complex substitution pairs for calcic amphibole. Mg (not shown in Figure 5-20), however, does not show any particular variation. The amphibole is classified as pargasite (Leak et al., 1997).

The pyroxenes have been classified using Morimoto et al. (1988) (Figure 5-21). The clinopyroxenes are divided into augite and diopside. The augite sample sites are all adjacent to amphibole, whereas the diopside sites are all surrounded by or adjacent to plagioclase (Figure 5-17). The diopside has a slight increase in Ca and a decrease in Fe cations. The orthopyroxene is enstatite and shows very little variation in composition (Figure 5-21).

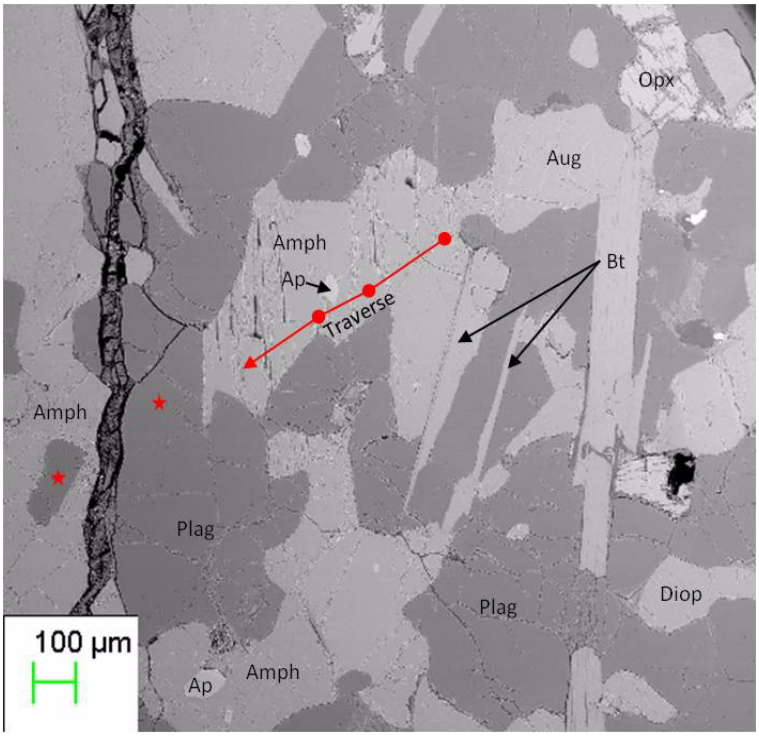

Figure 5-18: DR3-16 mineral textures: plagioclase, biotite and amphibole. Red stars are higher Ca plagioclase samples

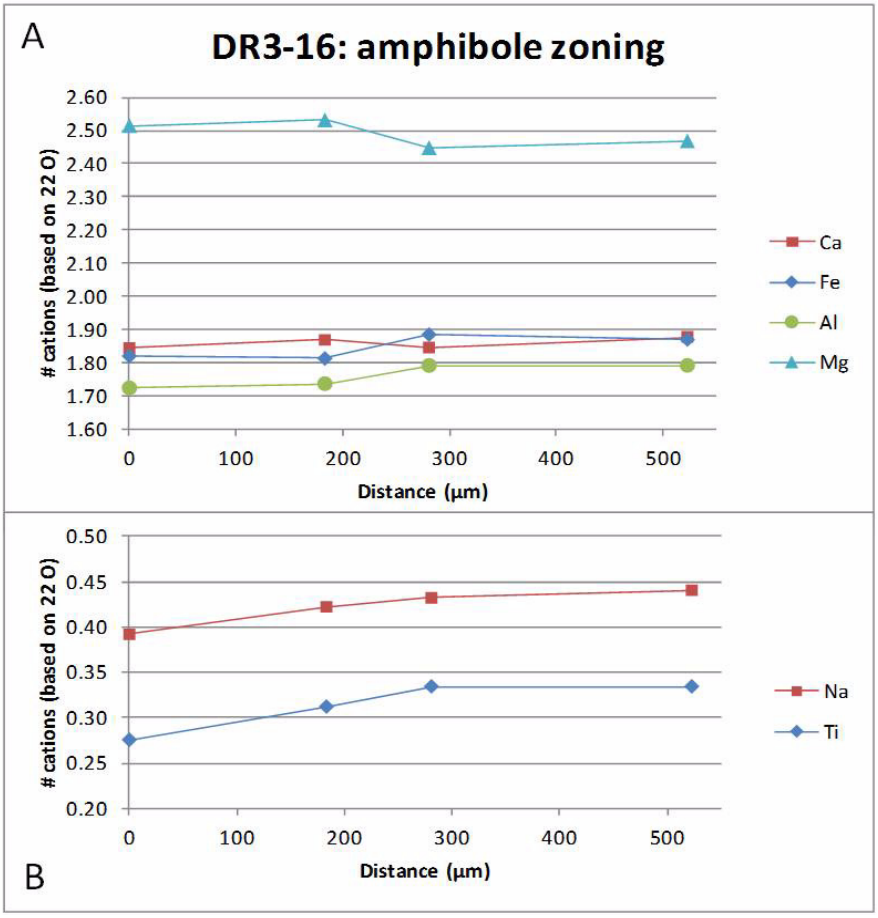

Figure 5-19: DR3-16 amphibole zoning element graphs

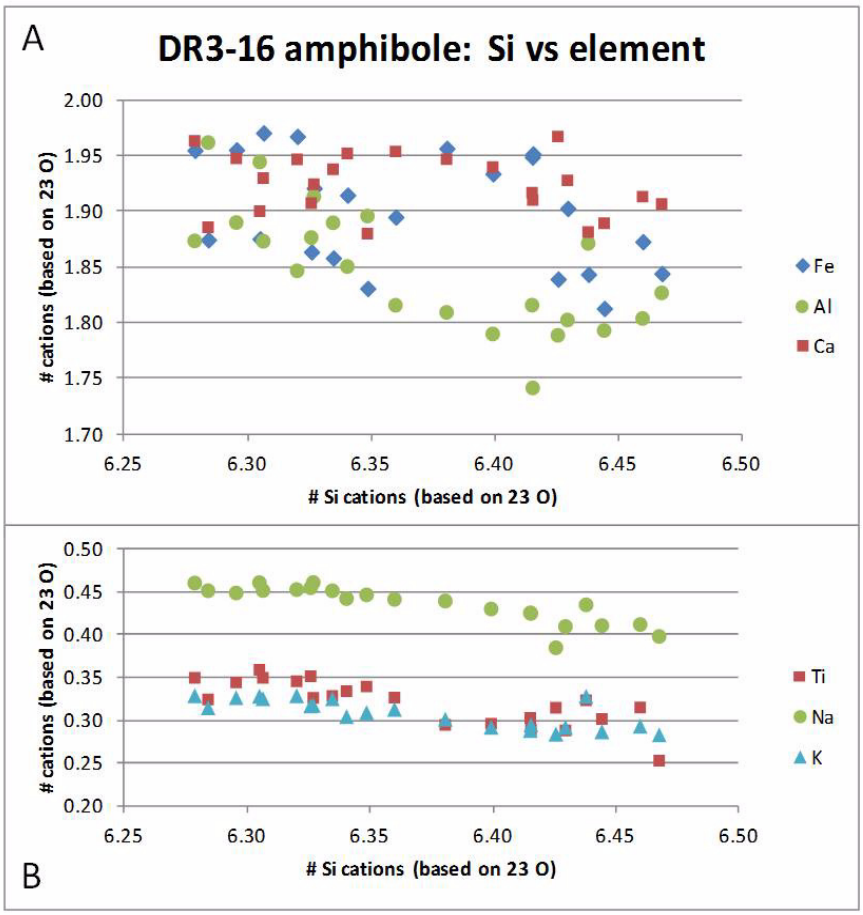

Figure 5-20: DR3-16 amphibole Si vs. element graphs

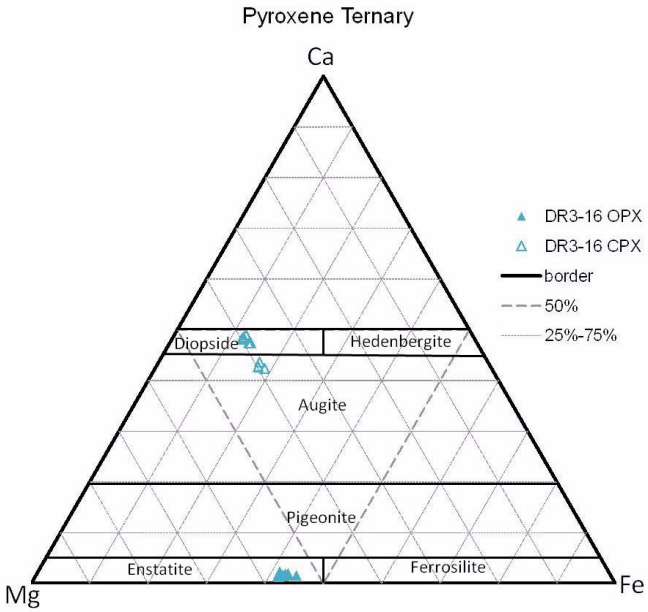

Figure 5-21: DR3-16 pyroxene classification

The biotite in sample DR3-16 is generally homogenous (Figures 5-4 and 5-5), no chlorite samples were found and no samples were rejected due to the effects of alteration to chlorite. The three samples of ilmenite analysed showed modest enrichment of Mn (Figure 5-3).

5.3 DISCUSSION

All samples show extensive metamorphic textures, including exsolution (for example, plagioclase/K-feldspar and ilmenite/haematite intergrowths), and diffusion effects (for example, Ca and K migration in DR3-2 plagioclases Figure 5-4). The original crystal shapes have been lost to metamorphic growth, recrystalisation and annealing effects in all but a few biotite and the zircons.

Alteration of plagioclase to sericite (DR3-2 and DR3-6), biotite to chlorite (DR3-2 and DR3-15) and of sillimanite to pinite (DR3-15) are all considered to be retrograde textures formed as the samples cooled after peak metamorphism.

Samples DR3-1, DR3-2, DR3-6 and DR3-15 all have perthitic textures in K-feldspar to a greater or lesser degree. Passchier and Trouw (1996) suggest rims and flames can form by exsolution replacement processes which proceed preferentially at sites of intracrystalline deformation such as where two feldspar grains touch. They also suggest the flame structures start to occur at low-medium metamorphic grade becoming more abundant at higher temperatures. At low to medium metamorphic grade the feldspar grains have less strain and show little flame perthite. On this basis, the extensive nature of the perthite flame structures in DR3-1 and DR3-6 suggests a higher temperature metamorphic event has altered the sample compared with DR3-2 which has only minor perthite structures.

Deer et al. (1966) indicate there is a complete solid solution between haematite (Fe_2O_3) and ilmenite ($FeTiO_3$) at temperatures over 1050^oC, that is, in the high temperature granulite or eclogite facies. As the solution cools lamellae of the ilmenite and haematite form. They also suggest ilmenite is common as an accessory mineral in granulite facies orthogneisses. These lamellae are prominent in samples DR3-1 and DR3-6. Sample DR3-2 shows exsolution activity with ilmenite blebs instead of lamellae, associated with haematite, while DR3-15 has no exsolution textures, displaying discrete ilmenite crystals in the matrix and both ilmenite and rutile as inclusions in the garnets. This suggests that both DR3-1 and DR3-6 are orthogneisses and underwent a granulite facies metamorphic event while DR3-2 did not reach such high temperatures.

Ti concentration is considered to be a proxy for temperature (Henry et al., 2005). The similar Ti concentrations for DR3-15 (the biotite inclusions are towards the rim of the garnet), DR3-16 and the bulk of DR3-2 (Figure 5-5) suggests that the biotites were all formed at roughly the same temperature. The low Ti biotites in DR3-2 (Figure 5-5 and Figures 5-8, 5-9 & 5-10) suggests that these were formed on either the prograde or, more likely, the retrograde path from the peak metamorphic conditions.

Vernon (2004) indicates that glomeroporphyritic zircon can either nucleate, drift together and grow or nucleate close together then grow. The texture is indicative that the zircons results from an igneous melt. These were seen only in DR3-2 suggesting that sample is igneous in origin.

The garnets in DR3-15 provide an insight into the conditions of formation during their growth. There appears to be three phases of garnet growth (Figure 5-15). Andesine and rutile inclusions in the centre of the garnets indicates a high temperature environment (Deer et al., 1966) for the initial garnet formation. High Ca concentrations in both the garnets and the biotites and the presence of rutile in the garnet cores indicates a high pressure environment

during formation. This high pressure and temperature environment appears to have been maintained for a period (where the Ca and Fe concentrations are flat in Figure 5-15 A(i) and (ii)) then the pressure eased to allow Fe substitution for Ca as the garnet continued to grow. This is likely to be upper amphibolite to granulite facies (Carlson, 2002) as Mg is flat indicating the high temperature was maintained. Subsequently, the temperature decreased to below lower amphibolite facies (Carlson, 2002) where Ca is unable to diffuse, causing the formation of a rim on the garnets where Fe is substituting for Mg and the Ca concentration is flat (Figure 5-15).

Plagioclase in DR3-15 reflects a similar scenario where high temperature andesine occurs in the garnet cores while oligoclase, formed at relatively lower temperatures is found in the matrix. The distinct edge to the Ca migration in the plagioclase in DR3-2 (Figure 5-7) also suggests there was extensive Ca diffusion which was halted as the temperature decreased on the retrograde path.

This temperature lag behind the pressure reduction is typical of tectonic uplift (Winter, 2001) or it may indicate two metamorphic events have occurred. The zoning pattern could also be due to a phase change (biotite breakdown for example) during cooling.

The mineral combination of pargasite (amphibole), enstatite (orthopyroxene) and augite and diopside (clinopyroxene) indicates that DR3-16 has a mafic protolith, and has undergone metamorphism at conditions from amphibolite to granulite facies (Bucher & Frey, 2002). The presence of ilmenite in the sample indicates the formation temperature was from 600 to 800^{o}C with pressure between 0 and 1.6 GPa (Ernst & Lui, 1998). Averaging the Ti content across the 25 amphibole analyses gives 0.30 Ti cations per 23 oxygen with a standard deviation of 0.07, which indicates that the amphiboles were formed under granulite facies metamorphic conditions (Raase, 1974). This sample is likely to have undergone the following metamorphic reaction (Deer et al., 1966):

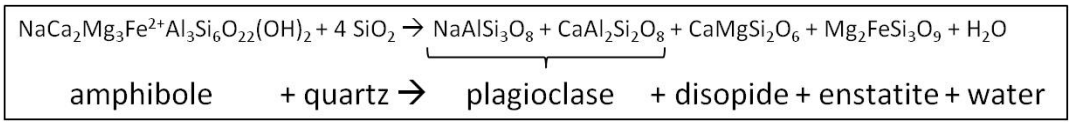

Figure 5-22: DR3-16 metamorphic reaction

The sample now shows no quartz, so this reaction could have continued until all the quartz in the sample was consumed. Deer et al. (1966) suggest this reaction will occur with high temperature and decreasing pressure: similar conditions seen in the formation of the garnet towards the rim in DR3-15, perhaps on the retrograde path from the metamorphic peak.

This analysis confirms, from the petrography, that DR3-15 is of pelitic origin and indicates that DR3-1, DR3-2 and DR3-6 are both most likely of igneous origin. DR3-1 and DR3-6 have undergone granulite facies metamorphism which has caused any hydrous minerals, such as biotite which may have been present to breakdown, so they are now anhydrous. By contrast, DR3-2 has undergone slightly lower temperature amphibolite metamorphism which has preserved the hydrous biotite minerals. DR3-15 and DR3-16 also both show evidence of granulite facies metamorphism. This implies that all samples have a shared metamorphic history.

CHAPTER 6: MAJOR & MINOR ELEMENTS

Chapter six continues the examination of DR3-1, DR3-2, DR3-6 and DR3-15, by investigating the major and minor element concentrations in whole rock samples to confirm their protolith and add to the understanding of their origin. No further analysis of DR3-16 was undertaken.

6.1 METHOD

Selected pieces sawn from the original sample were crushed using a hydraulic press, which was thoroughly cleaned between samples to avoid contamination. Altered parts of the sample were avoided where possible, however, DR3-2 and DR3-15 showed alteration on many internal faces making it difficult to get clean unaltered chips of the samples. The chips were then ground to a fine powder on a tungsten mill which was cleaned and dried with both distilled water, and ethanol between each sample, thereby avoiding contamination between the samples.

Loss on ignition (LOI) was determined on each sample. Approximately a gram of sample was weighed then heated in a furnace to 1000^{o}C for an hour. Samples were then cooled in a controlled environment and re-weighed. LOI data is included in Table 6-1.

Major element analysis was undertaken on fused borate glass discs of the sample created by mixing 0.3g of the sample with 2.5g of lithium metaborate flux by Peter Weiland of the GAU GEMOC Macquarie University. The glass discs were analysed by x-ray fluorescence (XRF) on a Spectro X-LAB 2000 at the University of Wollongong. The results are in Table 6-1. BVO-2 and BIR-1 standards are in use in the Wollongong facility

Sample	DR3-1	DR3-2	DR3-2 calc	DR3-6	DR3-15	LLD
SiO_2	77.32	89.78	67.94	76.79	72.91	0.01
TiO_2	0.08	0.09	0.37	0.47	0.27	0.01
Al_2O_3	13.27	4.92	15.81	11.34	15.33	0.03
Fe_2O_3	0.55	0.67	2.84	3.06	2.37	0.01
MnO	<LLD	<LLD	0.03	0.01	0.01	0.01
MgO	< 0.01	< 0.01	1.11	0.60	0.13	0.01
CaO	0.48	0.33	2.51	1.07	1.09	0.01
Na_2O	0.20	< 0.02	3.55	0.13	0.98	0.02
K_2O	6.34	1.76	4.69	3.55	5.81	0.01
P_2O_5	0.13	0.12	0.06	0.11	0.16	0.01
SO_3	0.053	0.029		0.028	0.037	0.010
LOI	0.78	1.06		1.32	3.84	
Total	99.20	98.76	98.91	98.47	102.93	
ASI	1.89	2.35	2.20	2.39	1.94	

Table 6-1: DR3 major element analyses with LLD (all values are wt% oxide)

Trace element concentration in the whole rock was determined by making a pressed pellet of each sample by mixing 5.3-6g of sample powder with 12 drops of polyvinyl acetate dissolved in ethanol in an aluminium cup. This mixture was then pressed to 4-5 tons in a hydraulic press to make the pellet and dried to remove the ethanol. Ethanol was used to clean the press between samples. These pellets were then used to determine the minor element concentrations by XRF using a Spectro XLAB2000 energy dispersive X-ray spectrometer at the GAU GEMOC facility at Macquarie University.

BHVO-2 and BCR-2 were used as a standard for the analysis (Appendix C, Table Appx-7). Comparing the measured value with the published values (from Wilson, 1997 and Wilson, 1997b) indicates the accuracy of the analyses is within the error margin specified for the standard for the majority of the elements. For BHVO-2, where the values are a little high (Cr) or low (Co, Ga, La, Ce and Nd) the measured values are within 2 sd of the values published by Wilson (1997). The measured Hf value however is below detection limit (2.0 μg/g), whereas the published value is 4.1±0.3 μg/g. For BCR-2 the majority of elements are within one 1 sd, with Fe, La, Hf, Pb and Th within 2 sd. The measurements of elements Ce, Mo and Cr are slightly low, while Pr is slightly high, so care should be taken when interpreting the minors data with respect to these elements.

6.2 RESULTS

Due to the random nature of dredging for rock samples, only single analyses of each rock were undertaken. Unfortunately, the analysis of DR3-2 appears to be erroneous with an SiO2 content of 89.78% (Table 6-1) which would indicate a very high mode of quartz. From the petrographic and mineral analysis in the previous chapters, this is clearly not the case. A calculation using average minerals from the EMP data and the modes from the petrography analysis was undertaken (Table 6-1 with calculation details in Table Appx-5) and is plotted with the measured DR3-2 data where appropriate. This gives only indicative measurements and the major analysis should be repeated. The discussion focuses on the calculated major element data rather than the measured data. The minor element analysis is considered valid (Table Appx-8).

6.2.1 Major element analysis

The whole rock data for the rock samples considered to be granite gneisses (DR3-1, DR3-2 and DR3-6) have been plotted on a Total Alkali versus Silica (TAS) diagram (Middlemost 1994) in Figure 6-1(A). The composition for DR3-1 and DR3-2 plot in the granite field while DR3-6 plots in the tonalite field.

In the ACF diagram, Figure 6-1B all samples have been plotted and all fall within the claystone and psammite area defined by Vernon and Clarke (2008). All samples have very low levels or levels below detection limits of FeO, MgO, MnO and CaO so the graph is dominated by the Al_2O_3 and K_2O values in the whole rock analysis. The samples are all peralluminous with aluminium saturation indexes (ASI) using the formula below, from 1.89 to 2.39 (Table 6-1).

$$ASI = \frac{Al_2O_3}{(Na_2O + K_2O + CaO)}$$

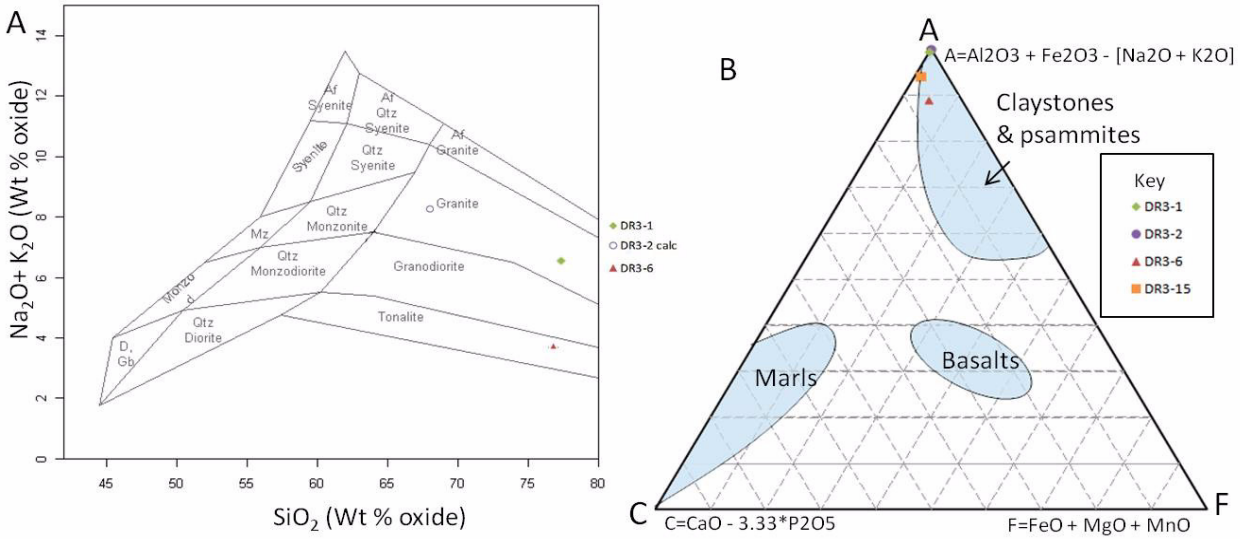

Figure 6-1: Major element classification diagrams: A TAS classification diagram created in GCD Kit V3(Janousek et al., 2006), attributed to Middlemost (1994). B ACF ternary diagram (from Vernon & Clarke, 2008)

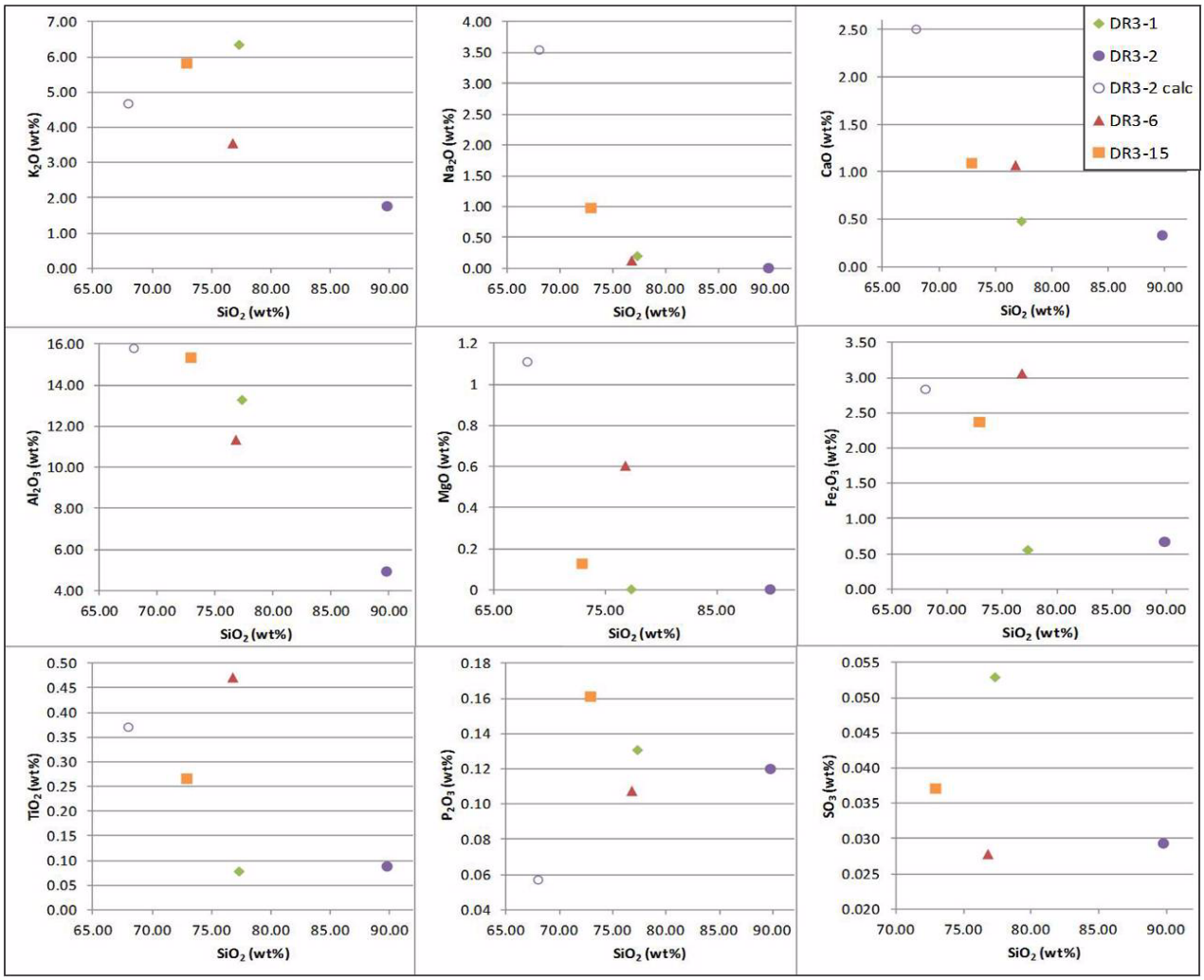

Figure 6-2: Harker diagrams of SiO_2 versus the major element oxides. Where the concentration is < LLD these have been plotted as zero.

The whole rock data (Table 6-1) shows high levels of SiO_2, from 67 to 77%, so the samples are all felsic. Harker diagrams of SiO_2 versus the major elements in Figure 6-2 show that none of the samples cluster together so all samples are considered to be from separate rock outcrops, with separate protoliths, though these could have undergone similar metamorphic processes. The data is discussed below.

6.2.2 Minor element analysis

Harker diagrams of the minor elements versus SiO_2 have been included in Figures 6-3 and 6-4. These have been grouped into siderophile, large ion lithophile, high field strength and rare earth elements as the elements within each group generally behave similarly (Winter, 2001).

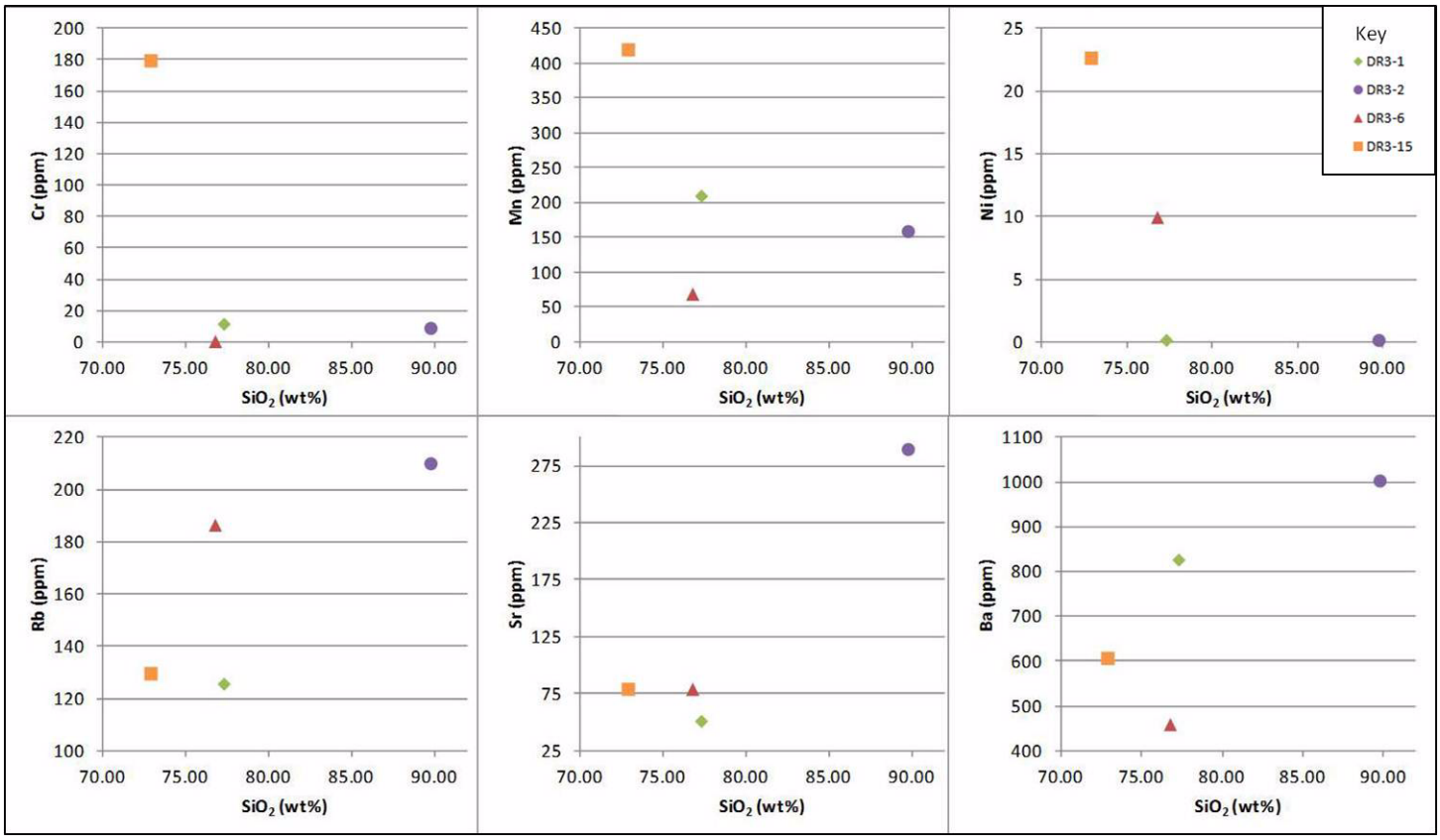

Figure 6-3: Selection of Harker diagrams of SiO_2 versus siderophile and large ion lithophile minor elements

DR3-15, the paragneiss, has the highest concentrations of siderophile elements (represented by graphs of Cr, Mn and Ni in Figure 6-3) which would have concentrated in the garnet and ilmenite minerals with any Fe. By contrast, the orthogneisses have generally lower siderophile concentrations though this is not reflected in lower Fe_2O_3 concentrations.

The large ion lithophile elements are represented by graphs of Rb, Sr and Ba in Figure 6-3. DR3-2 has consistently higher concentrations than the other samples. These differences most likely reflect the differences in protolith and magma conditions, including the presence or absence of vapour phases for the igneous events affecting the samples.

The Harker diagrams of the high field strength (HFS) elements, represented by Y and Zr in Figure 6-4 indicate that the DR3-1 and DR3-6 orthogneiss samples have higher Zr and Y values than the other samples (DR3-2 and DR3-15). Zr is usually present in the sample as zircons. Y and the rare earth elements (REE), represented by La and Ce in Figure 6-4 usually concentrate in the zircons. La, Ce and Th also concentrate into the monazite minerals. An analysis of Y in the zircons is undertaken in Chapter 7.

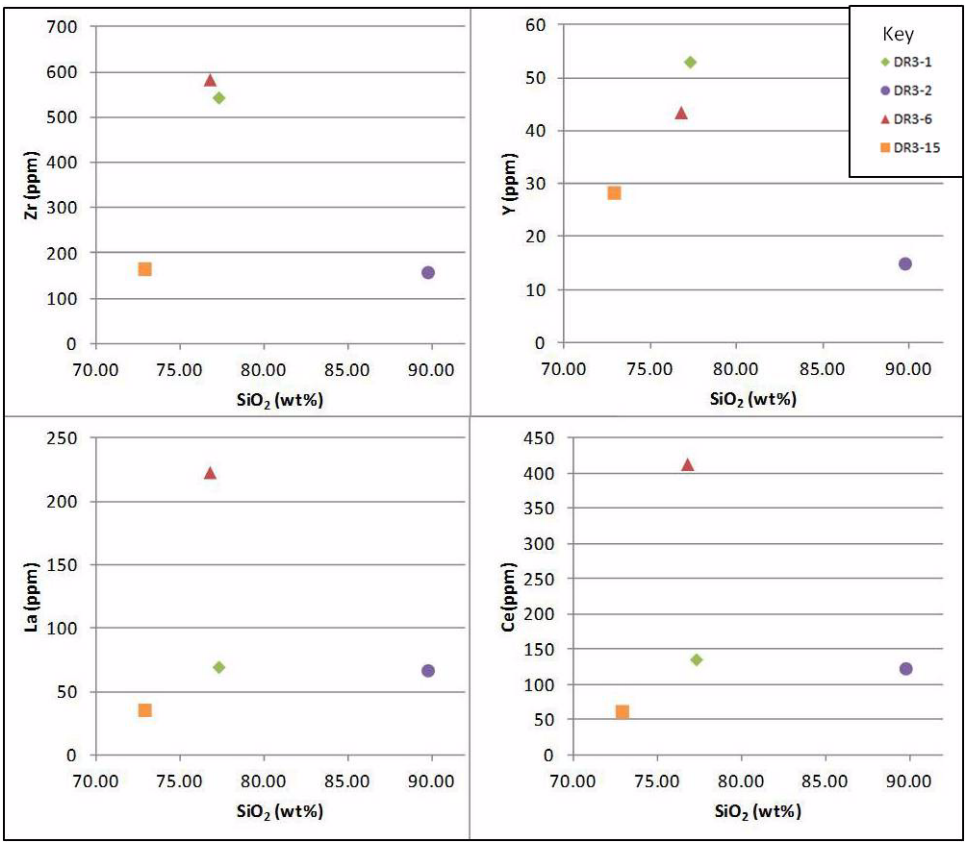

Figure 6-4: Selection of Harker diagrams of SiO_2 versus high field strength minor elements

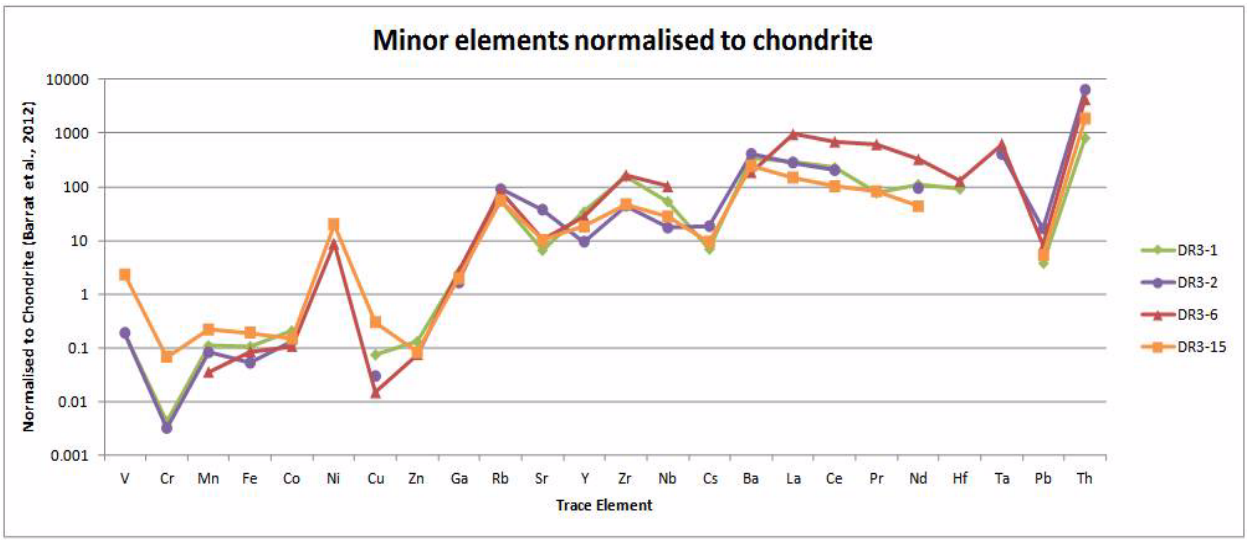

Figure 6-5: Minor elements normalised to chondrite (from Barrat et al., 2012)

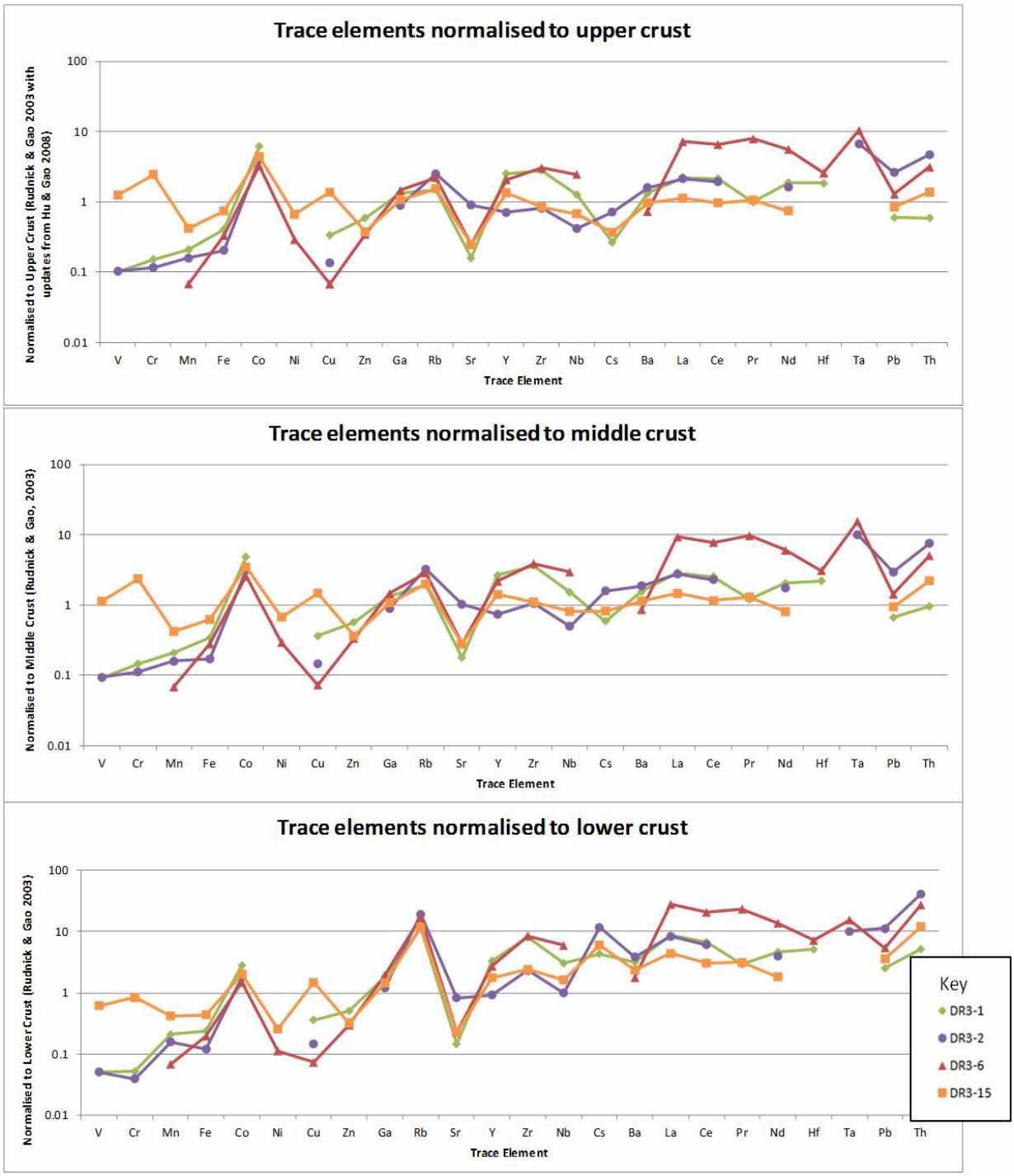

Figure 6-6: Minor elements normalised to lower, middle and upper continental crust compositions (Rudnick & Gao, 2003)

Figure 6-5 compares minor element concentrations to chondrite values (from Barrat et al., 2012) and shows sample DR3-6 has the highest concentration of REE. The samples are generally depleted in the siderophile elements, except for Ni in samples DR3-6 and DR3-15 and enriched in the LIL, HFS and REE elements which would be expected of samples with a continental crust origin.

Figure 6-6 includes similar spider diagrams of the minor trace elements against the lower, middle and upper crust. Average crustal values were taken from Rudnick and Gao (2003)

with updates from Hu and Gao, 2008 for the upper crustal values. Compared with the lower crust values, the samples are all depleted in siderophile and enriched in LIL, HFS & REE elements. DR3-15 generally matches the values for upper continental crust while the other samples, show some additional depletion in siderophile elements except for Co. Additionally, DR3-2 and DR3-6 show minor enrichment of REE compared with upper continental crust.

6.3 DISCUSSION

6.3.1 Major elements

The calculated DR3-2 sample has the highest Na_2O and CaO concentrations (Figure 6-2) reflecting the higher mode of oligoclase to andesine plagioclase (40%) in that sample, though as these are very mobile elements the lower concentrations in the other samples may be due to leaching processes removing the elements. All samples have similar K_2O reflecting the modes of K-feldspar and/or biotite in the samples.

Samples DR3-1 and DR3-6 have slightly lower Al_2O_3, perhaps due to the loss of biotite from those samples, though DR3-15 as a metapelite would be expected to have a higher Al_2O_3 concentration than the orthogneisses.

MgO is concentrated in biotite in DR3-2 (calculated) which has given this sample the highest concentration. The MgO concentration for DR3-15 is unusually low as the presence of both biotite and garnet in the sample should increase the MgO concentration.

The Fe_2O_3 and TiO_2 Harker diagrams are very similar as these oxides both concentrate in the opaques and/or biotite and garnet minerals. Relatively lower levels in DR3-1 reflect the lack of biotite and lower mode of opaques in the sample.

P_2O_5 concentrations are overall quite low (Figure 6-2), but higher in DR3-15 and DR3-1 compared with the other samples, reflecting the presence of apatite, $Ca_5(PO4)_3$ in DR3-1 and monazite, $(Ce,La,Th)PO_4$ in DR3-15 as accessory minerals. The calculated DR3-2 concentration is likely to be too low as it too has monazite as an accessory mineral however, monazite was not considered during the calculation. DR3-6 has neither of these minerals. SO_2 concentrations are negligible for all samples indicating there are no metal sulphide minerals in the samples.

6.3.2 Minor elements

In the previous chapter DR3-1 was found to have much higher Mn levels in the ilmenite (Figure 5-3) than seen in the other samples. This could explain the higher Mn concentration seen in Figure 6-3.

The spider diagrams indicate that in general the samples are more depleted in siderophile and enriched in REE than the standard upper continental crust as defined by Gao and Hu (2008). Chappell and White (2001) suggest that the Rb/Sr ratio will increase with increasing fractionation. Samples DR3-1 and DR3-6 both show a Sr depletion compared to average upper continental crust, this is also reflected in the Sr Harker diagram in Figure 6-3 and lower plagioclase modes for the samples (Table Appx-6), suggesting plagioclase was fractionated from the magma before forming these samples. In contrast, DR3-2 has a higher

plagioclase mode, and no Sr depletion suggesting that the magma was either not fractionated, or accumulated plagioclase.

6.3.3 General

Chappell and White (2001) in a review of their seminal 1974 paper define an S-type granite (that is, having a sediment protolith), as having depleted Na, Ca and Sr due to these elements being lost as the plagioclase in the sediment protolith is altered to clay, but enriched in K, Rb and Pb as these elements are taken up by the clays. They also suggest a high SiO_2 content and an ASI of over 1.1 defines an S-type granite. Using this criteria it can be seen that both DR3-1 and DR3-6 are most likely S-type granites. DR3-2 could possibly be an I-type granite as it has elevated Ca, Na and Sr elements though a re-analysis of the major elements should be done before any conclusions are drawn. Chappell and White (2001) also suggest that S-type granites form in a relatively lower temperature environment compared with I-type granites.

Pearce (1996) suggests that based on the Rb and (Y+Nb) concentrations an indication of the tectonic setting for the source of the granites can be determined. The DR3-1 and DR3-6 orthogneisses plot in the within plate granite, and the post collision granite fields (Figure 6-7). Pearce (1996) also suggests that post collision granites would have upper continental crust compositions which agrees with the spider diagrams for the samples (Figure 6-6). The calculated DR3-2 sample plots close to the boundary between volcanic arc and syn-collision granites, which suggests that this sample is from a magma generated in a different environment to the other orthogneisses.

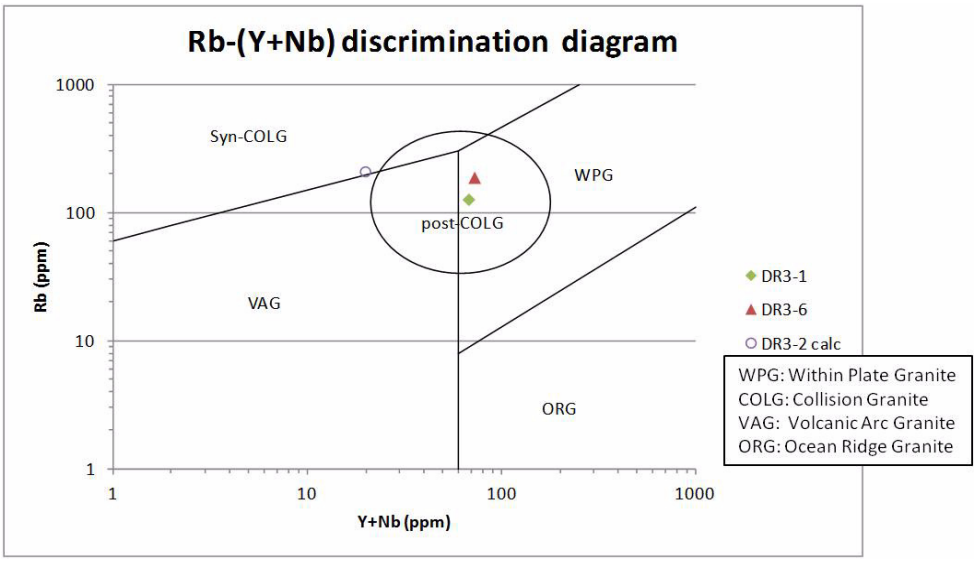

Figure 6-7: Tectonic setting: Rb vs. (Y+Nb) (after Pearce, 1996)

CHAPTER 7: ZIRCON MORPHOLOGY AND COMPOSITION

Zircons are resistant to chemical alteration and physical weathering, and will concentrate light and heavy REE, Y, Hf and U into the crystal structure, with often very little diffusion occurring. Because of these attributes, zircon formation can be dated, they reflect the REE environment in which they grew, and can be used to determine the often complex history of the rocks containing them (Rubatto & Hermann, 2007).

So, focus now moves from the minerals making up the rock and the whole rock analysis, to the zircons extracted from the samples. In this chapter the zircons are sorted into morphological groups and their compositions are investigated, using Y and Hf as a proxy for REE and U (Rubatto & Hermann, 2007). In subsequent chapters the U-Pb and Lu-Hf isotope systematics will be investigated.

7.1 METHOD

Zircons were extracted from each sample by a series of well established steps used at the GEMOC facility in Macquarie University. Pieces of each sample were processed by SelFrag© which subjects the whole rock to high voltage pulses which causes the rock to fragment along the crystal boundaries. In this way the crystals suffer the least damage. The output from the SelFrag© process was sieved through a 300 μm sieve. As the zircons are dense and usually very small, the fine fraction was then panned to remove the light minerals. Magnetic minerals were removed initially with a hand magnet for DR3-1, DR3-2 and DR3-6, then all samples were put through a Frantz© Magnetic Separator to remove the last of the magnetic minerals, including the garnets in DR3-15. Further concentration of the zircon fraction was undertaken by panning in a watch glass. When a low yield of zircons was achieved initially for DR3-1 and DR3-2 additional material was also separated using heavy liquids. Great care was taken cleaning all equipment between samples to avoid contamination.

Zircons were selected under a reflecting light microscope and mounted in epoxy for analysis. All analyses were undertaken at the GEMOC facility at Macquarie University. backscatter electron (BSE) and cathodoluminescence (CL) images of all zircons were taken on a Zeiss EVO MA15©. Electrons were accelerated from a tungsten filament at 15KeV, providing a beam current of 15 nAmps. X-rays generated from the sample were counted on the backscatter and cathodoluminescence detectors. A Bruker Quantax© energy dispersive X-ray spectroscopy (EDS) which used the same beam conditions and Esprit software was used to display elemental compositions of selected spots on the zircons and their inclusions.

The mounted zircons were then polished and coated with carbon approximately 200 Angstrom thick. The elements specified in Table 7-1 were measured in the Cameca SX100 electron microprobe (EMP) which has 5 crystal spectrometers and an energy dispersive system. Electrons were accelerated from a tungsten filament at 15 KeV, providing a beam current of 20 nAmps onto a spot size of approximately 1 μm. A count time of 10 seconds for the peak with 5 seconds either side of the peak was used. The EMP was calibrated using Hf-wire (Hf), zircon (Si & Zr) and YAG (Yttrium Aluminium Garnet) crystal (Y). LLD for the elements was provided by the lab and is included in Table 7-1. Oxygen was inferred

using stoichiometry. Only zircon analyses with totals less than 85 wt% for samples DR3-1, DR3-2 and DR3-6 and 75 wt% for DR3-15 were rejected.

Detector	Element analysed	LLD (ppm)
1: LTAP	-	-
2: TAP	Si Kα	150
3: LPET	Y Lα	650
4: TAP	Zr Lα	550
5: LLIF	Hf Lα	1250

Table 7-1: EMP set up for zircon analysis

7.2 RESULTS

The morphology of the zircons is examined using Corfu et al., (2003) as a primary reference, unless otherwise specified. This is followed by an analysis of the EMP data on the zircon composition, based on the Y and Hf concentrations. For each sample graphs of Y_2O_3 and HfO_2 vs SiO_2 and ZrO_2 are included to highlight similarities and differences in composition between the morphological groups. The average, standard deviation (sd) and %rsd was calculated for each morphological group within each sample (Table Appx-9). Where %rsd is from 10% to 25% this is considered to show minor variation within the group, %rsd 25% to 100% is moderate and over 100% is extensive variation. Standard error is used for all error bars. No core to rim comparisons were made for the groups of homogenous zircons (that is, group 1 in DR3-2 and DR3-15 and group 4 in DR3-6.)

The site of EMP probing has been included in the CL images: red for cores, blue for rims and green for extra analyses. U-Pb isotope analyses were undertaken at the site of the orange circles and Lu-Hf isotope analyses were undertaken at the site of the blue circles. These systematics are investigated in later chapters.

7.2.1 DR3-1: Two feldspar-quartz orthogneiss

The zircons from DR3-1 were sorted into three groups along morphological lines. The first group (Figure 7-1) of 54 zircons are doubly terminated, euhedral to subrounded shapes, from 44 to 200 μm long with a length:width ratio range from 1.1 and 3.3 though the bulk of the zircons are around 2.0. The CL images display complex growth histories, with usually a dark core surrounded by growth zoning. A number of zircons have a dark, perhaps xenocrystic core with a much brighter rim (Figure 7-1 #209). Recrystallization of the zircons is seen as textural discontinuities in the zoning (Figure 7-1 #1), as ghosting of the original zoning texture (Figure 7-1 #223 and 242) and as almost homogenous cores (Figure 7-1 #231).

Group 2 has 11 zircons (Figure 7-2) which are euhedral, from 84 to 185 μm long, with a length:width ratio concentrated in the 1.5 to 2.0 range. The internal characteristics seen in the CL images is less complex than for Group 1. Sector and growth zoning are both prominent, with some disruption of the zones by recrystalisation in some, but not all of the zircons (Figure 7-2 #203 and #218).

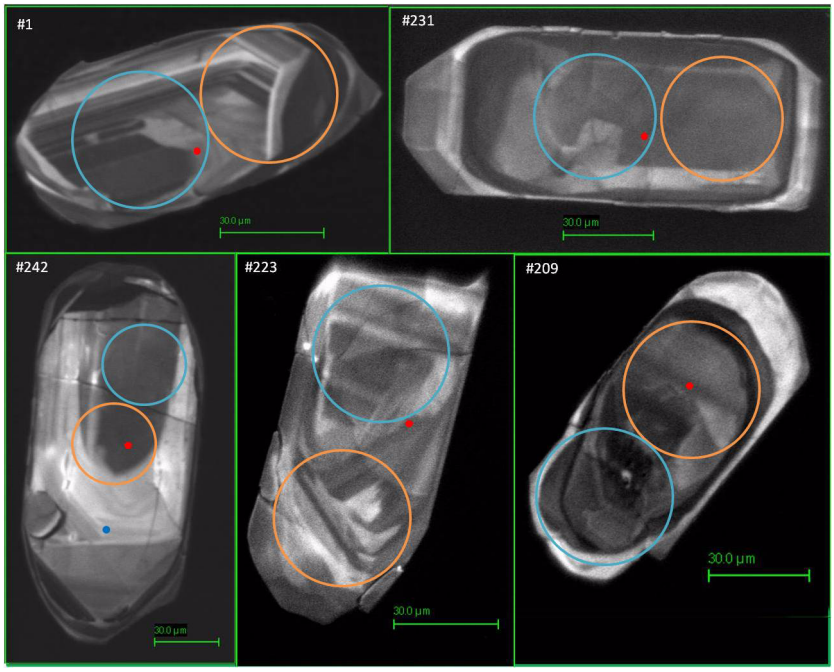

Figure 7-1: DR3-1 CL images of group 1 zircons

The group 3 zircons are a small number of very small (~60µm long, with a length:width ratio of 1.5 to 1.8.), anhedral zircons with homogenous interiors in the CL images.

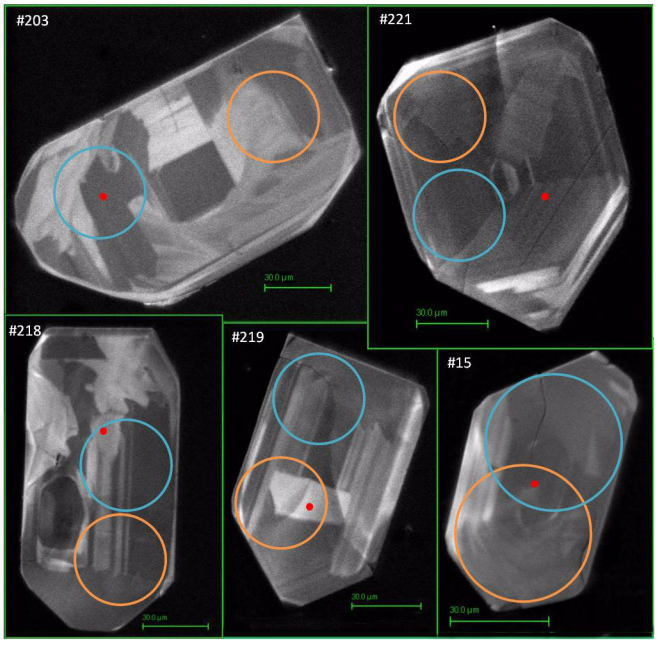

Figure 7-2: DR3-1 CL images of group 2 zircons

The Group 1 zircons show extensive variation for Y_2O_3 concentrations in the cores and to a lesser extent in the rims. Figures 7-3 A&B indicate there is a possible inverse linear relationship for a subgroup of the group 1 zircons cores between Y_2O_3 and SiO_2 and HfO_2.

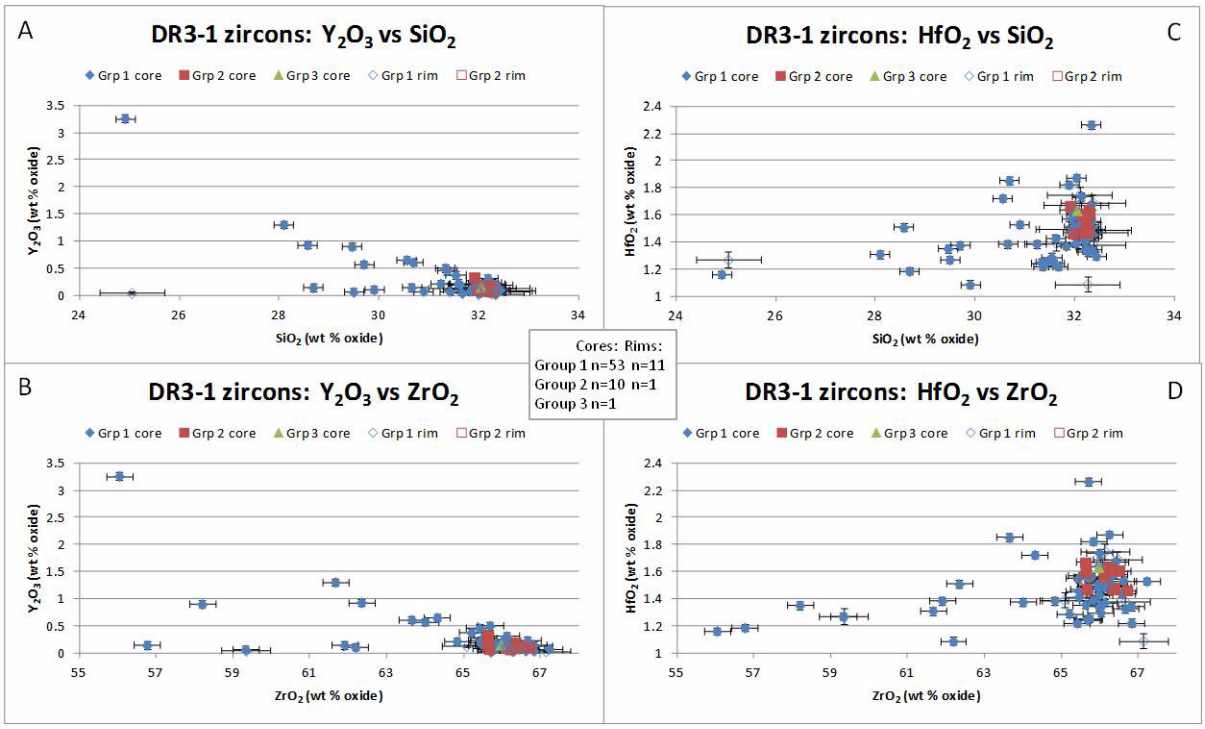

Figure 7-3: DR3-1 graphs of Y_2O_3 and HfO_2 vs. SiO_2 and ZrO_2

The group 2 zircons appear to be closely clustered with lower Y_2O_3 concentrations (Figure 7-3 A&B). However, closer examination of the population (in Figure 7-4 A&B) shows there is moderate variation for Y_2O_3, similar to the variation in group 1 rims.

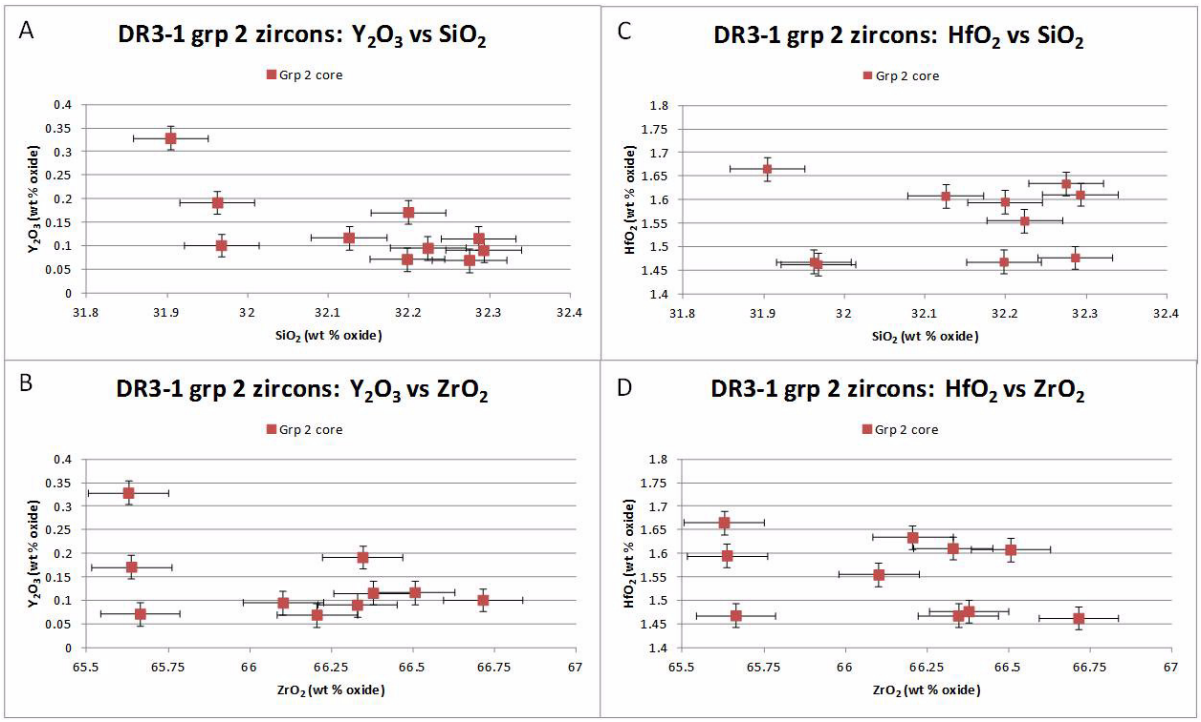

Figure 7-4: DR3-1 group 2 graphs of Y_2O_3 and HfO_2 vs. SiO_2 and ZrO_2

There is minor variation of HfO_2 concentrations for group 1 cores and rims, though no relationship with SiO_2 and ZrO_2 is evident (Figure 7-3 C&D). The group 2 zircons show no variation for HfO_2 suggesting they are a single population.

7.2.2 DR3-2: Quartz-feldspar-biotite orthogneiss

The zircons of DR3-2 were divided into three groups based on morphology. The first group of 24 zircons are small anhedral to subhedral, from 42 to 129µm long with a wide spread of length:width ratios from 1.6 to 4.0. The CL images show that the interiors are homogenous (for example #245 in Figure 7-5), chaotic (#209 in Figure 7-5) or have fine residual ghost zoning, and the rims may have a brighter edge (#37 and #209 in Figure 7-5).

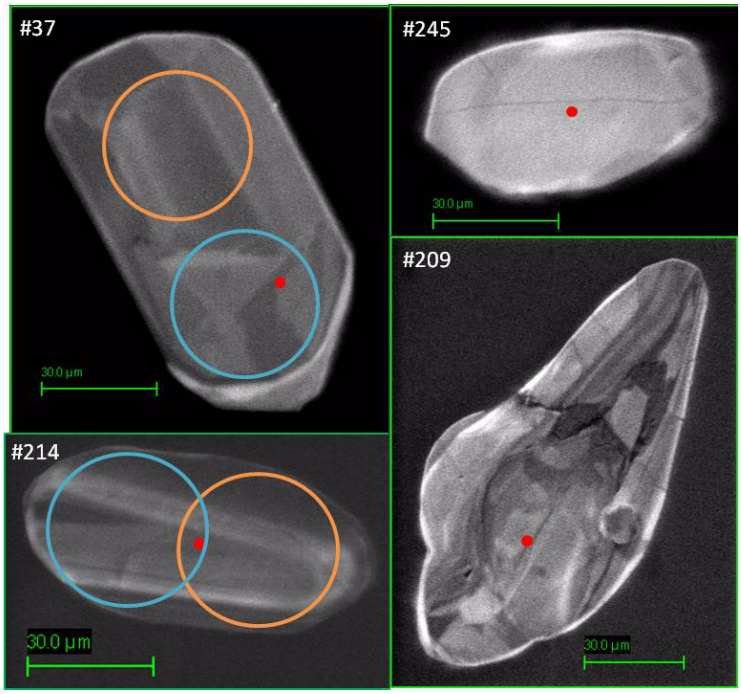

Figure 7-5: DR3-2 CL images of group 1 zircons

Group 2 consists of 52 zircons which are much larger, from 75 to 255µm and elongate with length:width ratios of 2.0 to 6.6. They are euhedral and the CL images all display a very bright band close to the rim of the zircons (Figure 7-6). The cores are usually dark and display oscillatory zoning with some recrystallization effects visible. Inclusions of quartz, K-feldspar and monazite were seen in approximately half the samples.

The third group of 19 zircons has some overlap with the group 2 characteristics, however, these all display a much lighter core and the residual oscillatory zoning in the core is either severely truncated (Figure 7-7 #240 and #241) or has been almost completely resorbed (Figure 7-7 #40 and #42). The zircons have a similar size range to group 2, and some display the bright band close to the rim, however, these are not all elongate, with many showing irregular shapes and inconsistent growth areas on the edges.

Figure 7-6: DR3-2 CL images of group 2 zircons

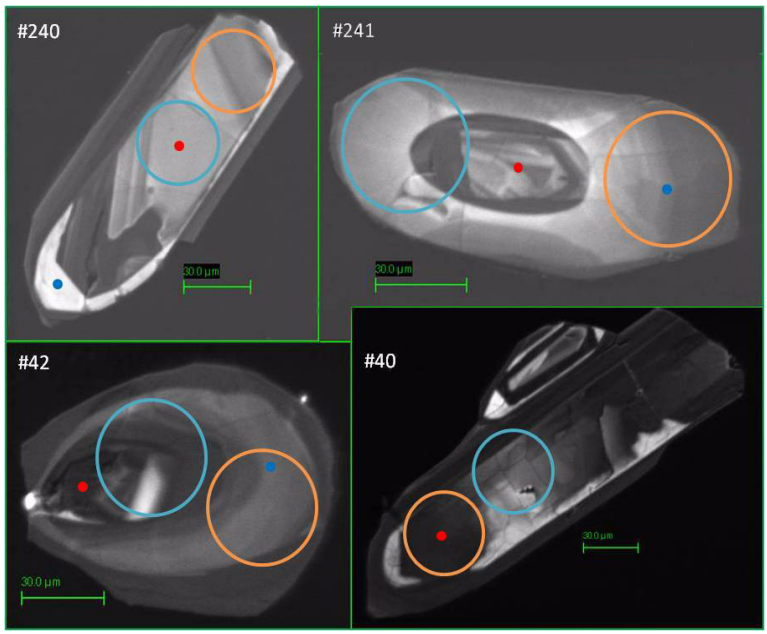

Figure 7-7: DR3-2 CL images of group 3 zircons

The composition of the zircons in DR3-2 shows extensive variation for Y_2O_3 within the cores for all group, with moderate variation in the rims where it was measured (Figures 7-8 A&B). Similarly to DR3-1, there is an inverse relationship between Y_2O_3 and SiO_2 and ZrO_2 concentrations.

DR3-2 also shows minor variation of HfO_2 and no relationship between HfO_2 and the SiO_2 and ZrO_2 values (Figure 7-8 C&D) within the group 2 and 3 cores and rims.

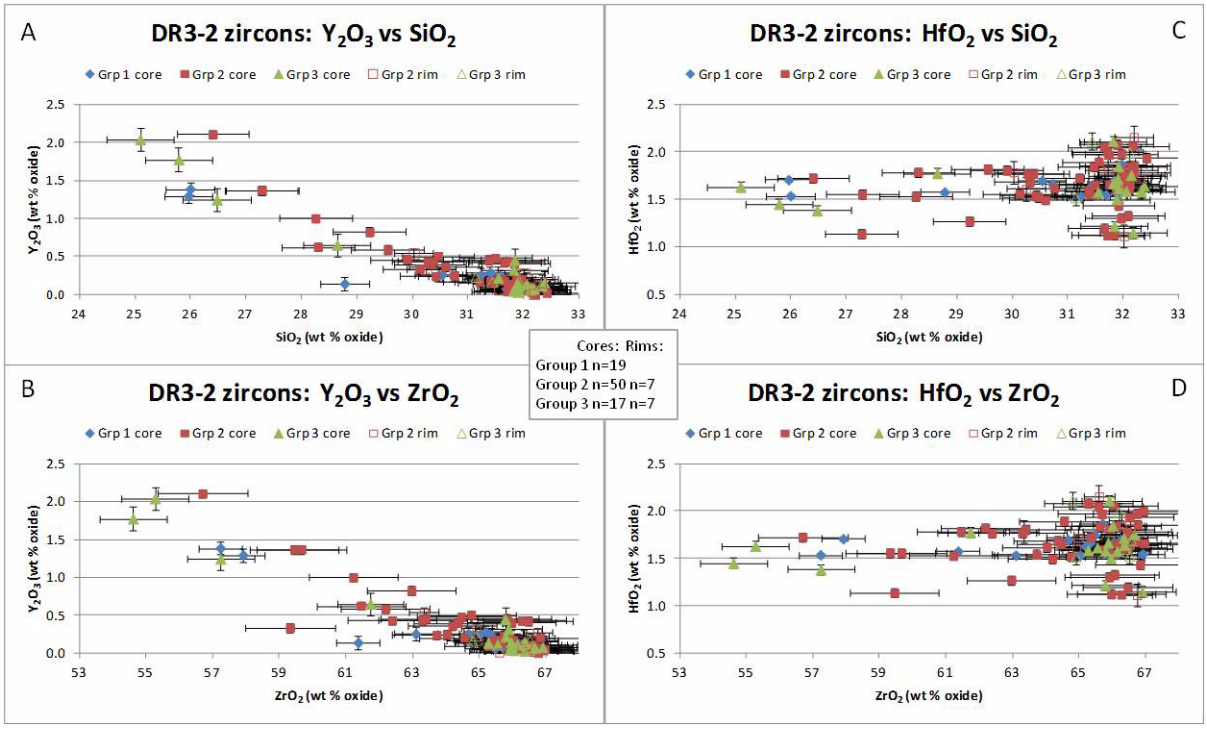

Figure 7-8: DR3-2 graphs of Y_2O_3 and HfO_2 vs. SiO_2 and ZrO_2

7.2.3 DR3-6: Two feldspar-quartz orthogneiss

Zircons from the DR3-6 samples were split into five groups. The first of these groups (Figure 7-9) has 29 zircons which are elongate and euhedral, from 100 to 300µm with a length:width ratio between 2.0 and 4.2. All zircons have a metamict core with fracturing from the core edge to the rim and a variety of inclusions of quartz, monazite, apatite, K-feldspar, and an undetermined phase of Al, Mg, Fe, Si and O (perhaps garnet or cordierite?). The core is surrounded by fine oscillatory zoning which shows minor recrystalisation.

The second group (Figure 7-10) of 43 zircons are also elongate and euhedral but are more variable in size than the first group, from 100 to 350µm with a length:width ratio of 1.3 to 4.0. They have similar oscillatory zoning to group one, with some recrystallization textures, however, their cores may be dark, but have no inclusions, are not obviously metamict and don't display core to rim fracturing.

Group 3 (Figure 7-11 #7, #50 and #60) has 21 zircons of anhedral to subhedral shape with lengths from 107 to 363µm and a length:width ratio of 1.5 to 4.2. They display strong recrystallization textures and may have some zoning on the rim.

The fourth group of 7 zircons are very similar in size and shape to the third group, however the recrystallization process has proceeded to the point where the zircon is virtually homogenous with little to no residual texture visible (Figure 7-11 #107 and #108).

The fifth group of nine zircons are all fragments (Figure 7-12) from 114 to 282mm. They display some oscillatory zoning and recrystallization textures.

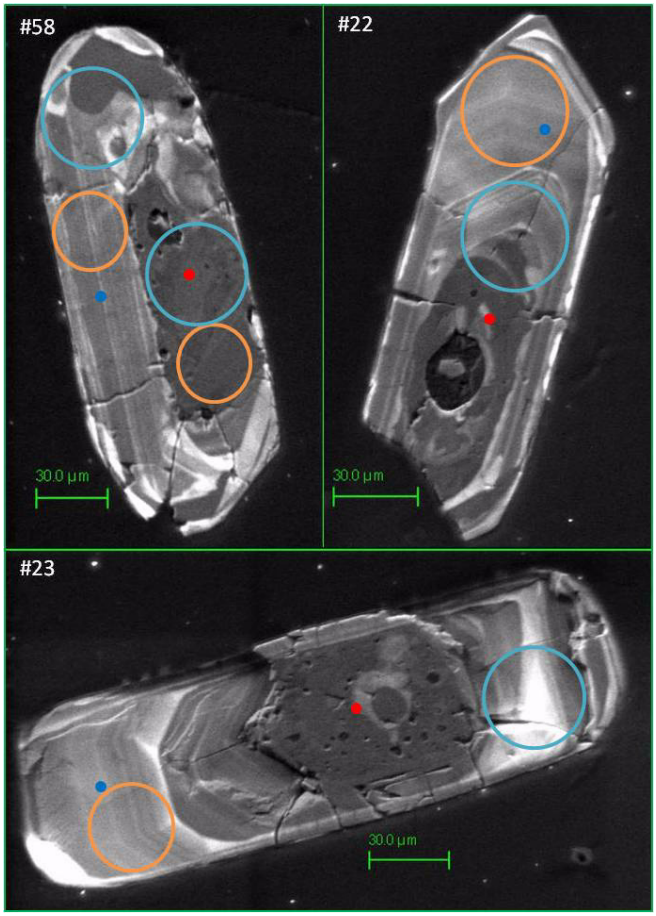

Figure 7-9: DR3-6 CL images of group 1 zircons

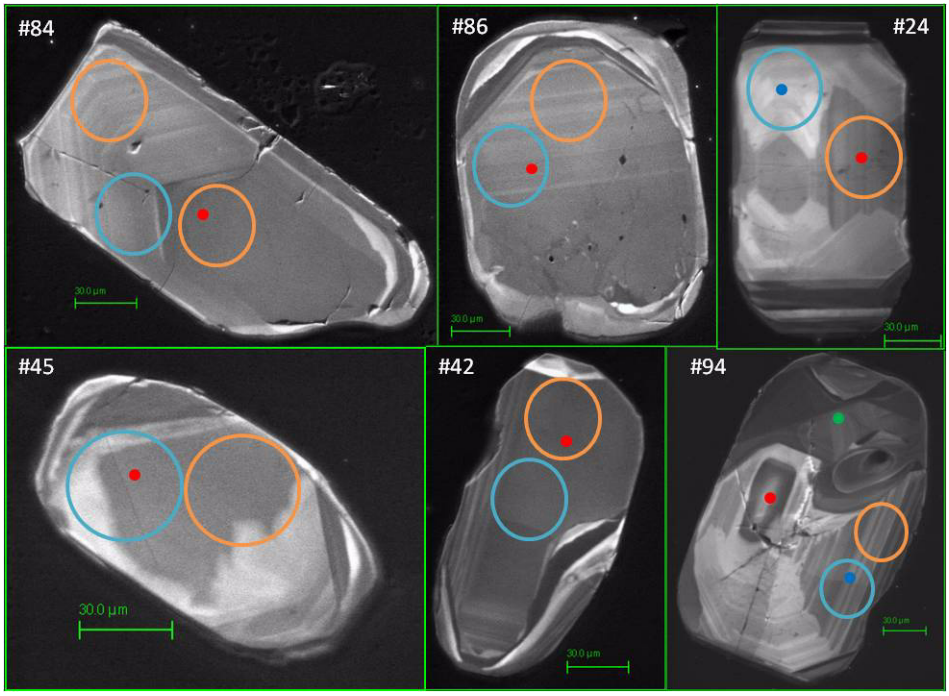

Figure 7-10: DR3-6 CL images of group 2 zircons

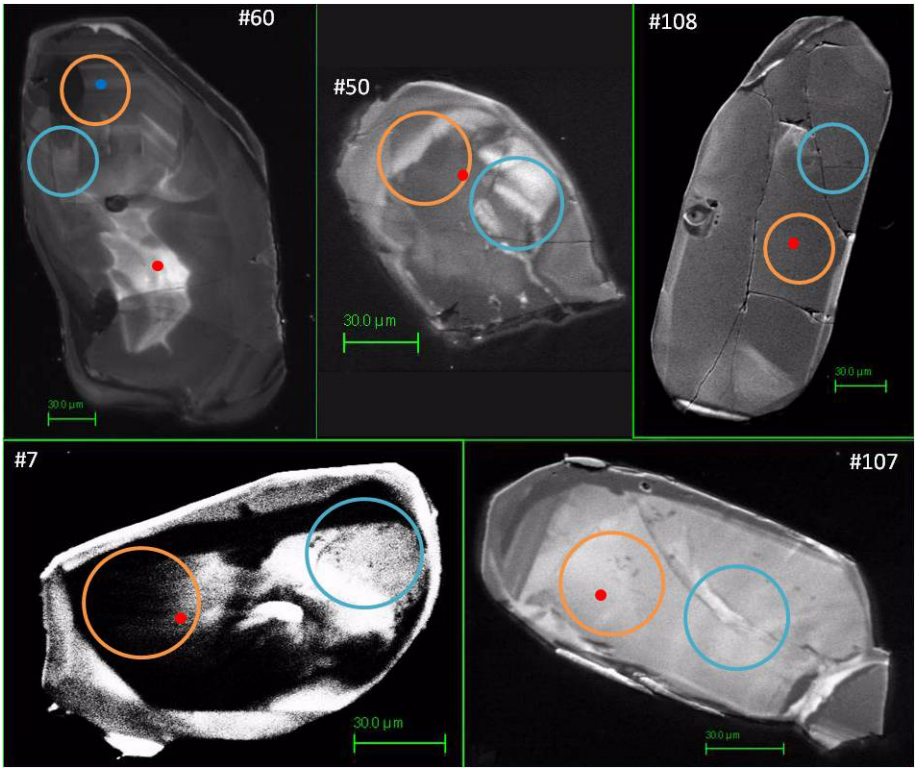

Figure 7-11: DR3-6 CL images of group 3 (#7, #50 & #60) and group 4 (#107 and #108) zircons

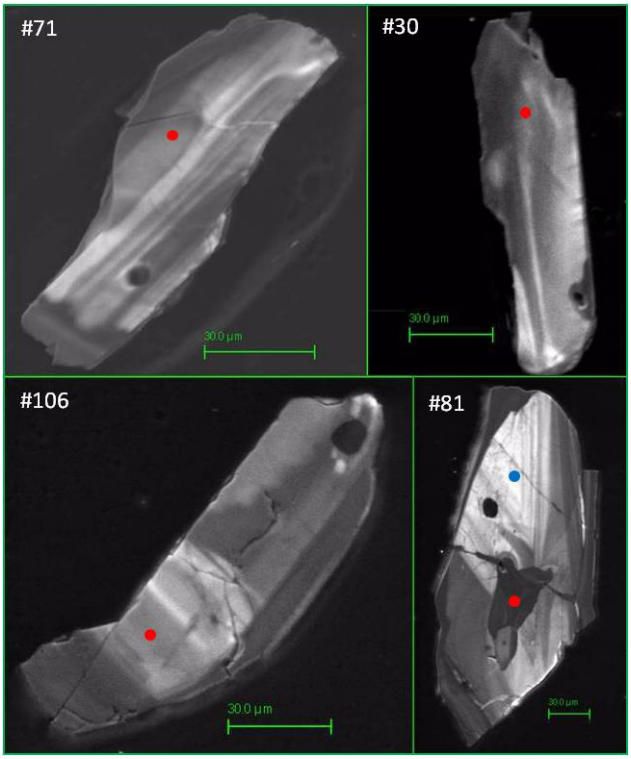

Figure 7-12: DR3-6 CL images of group 5 zircons

Figures 7-13 A&B indicate that, in contrast to DR3-1 and DR3-2, the zircons in sample DR3-6 have moderate variation in both cores and rims, but all have low Y_2O_3 (below 1.4

wt% oxide) concentrations and no linear relationship between Y_2O_3 and SiO_2 and ZrO_2 concentrations is evident. The cores of the zircons have marginally increased Y_2O_3 concentrations compared with the rims. The anomalous group 1 core and group 2 rim were not eliminated as they appear to be a valid analyses.

The HfO_2 graphs for DR3-6 (Figure 7-13 C&D) show a possible inverse linear relationship between HfO_2 and SiO_2 and ZrO_2 for a subset of the group 1 zircons. The y-axis on these HfO_2 graphs ranges from 0.5 to 5.5, double that seen in the previous samples. The group 1 cores show HfO_2 variation much greater than the groups 2 to 5. Groups 1, 2 and 5 have rims with less variation than the cores, while group 3 has increasing variation.

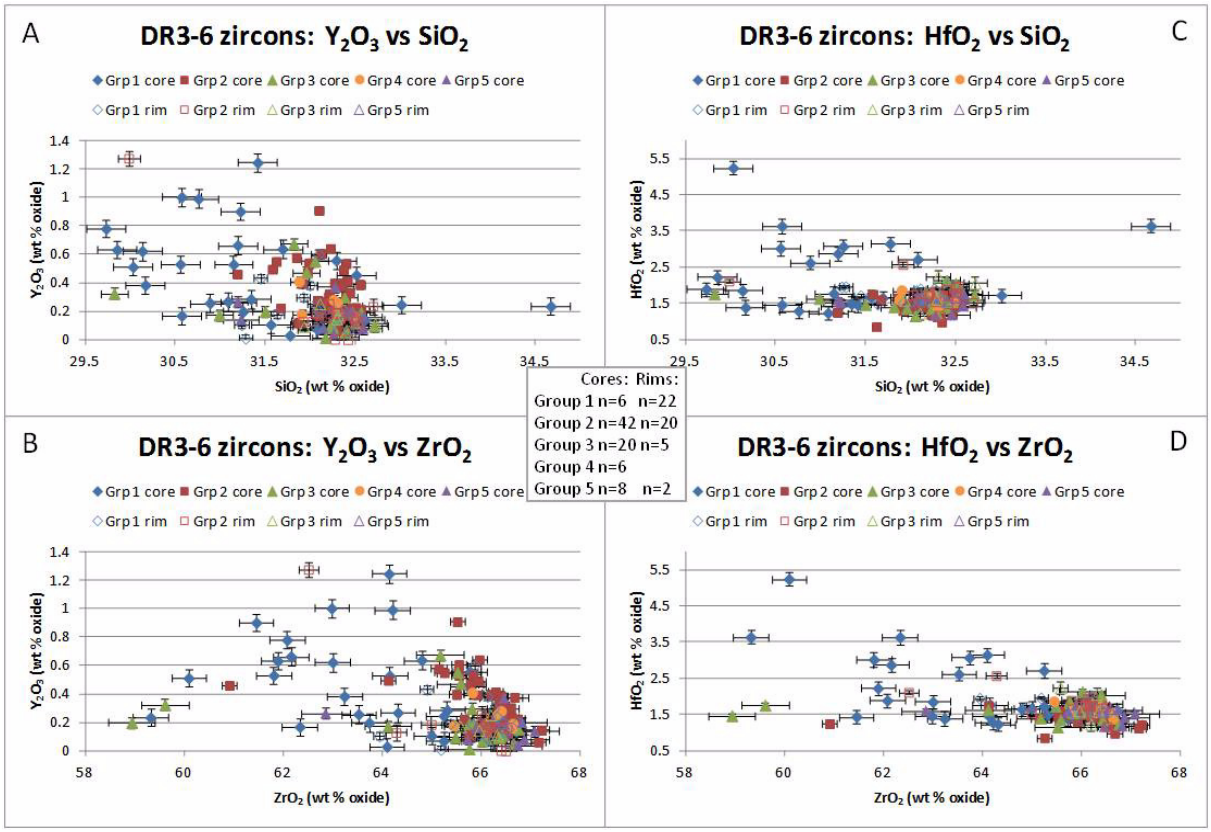

Figure 7-13: DR3-6 graphs of Y_2O_3 and HfO_2 vs. SiO_2 and ZrO_2

7.2.4 DR3-15: Garnet-sillimanite-biotite paragneiss

The zircons of sample DR3-15 were sorted into three morphological groups. The first group (Figure 7-14), comprising 48 zircons, are very small rounded anhedral crystals from 28 to 132 mm with a length to width ratio from 1.0 to 3.2. The interiors are homogenous, sometimes with inclusions, and sometimes with a brighter rim (Figure 7-14 #42, #62 and #235).

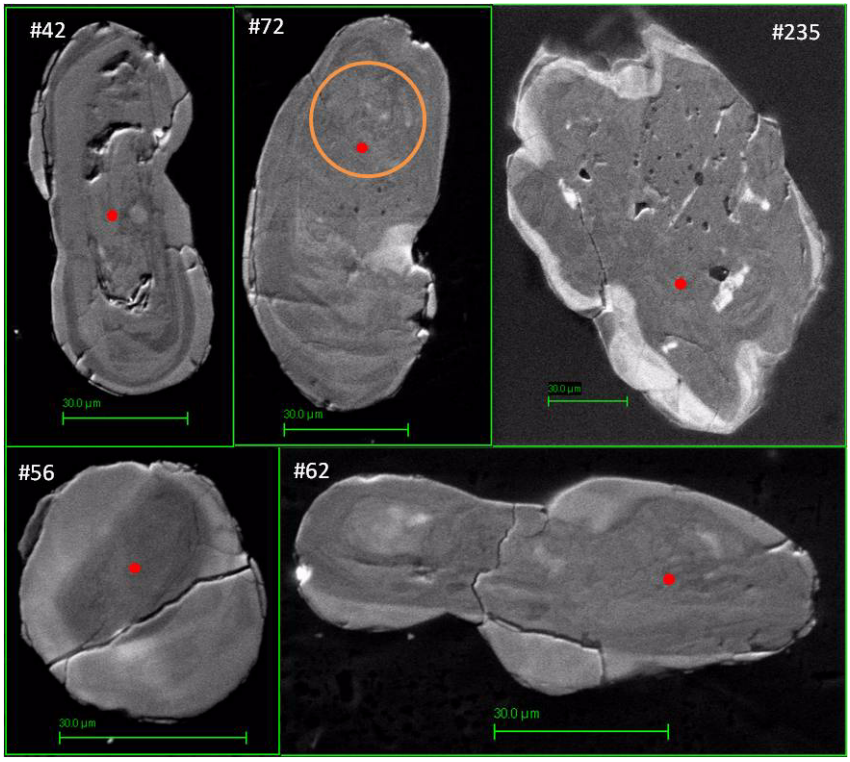

Figure 7-14: DR3-15 CL images of group 1 zircons

The second group of 75 zircons (Figure 7-15) are somewhat larger, from 45 to 150µm with a length to width ratio from 1.0 to 4.0. The crystals are anhedral to subhedral with rounded edges with a xenocrystic core displaying oscillatory zoning. These too sometimes have a lighter rim.

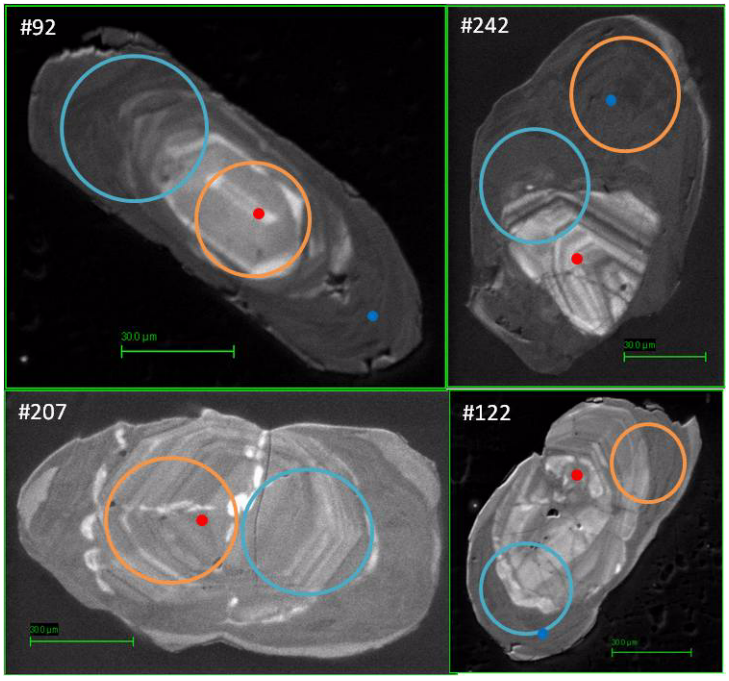

Figure 7-15: DR3-15 CL images of group 2 zircons

The third group of 63 zircons (Figure 7-16) are very similar to group 2, with a range of lengths from 33 to 195µm and the same length to width ratio and variety of shapes. The cores, however, display chaotic zoning or remnants of recrystallised metamorphic textures instead of oscillatory zoning.

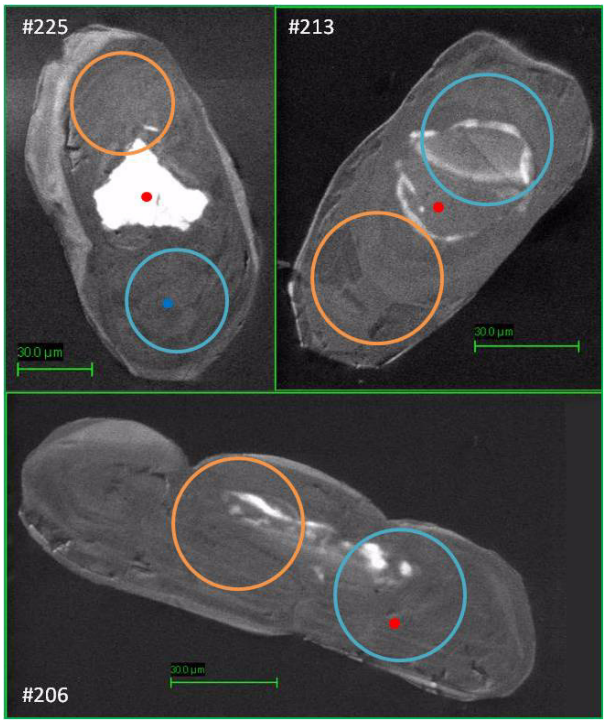

Figure 7-16: DR3-15 CL images of group 3 zircons

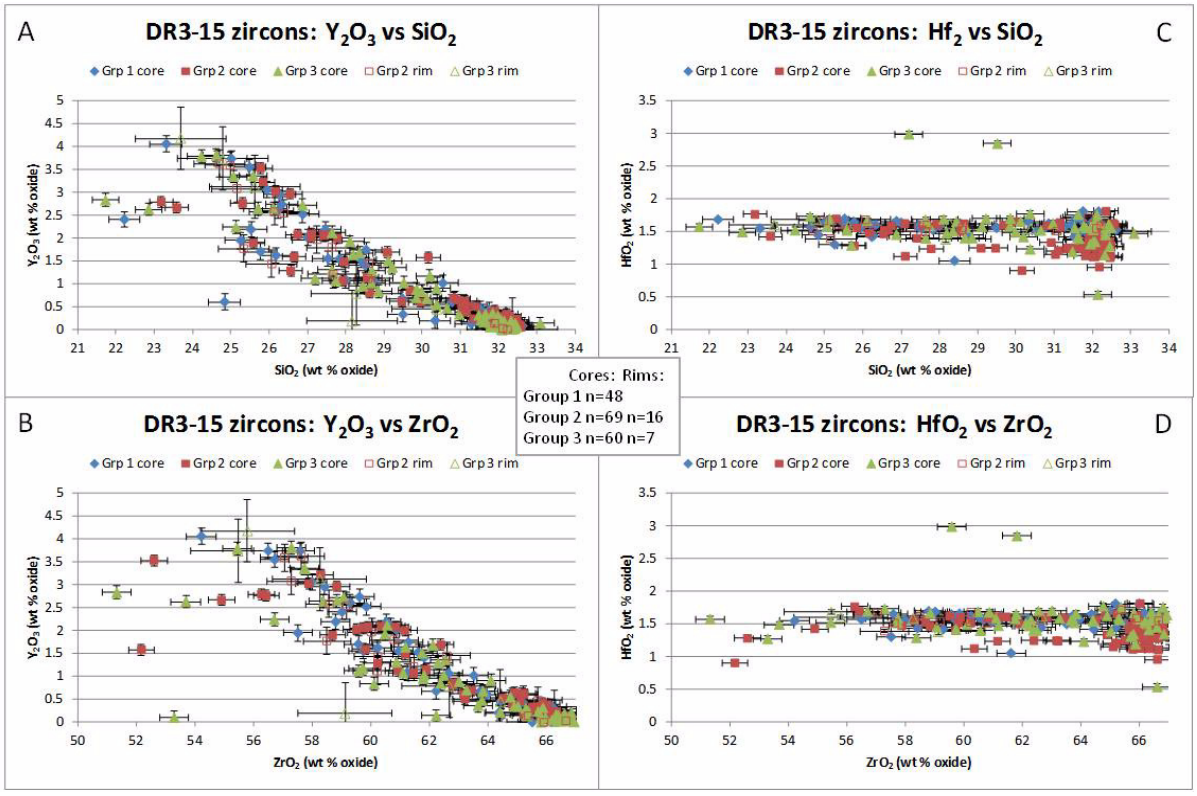

Figure 7-17: DR3-15 graphs of Y_2O_3 and HfO_2 vs. SiO_2 and ZrO_2

The graphs in Figure 7-17A and B show that for all three groups of zircons in DR3-15 there is a strong inverse relationship between Y_2O_3 and both SiO_2 and ZrO_2. This is consistent with the cores showing extensive variation in all four groups. Groups 2 and 3 show a decrease in variation in the rims.

Figure 7-17C and D indicates the concentration of HfO_2 is stable across the varying SiO_2 and ZrO_2 concentrations. Variation of HfO_2 is low across both cores and rims for all groups.

7.3 DISCUSSION

Metamorphic zircon can form over a wide range of temperature and pressure conditions, from prograde subduction, through the peak and into the retrograde exhumation, particularly during any temperature lag (Rubatto & Hermann, 2007). Recrystalisation is more common if there is no melt (sub-solidus), while the presence of melt promotes new growth (Rubatto & Hermann, 2007).

7.3.1 DR3-1: Two feldspar-quartz orthogneiss

The DR3-1 group 1 zircon cores appear to have been emplaced and a second event has subsequently caused rims to form on these cores while the group 2 zircons appear to have undergone only a single event. The group 2 zircons have a lower length:width ratio so have crystallised more slowly than the group 1 zircons, and show less evidence of complex history, though they do display sector zoning which has been attributed to a number of different factors associated with a fluctuating growth environment, the kinetic energy available and the ability of Hf and Y to diffuse through the crystal lattice (Corfu et al., 2003). The group1 zircons appear to have been modified by late and/or post magmatic recrystalisation. Corfu et al., (2003) suggest that the disrupted oscillatory zoning seen in Figure 7-1 is typical of this recrystallization effect. The Group 3 zircons are most likely metamorphic in origin.

Using Y as a proxy for the REE (Hofmann et al., 2009), the EMP data suggests that some of the group 1 zircons have an enriched core when compared with the rims, whereas the group 2 core and rim values are closely clustered. This also bears out that group 2 has a less complex history.

7.3.2 DR3-2: Quartz-feldspar-biotite orthogneiss

The bright band in the zircons in the DR3-2 groups 2 and 3 is most likely due to the same event where the zircons grew in an environment relatively depleted in REE (Hofmann et al., 2009), followed by a period of growth with subtly higher REE forming the dark rim. The cores of the group 2 zircons are all igneous in origin, displaying oscillatory zoning, albeit with some recrystallization. The cores of the group 3 zircons, however, display more complex histories with extensive metamorphic textures. The group 1 zircons do not display the bright band, so were either not impacted by the varying REE event, or have undergone extensive recrystallization. This suggests that DR3-2 has detrital zircons from an igneous source forming the group 2 xenocrystic cores, with a possibly different source for the group 3 cores, these then experienced the event forming the bright band and dark rim. The highly metamorphosed group 1 zircons were from a separate source. The zircon groups cannot be separated using the EMP data, though again the cores are more variable in REE than the rims which cluster at low levels of Y_2O_3.

7.3.3 DR3-6: Two feldspar-quartz orthogneiss

The bulk of the DR3-6 zircons (72%) are of igneous origin (groups one and two) with a metamorphic overprint, however in contrast to DR3-1 there are a significant proportion of anhedral to subhedral rounded zircons (groups 3 and 4) of metamorphic origin. The group 5 zircons may be due to fracturing of the original zircon or growth of the zircon late in crystalization in the interstitial space between other minerals (Corfu et al., 2003). The EMP data indicates that many of the group 1 zircons have a higher and more variable HfO_2 concentration. This is consistent with the zircons having a metamict core as Hf is considered to be a proxy for U as both have a similar ionic charge (Rollinson, 1993) to the Zr ion. The metamict core has a higher concentration of U which expands during cooling and decays causing damage to the crystal structure (Geisler et al., 2007). Over geological time periods this can cause the fracturing from core edge to rim seen in the group 1 zircons (Corfu et al., 2003). The subgroup of group1 zircons not displaying elevated HfO_2 may still have elevated U concentrations as many have low totals. The group 2 zircons, though similar in many characteristics to group 1 do not have the metamict core.

7.3.4 DR3-15: Garnet-sillimanite-biotite paragneiss

All of the 189 zircons from DR3-15 appear to be heavily affected by metamorphism. There is some evidence for high pressure influence on the zircons (Figure 7-14 #235) and recrystalisation and regrowth in a high grade metamorphic environment (Corfu et al., 2003). The EMP data suggests that the samples have very variable REE concentrations, reflected in Y_2O_3 concentrations from very low (at LLD) to high at 4.06 wt%. The linear relationship seen in Figure 7-17A&B supports the substitution process suggested by Speer (1982) occurring:

$$(Y,REE)^{3+} + P^{5+} = Zr^{4+} + Si^{4+}$$

However, the substitution may not be this simple as both Figure 7-17A and B appear to split into two linear relationships as the Y_2O_3 concentration increases. A number of other substitution reactions have been suggested (for a summary see Hoskin and Schaltegger, 2003), so any or all of these could also be occurring. The anomalous zircon analyses could reflect variation in the origin of the cores as the protolith for this sample is sedimentary mudstone. The increase in Y_2O_3 in the darker rims (Figure 7-16 #225 is typical) suggests the rim grew in an environment of higher REEs. The appearance of this darker rim in both group 2 and 3 and the high Y_2O_3 values for a number of the group 1 zircons suggests these all formed in the same enriched REE environment. The brighter edge on the zircons reflects a subsequent decrease in REE concentration.

All of the samples have a group of small homogenous zircons most likely of metamorphic origin. All samples also have groups of zircons with xenocrystic and/or metamict cores, surrounded by oscillatory zoned and/or metamorphic rims. This suggests that the zircons may have had different protoliths forming the cores, but have undergone similar processes to form the rims.

CHAPTER 8: U-PB DATING OF ZIRCONS

The U-Pb isotopic system is a complex system of decay reactions which includes ^{238}U decaying to ^{206}Pb and ^{235}U decaying to ^{207}Pb. In an ideal closed system the decay can be modelled to determine the age as the decay constants are known. This is the concordia (age) line on the ratio diagrams (Figure 8-2 for example). The concentrations of the isotopes in the zircons are measured, then using the ratios of the isotopes these are plotted on the concordia diagram. The concordia diagram can then be interpreted to determine the age of the event forming the zircons, and possibly the age of any lead loss events. For a full discussion of the U-Pb system see Winter (2001).

In this chapter the morphological groups determined in the previous chapter are examined in relation to the U-Pb isotope system in an attempt to determine the age of metamorphic and/or igneous zircon formation and the possible ages of any lead loss events impacting the zircons. This information is then used in later chapters to elucidate the overall history of the samples and that of Gulden Draak as a whole.

8.1 METHOD

The BSE and CL images were closely examined to find 30-40μm areas clear of inclusions or cracks of either rim or core. Some zircon groups, as specified in the results section, were not able to be dated successfully as there were no examples with a clear area large enough for dating. Many of the zircons were heavily cracked and many, particularly in DR3-15 were too small.

Age dating for each zircon was undertaken as described by Jackson et al. (2004). An Agilent 7700 ICP-MS (inductively coupled plasma mass spectrometer) with a quadrupole mass analyser and a single detector was used to measure uranium, lead and thorium isotope levels in the zircons (method L-SE-UPb). A beam from a Nd:YAG source at a wavelength of 213 nm at 5 Hz, with a fluence of approximately 3.9 Joules/cm^2 was directed at a 30 or 40 μm spot on the zircon. A 3 minute detection period was attempted for each analysis: the first 60 seconds took a gas background reading prior to starting the laser, providing a maximum of 120 seconds of ion detection for each zircon, however, many of the zircons were very small and detection times generally did not last for the full 120 seconds. This is reflected in the error on the measurement. The count data was then passed directly to GLITTER (© GEMOC & CSIRO) V4.4 software for data reduction. GJ Red zircon was used as a calibration standard for the GLITTER© software, that is 230 ppm for U and 18 ppm for Th (Elhlou et al., 2006). Zircons were analysed in runs of 10-15 samples with GJ Red zircon analyses at the beginning and end of the each run.

Mud Tank (MT) and 91500 zircon analyses were analysed as unknowns at the beginning of each run to determine external precision. Over 10 analyses of Mud Tank zircon the average was 728.4±8.8Ma, which is within error of the published value of 732 Ma (Black & Gulson, 1978). Twelve analyses of 91500 zircon yielded a concordia age of 1059.1±7.6 Ma which is also within the error margin for the published value of 1065.4±0.3 Ma (Wiedenbeck et al., 2004).

The U/Pb data was analysed using the GEMOC TerraneChron® methodology. Common lead correction was undertaken using the Excel spreadsheet ComPbCorr (Andersen, 2002).

8.2 RESULTS

Uranium/lead (U/Pb) dating results are described using age distribution graphs and concordia and probability density graphs created using Isoplot v3.71 (Ludwig, 2008). All graphs use the same colour scale for U concentration and all ellipses are based on one standard deviation. Where there is a wide range of dates for a group an inset graph of the younger zircons is included. Robust ages were difficult to achieve in some of the samples as clear areas for dating were not available. Where the sample area overlaps the core and rim this is highlighted in the text. The sites of the U-Pb analyses are highlighted in the sample CL images in the previous chapter as an orange circles.

Discordance is determined by calculation using the disparity of the $^{206}Pb/^{238}U$ and $^{207}Pb/^{235}U$ ratios. Ages for zircons with a discordance less than 15% are considered to be valid ages for a zircon forming event. Where the discordance is greater than 15% the age is less reliable, shown in the age distribution graphs as a hollow icon and used for indicative purposes only. The probability density plots use only zircons of less than 15% discordance.

As the U in the zircon decays, the Pb formed prefers to be in the Pb^{2+} ionic form which is mobile and not readily integrated into the zircon crystal lattice. These Pb ions are then prone to being lost from the zircon, in response to remelting, metamorphic events or fluid leaching (Winter, 2001). There is often a correlation between U concentrations and the discordance of the U-Pb determined age, so U concentration is often considered to be a proxy for lead loss. The U concentration in the zircon can reflect either the U concentration at the time of zircon formation or it can reflect U ions moving into the zircon from less compatible environments. Any zircons with lead loss greater than 2% were rejected to avoid anomalous results (Andersen, 2002).

8.2.1 DR3-1: Two feldspar-quartz orthogneiss

Dating of 24 zircons in group 1 and 10 in group 2 was attempted using a 40μm spot size. The group 3 zircons were all too small to date using this process. Two zircons were rejected from group 1 due to common lead being greater than 2%. The 32 remaining zircons have been plotted in Figure 8-1B. Of these 32 zircons 25 were less than 15% discordant and are included in the age probability density plot (Figure 8-1A). These figures show two main age peaks at ~500 Myr and at ~2800 Myr, with all of group 2 ages prior to ~500 Myr.

Of the 22 zircons remaining in group 1, 17 have central discordance less than 15%, with the others ranging to 60% discordance. However, all 22 zircons were included in Figure 8-2. Group 1 has clusters of concordant zircons at ~500, ~1300 and ~2800 Myr. The zircons where the dating was undertaken purely on the core (for example, zircon #231 and #209 in Figure 7-1) are those at ~2800 Myr. Where the sample area may have overlapped the rim and core (zircons #1 and #242 in Figure 7-1) the dates found were ~1300 Myr, reflecting perhaps a mixed core-rim age. The sample area of ~500 Myr age group is either purely rim area or a zircon with extensive metamorphic texture (#223 in Figure 7-1). U concentrations range from 166 to 1217 ppm, with the higher U concentrations in the younger zircons.

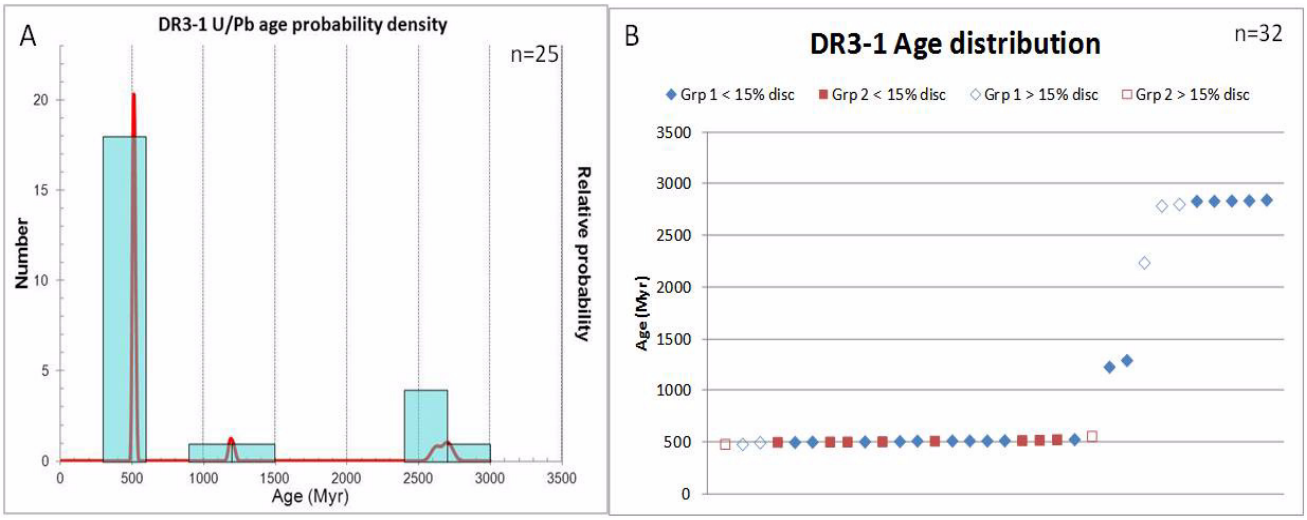

Figure 8-1: DR3-1 zircon age probability density (A) and distribution (B)

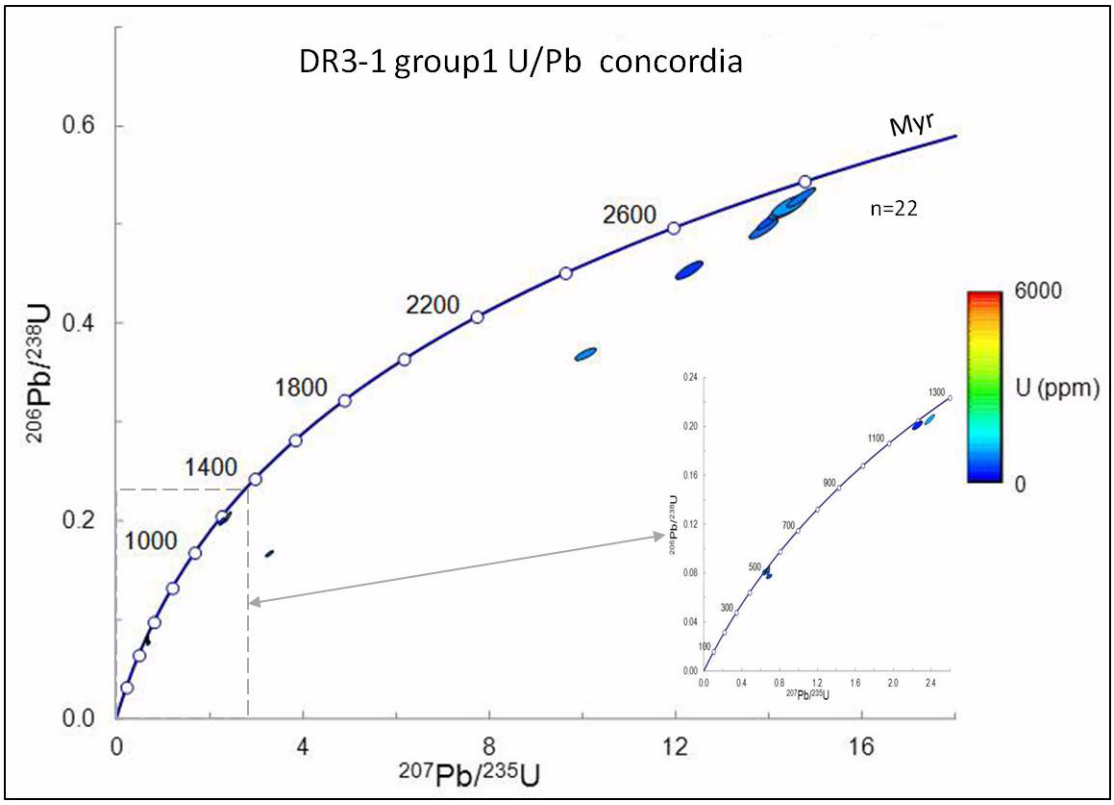

Figure 8-2: DR3-1 group 1 U/Pb concordia diagram

In contrast the 8 group 2 concordant zircons (Figure 8-3) are all clustered from 500 to 525 Myr with lower U concentrations from 290 to 602 ppm. The two zircons with discordance of 27 and 31% are pale blue as they have higher U concentrations at 746 and 942 ppm.

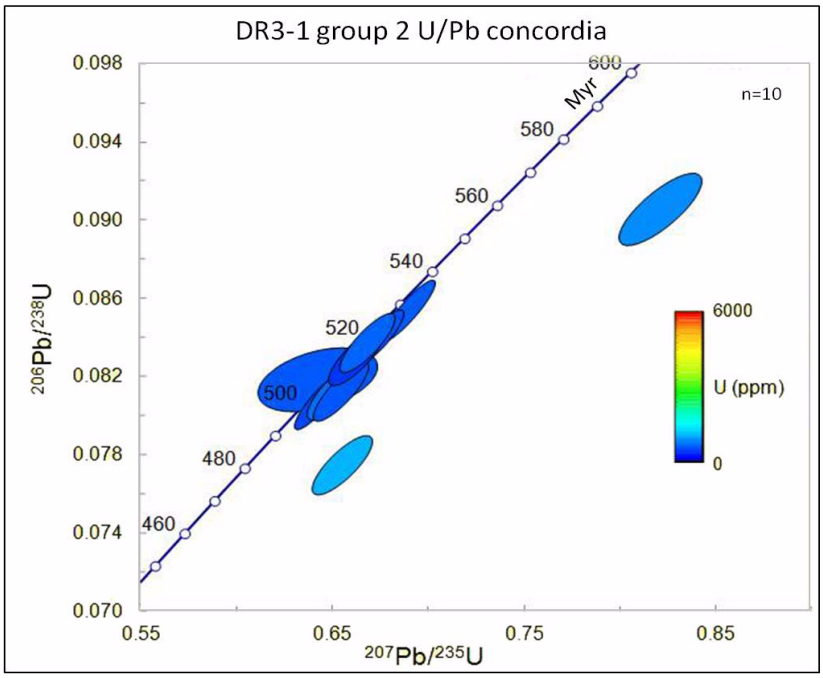

Figure 8-3: DR3-1 group 2 U/Pb concordia diagram

8.2.2 DR3-2: Quartz-feldspar-biotite orthogneiss

U/Pb dating using a 40µm spot size was attempted on 29 zircons. Four group 2 and one group 3 zircons were rejected as they had greater than 2% common lead, leaving 24 zircons. Of these only 8 (two in groups 1 and 3, four in group 2) have discordance less than 15%. These have been used for the probability density plot in Figure 8-4A and have been highlighted in Figure 8-4B as solid icons, with their zircon numbers.

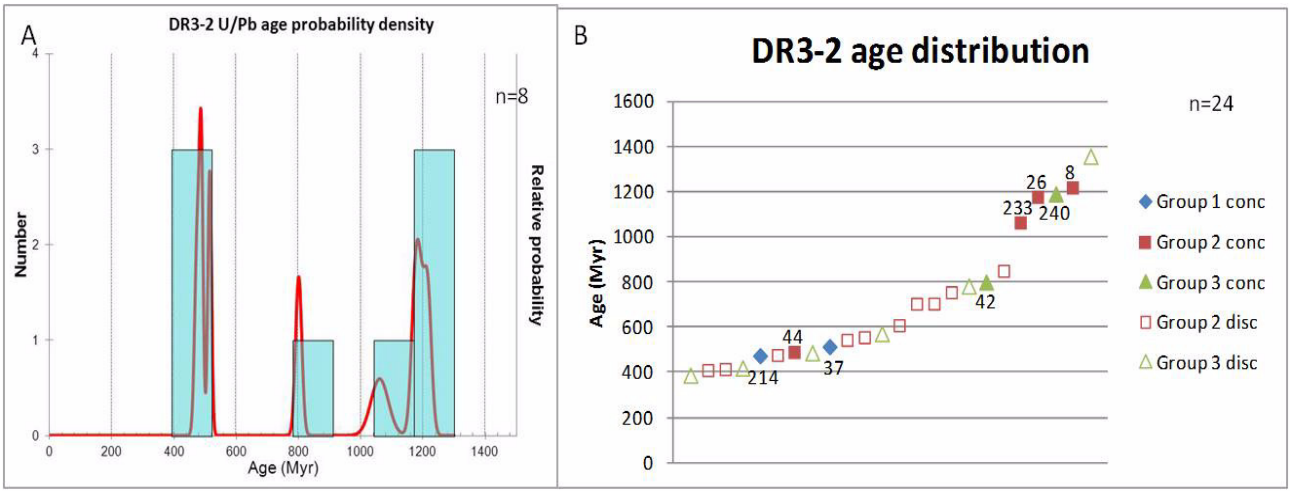

Figure 8-4: DR3-2 zircon age probability density (A) and distribution (B)

In the first morphological group only two zircons were dated as the others were too small. These two zircons (Figures 8-4B & 7-5 #214 and #37) have lead loss less than 2% and discordance of 3% and 7%, so the ages determined, at 474±8 Myr and 514±6 Myr are considered valid. These form the peak at ~500Myr in Figure 8-4A.

The second group has four zircons with discordance less than 15% with the other ten ranging to 76% discordant. Zircons #8 (CL image in Figure 7-6) and #26 have ages taken from their cores and contribute to the peak at ~1200Myr in Figure 8-4A. The age for zircon #233 (CL image in Figure 7-6) has been taken from a mixed domain and has created the peak at ~1080 Myr in Figure 8-4A. Zircon #44 (CL image in Figure 7-6) is also a mixed domain and has contributed to the peak at ~500Myr. Figure 8-5 shows there is a general trend towards increased U concentrations as the ages of the zircons decrease, though there is a small cluster of zircons with better discordance and lower U concentration at ~500 Myr.

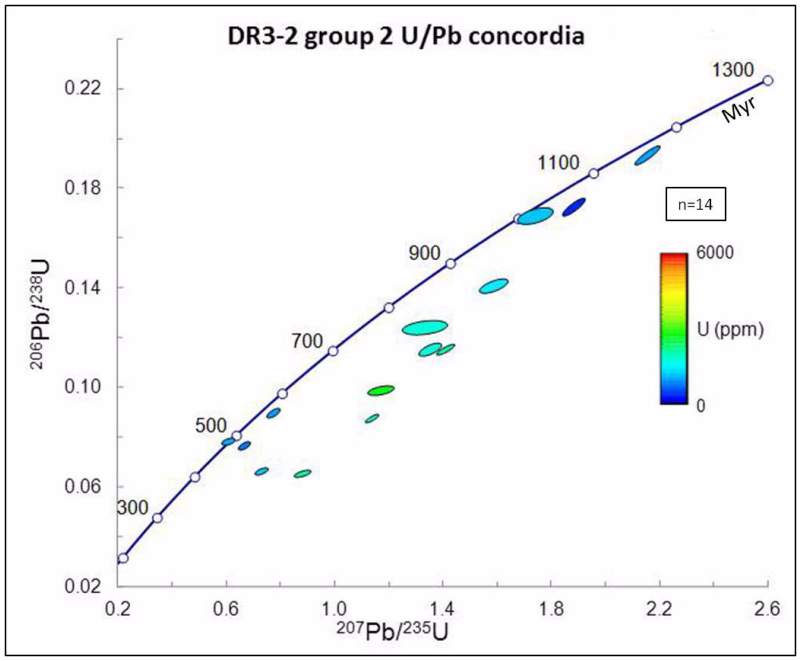

Figure 8-5: DR3-2 group 2 U/Pb concordia diagram

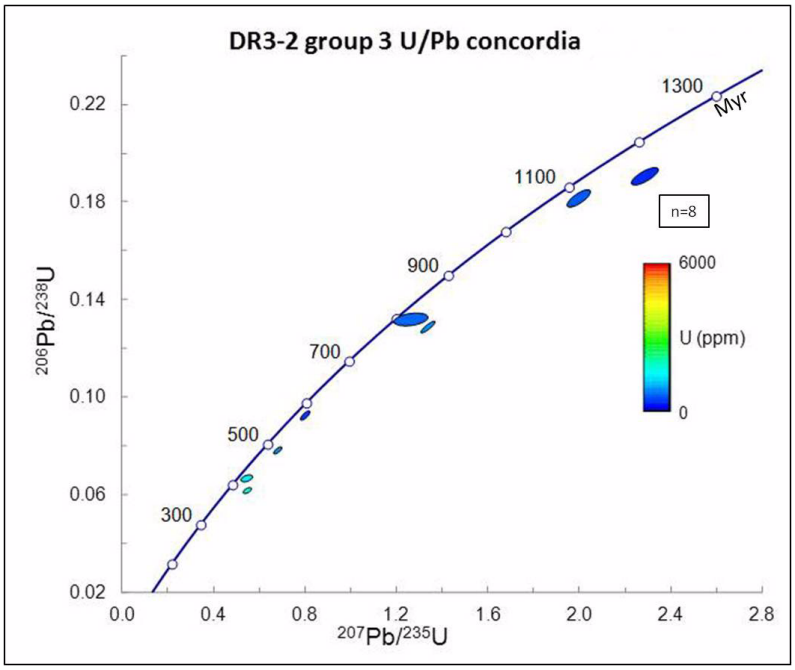

Figure 8-6: DR3-2 group 3 U/Pb concordia diagram

The third group of 8 zircons has two (Figure 8-4B # 240 and #42, CL images in Figure 7-7) with less than 15% discordance, with the other 6 ranging to 65% discordance. The age of #240 is taken from the core and contributes to the age peak at ~1200 Myr (Figure 8-4A) while #42, which creates the peak at ~800 Myr, has been taken from mixed core and rim domains. Similarly to group 2, Figure 8-6 indicates that as the zircon age decreases the U concentration increases.

8.2.3 DR3-6: Two feldspar-quartz orthogneiss

Of the four samples DR3-6 has the best zircons for dating, as they are larger, but even these are heavily fractured so great care selecting the area for dating was taken. The results are 45 zircons were dated, none were rejected due to common lead above 2% and 39 of these have discordance less than 15%. Figure 8-7A shows there is a single large peak of zircons spanning ~1200 to ~1300 Ma, with the peak at ~1240 Ma. Figure 8-7B shows that the morphological groups for this sample all have similar ages.

Morphological group 1 and 2 were considered similar, but separated by the metamict core seen in the group 1 zircons. Fifteen group 1 ages including 4 core rim pairs and 21 group 2, including 3 core-rim pairs were successfully dated. The core-rim pairs for group 1 (Figure 8-8A), show that the metamict cores are all much younger (up to 468 Myr younger for #58; CL image in Figure 7-9) than the rims and have much higher concentrations of U (up to 5696 ppm for #72 core). All but one (#74) of the group 2 cores (Figure 8-8B) are younger than the rims, though the difference in ages between the core and rim is much less marked at only up to 57 Myr. This is also highlighted in Figures 8-9A and 8-9B which plot all the core and rim data, not just the pairs, for groups 1 and 2.

The cores younger than the rims have been affected by lead loss or some other impact to the U-Pb system as they would necessarily be older than the rims as they would have formed first. Disregarding these younger cores, the group 1 and 2 zircons all contribute to the peak from 1200 to 1300 Myr.

Of the group 3 zircons only 7 were successfully dated with one having discordance over 15%. Figure 8-10 shows the concordia for all seven zircons. Figure 8-7B shows 5 of the zircons are associated with the main age peak at ~1240 Myr. The zircon, at ~975 Myr has oscillatory zoning which has been strongly recrystallised, which may have reset the U-Pb system. Figure 8-10 indicates the discordant zircon has a much higher U concentration at 2008 ppm.

Only two zircons (#107 and #108; CL images in Figure 7-11) were successfully aged in group 4. These are both less than 6% discordant with ages at 1269±13 Myrs, in the main peak (Figure 8-7) and 1336±11 Myrs at the high end of the main peak.

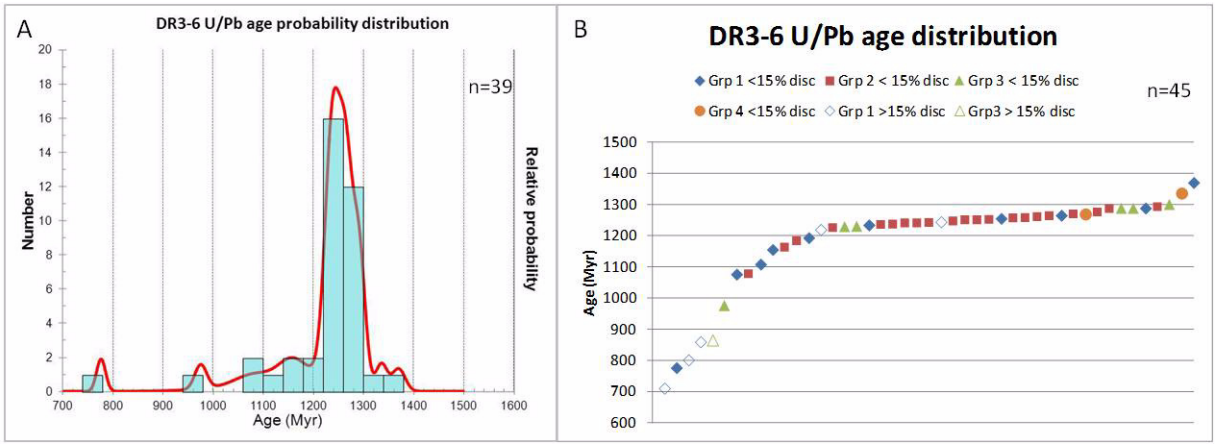

Figure 8-7: DR3-6 zircon age probability density (A) and distribution (B)

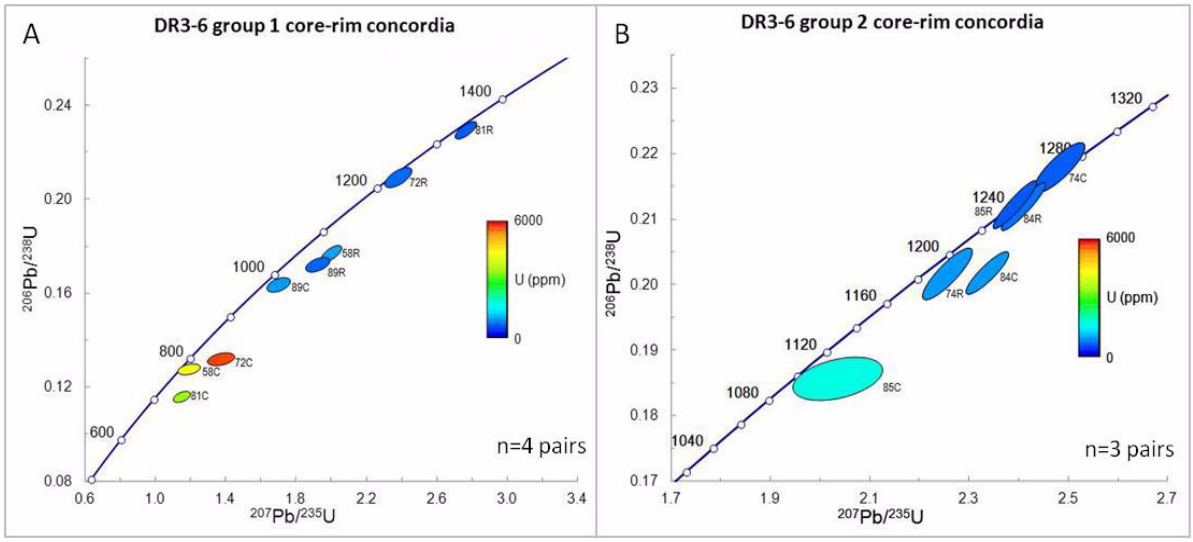

Figure 8-8: DR3-6 groups 1 (A) and 2 (B) core and rim pair concordia

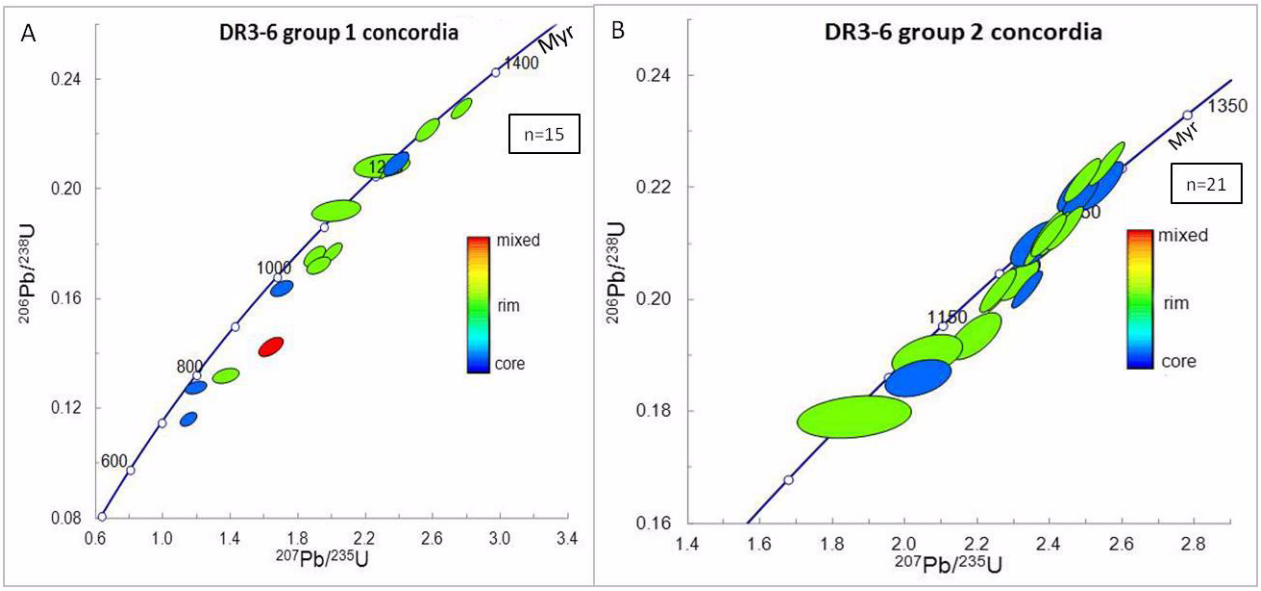

Figure 8-9: DR3-6 groups 1 (A) and 2 (B) concordia showing all cores and rims

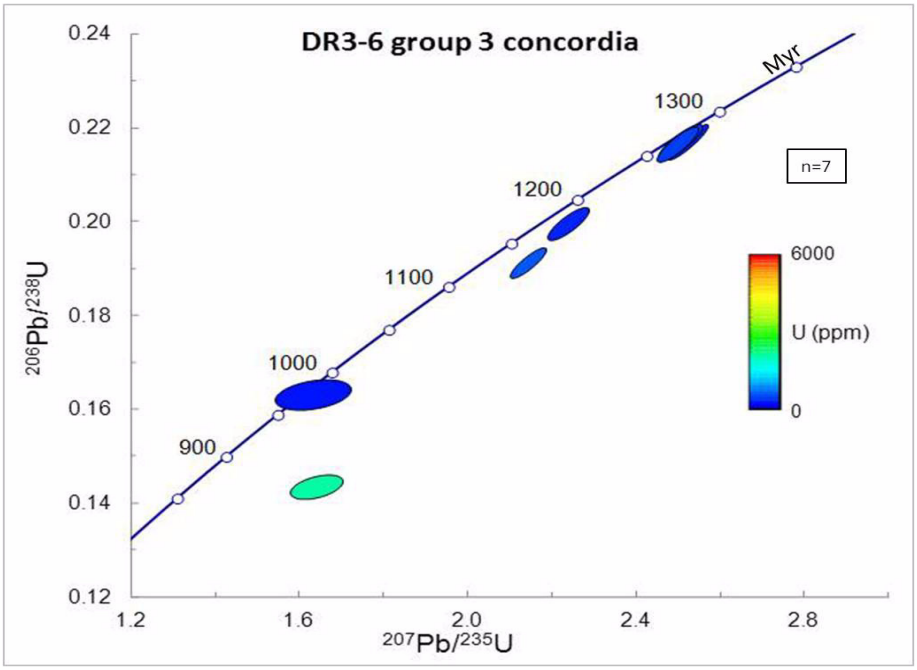

Figure 8-10: DR3-6 group 3 U/Pb concordia

8.2.4 DR3-15: Garnet-sillimanite-biotite paragneiss

The U-Pb analysis of DR3-15 has only had limited success as the zircons are very small and heavily fractured. A 30µm spot size was used which has provided less robust ages. Figure 8-11A is based on only those zircons less than 15% discordant and Figure 8-11B includes all discordant zircons, but not those rejected for high common lead levels.

In morphological group 1, of 8 zircons large enough to sample 6 were rejected with common Pb greater than 2% leaving the remaining 2, both of which have discordance greater than 95%. No reliable age can be taken from these analyses.

In group 2, 17 of 24 zircons sampled were rejected with common lead levels too high, and only one (#92) has discordance less than 15% (at 12.4%), with the other 6 zircons ranging from 35% to 88% discordant. Zircon #92 has a $^{207}Pb/^{206}Pb$ age of 3108±30 Myr.

Group 3 is similar to the previous groups with 15 of 20 zircons rejected for high common lead levels with only three (#79 at 2.3%, #78 at 11.5% and #213 at 10.6%) less than 15% discordant. The other two are 44.1% and 98.4% discordant. The age of zircon #213 age (at ~522 Myr) was taken on the rim, while the others, at ~2537Ma and ~2782 Ma were taken on the core.

The morphological groups are not reflected in the U/Pb age data, but all of the group 1 (homogenous zircons) are in the younger range from 500 Myr (Figure 8-12).

The concordia for all three groups show that. similarly to the other samples, U concentration increases as the zircons become younger (Figure 8-13).

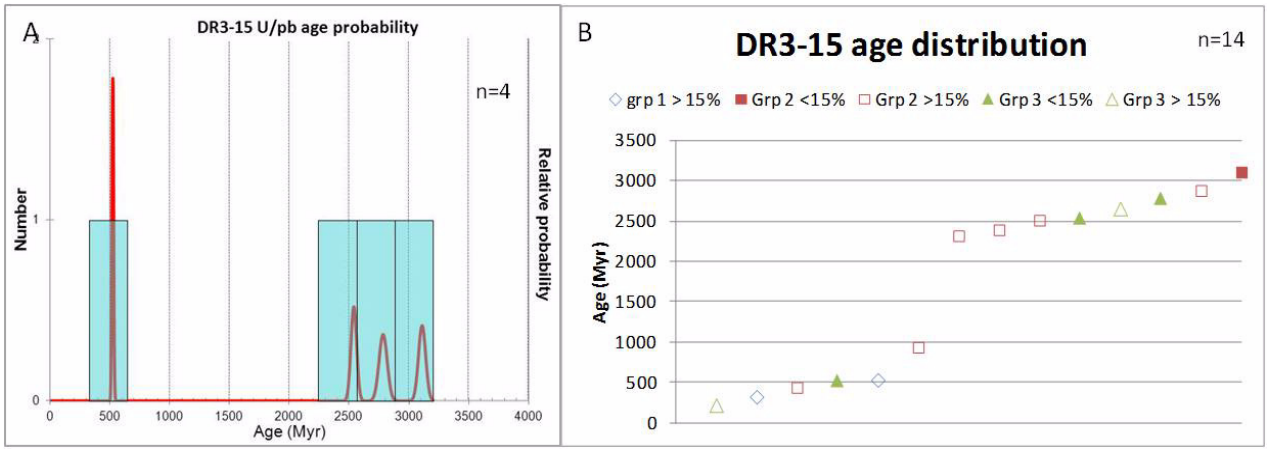

Figure 8-11: DR3-15 zircon age probability density (A) and distribution (B)

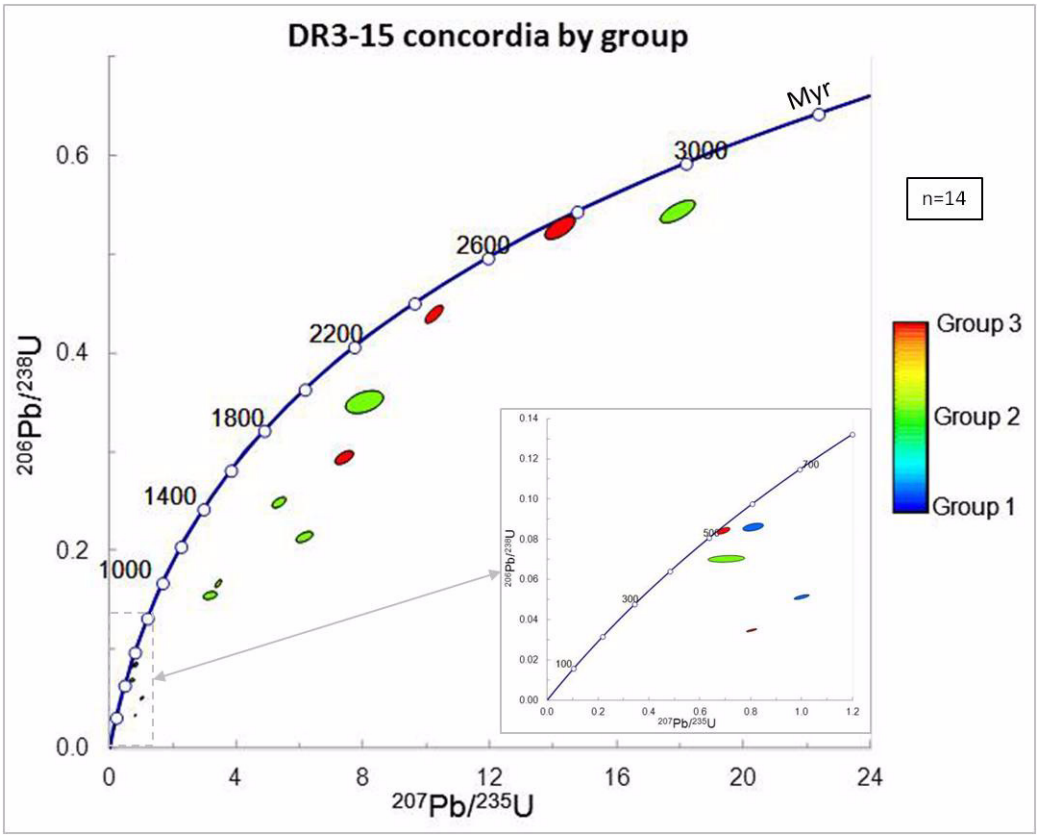

Figure 8-12: DR3-15 concordia displaying morphological groups

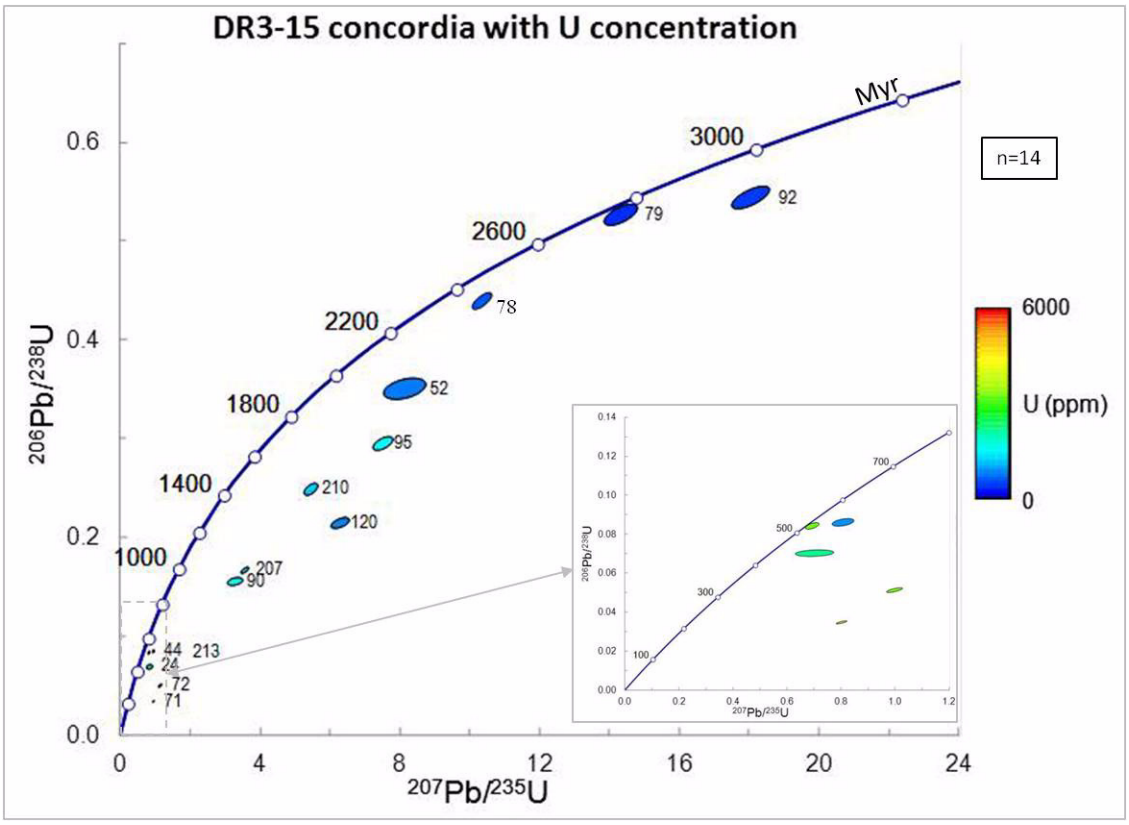

Figure 8-13: DR3-15 concordia displaying U concentrations

8.3 DISCUSSION

A spread of U/Pb concordant ages suggests the U-Pb isotopic system has been reset. This is likely to be either by Pb loss due to an orogenic event which would promote recrystallization and/or metamictization or a complex interplay of Pb loss, inherited zircon and new zircon growth (Halpin et al., 2012). Halpin et al. (2012) suggest the age of an igneous intrusion or metamorphic event can be determined by considering only concordant (<2% discordance) zircons with Lu-Hf systematics and Th, U, Y and REE concentrations typical of the population. The oldest of these zircons represents the likely earliest age for the igneous or metamorphic event. This process has been followed where possible for the samples in this study.

8.3.1 DR3-1: Two feldspar-quartz orthogneiss

Only two zircons from each of groups 1 and 2 gave a U-Pb age with <2% discordance. In group 1 zircon #9 was the oldest with an age of 527±5 Myr while zircon #221 in group 2 gave 519±6 Myr. Due to the small sample size of very robust ages the dates for this sample are considered indicative rather than definitive. This U/Pb data suggests the group 1 zircons have undergone two events with the cores forming in the ~2800 Ma emplacement event. These zircons then formed the site for further crystallization of zircon forming their rims due to a metamorphic event causing partial remelting prior to ~500Ma. This second event also caused the formation of the group 2 zircons. Figure 8-14 shows that the discordant zircons align on a chord from ~500 Ma to ~2856 Ma which suggests an emplacement age of ~2856 Ma and lead loss caused by an ~500 Ma metamorphic event.

The two zircons (#1 and #242) at ~1300 Ma may indicate an additional metamorphic event which has caused a minor partial melt in the rock.

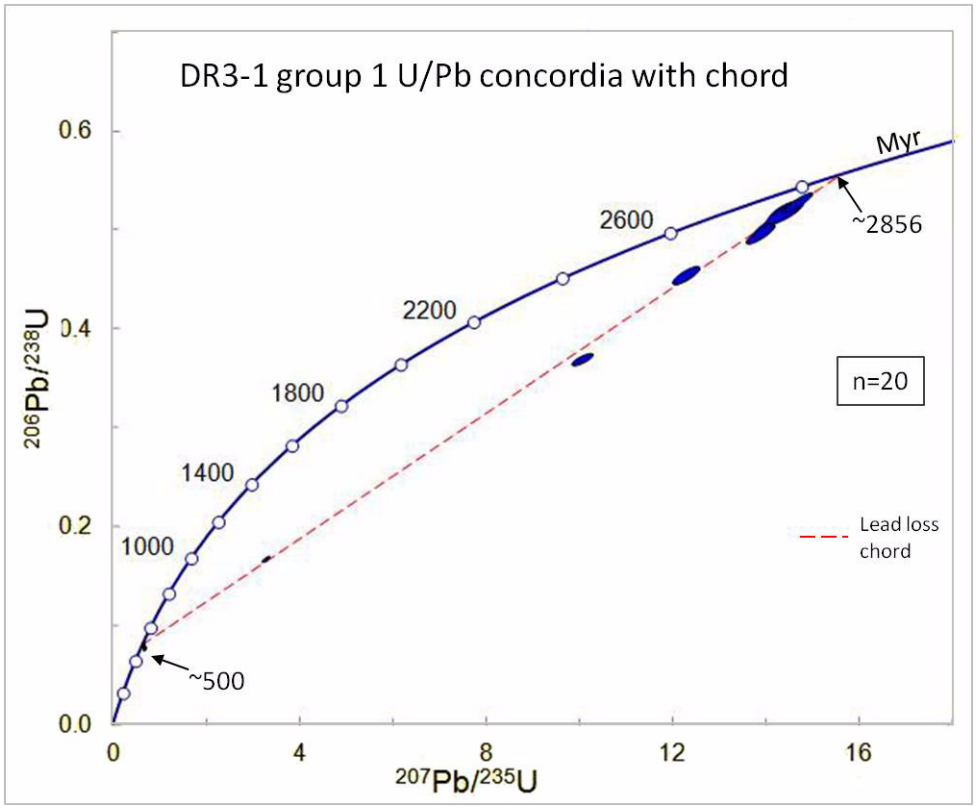

Figure 8-14: DR3-1 group 1 U/Pb concordia with lead loss chord to 500 Myr

8.3.2 DR3-2: Quartz-feldspar-biotite gneiss

In sample DR3-2 there were no zircons with ages less than 2% discordant. Eliminating the ages where mixed core and rim domains were used highlights that there are only two indicative ages for zircon growth, at ~1200 Myr for the original igneous zircon growth in the cores of groups 2 and 3 and at ~500 Myr, for group 1 and the rims of groups 2 and 3. This suggests an emplacement age prior to ~1200 Myr and a metamorphic/partial remelting event at ~500 Myr. The group 1 zircons are anhedral to subhedral, suggesting a metamorphic origin, while the rims of group 2 and 3 may be igneous. The lead loss for the zircons is very complex with a combination of lead loss events likely. Chords have been included in Figure 8-15 for lead loss at ~136 Ma and ~500 Ma. This indicates an initial formation date at ~1290Ma. However, these don't account for all of the discordant zircons, so a third chord was added at ~1370 Ma, though there are still a number of zircons outside the chord. These probably represent older detrital cores as they are all group 2 zircons which display an igneous core with clear oscillatory zoning (Figure 7-6).

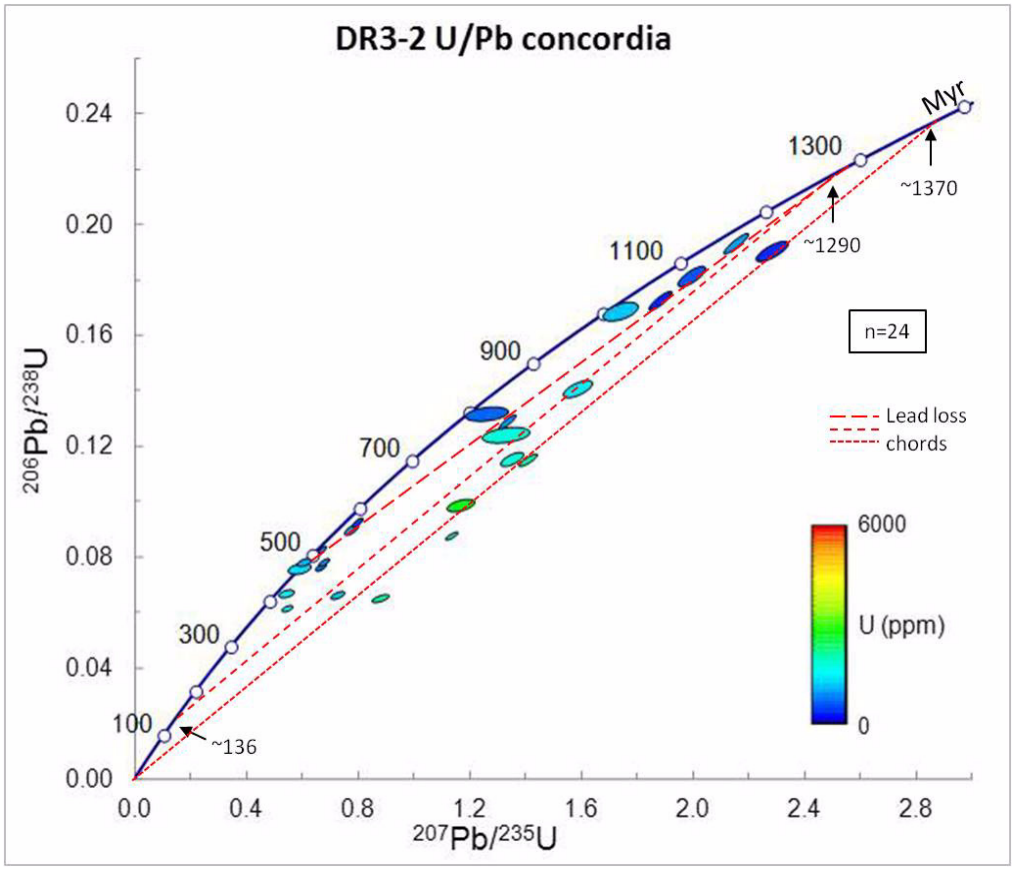

Figure 8-15: DR3-2 U/Pb concordia with lead loss chord to 136 Myr

8.3.3 DR3-6: Two feldspar-quartz orthogneiss

In sample DR3-6 there were 2 zircons in group 1, 7 in group 2 and 1 in group 3 that have robust ages less than 2% discordant. The oldest of these in each group respectively are #73 with an age of 1288±17 Myr, #41 at 1286±13 Myr and #7 at 1287±12 Myr. These are remarkably similar ages suggesting the igneous event occurred at or prior to 1287 Ma (after Halpin et al., 2012). The presence of older, though more discordant zircons suggests that the igneous event could be even earlier. For example, the rim of zircon #81 has an age of 1370 Ma with 3.14% discordance. The lead loss chords fitted in Figure 8-16 are consistent with an emplacement age of ~1370 Ma, with the lead loss being caused by an event at ~500Ma or at ~136 Ma, or a combination of them both.

U (ppm) concentration is generally higher in the cores than the rims, particularly in the group 1 zircons which have metamict cores. The cores and rims are thought to have formed in the same event, with the differences in ages the result of U and Pb ion migration.

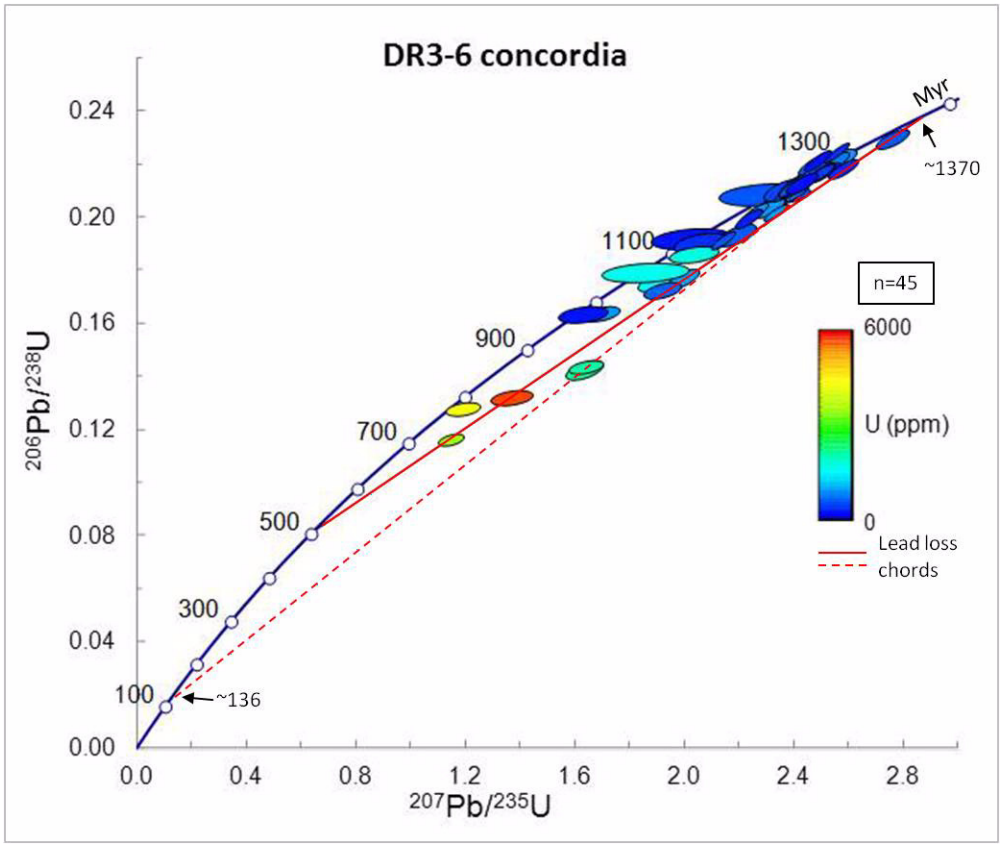

Figure 8-16: DR3-6 U/Pb concordia with lead loss chords 1370 Ma to 500 Ma and 136 Ma

8.3.4 DR3-15: Garnet-sillimanite-biotite paragneiss

The U/Pb age data for all three groups of zircons in DR3-15 have been heavily impacted by Pb loss. There are no zircons meeting the criteria to determine the initial age of the event forming the zircons, though # 79 at 2.31% discordant it close. It is the second oldest zircon from this sample at 2782±34 Myr. The wide range of discordant ages, and the concentration of three relatively concordant ages taken on cores in the 2500 to 3100 Myr suggests that DR3-15 has Archaean zircons which have undergone a series of events impacting the U/Pb isotope systematics. This range in relatively concordant ages suggests a sedimentary protolith with a variety of detrital zircons of different ages.

Group 1 zircons have no core visible in CL and are both at or younger than 500 Myr. This suggests they formed during a ~500 Ma event, but as there are three zircons across all the groups with ages from 221 to 429 Ma, a later lead loss event, possibly at ~136 Ma is likely. Figure 8-17 shows all of the samples, with two suggestions for possible lead loss chords, though realistically, these are only two of a myriad of possibilities.

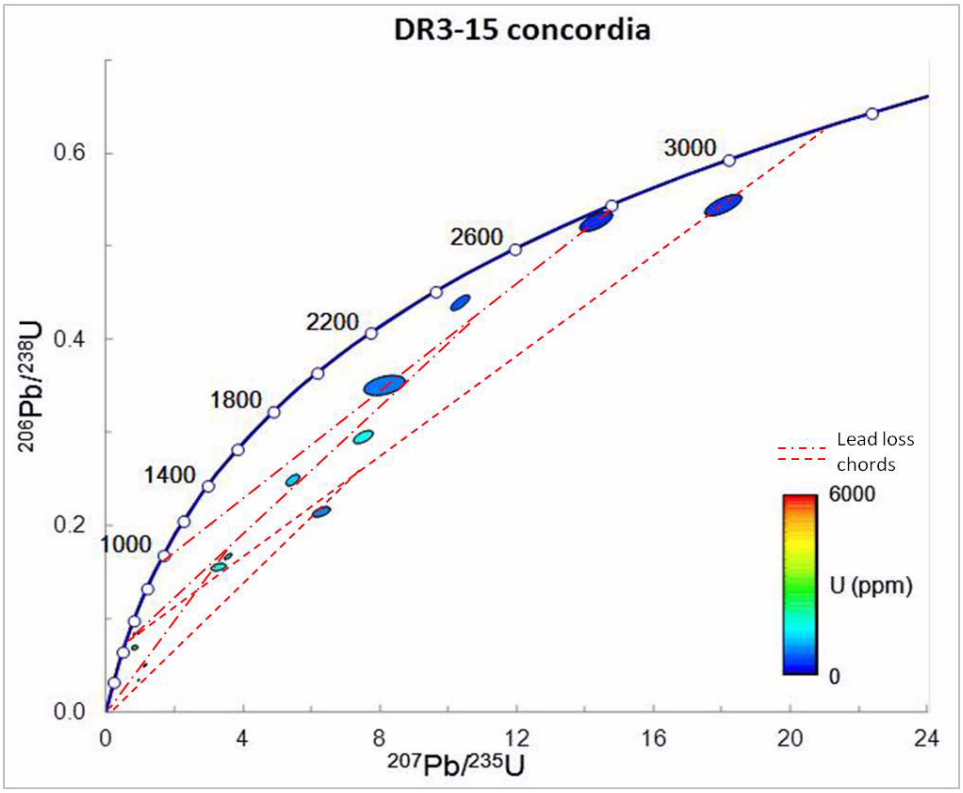

Figure 8-17: DR3-15 U/Pb concordia with possible complex lead loss chords

CHAPTER 9: HAFNIUM ISOTOPES

A second isotopic system, that of Lu-Hf isotope decay, was used to investigate the source of the zircons. The beta decay of ^{176}Lu to ^{176}Hf has a half life of around 37 billion years (Scherer, 2001). When magma is formed, Hf partitions into the melt while Lu remains in the solid phase. As the zircons grow the Hf is incorporated into the zircon crystal lattice as it has a similar ionic charge and radius to the Zr ions (Rollinson, 1993). By measuring the Lu and Hf isotopes, the ratio of $^{176}Hf/^{177}Hf$ when the zircon was initially crystalised ($^{176}Hf/^{177}Hf_i$) can be determined. By comparing this with a model of $^{176}Hf/^{177}Hf$ decay in bulk silicate earth, that is, uniform chondritic reservoir (CHUR) and depleted mantle (DM) an indication of the source of the melt that created the zircons is possible. For a more detailed review of the system see Scherer (2007).

In this chapter the events highlighted from the U-Pb analysis are further investigated to determine the source of the melt forming the zircons, and to further confirm the history of the samples. This information will be used in the next chapter to summarize what we know of the samples.

9.1 METHOD

Hafnium analysis was undertaken on those grains large enough to allow a 40μm spot with the most concordant ages. A Nu Plasma high definition LA-MC-ICPMS (laser ablation multi-collector ICPMS) at the GEMOC facility at Macquarie University was used for the analyses. A Nd:YAG crystal was used to generate an electron beam current of 5 Hz, with a fluence of approximately 7.45 Joules/cm^2. A 200 second detection period was attempted for each analysis: the first 30 seconds took a gas background reading prior to starting the laser, providing 170 seconds of ion detection for each zircon. Many of the zircons are very small so some detection times were quite short. This is generally reflected in the error on the measurement. The detectors were set up per Table 9-1 to allow corrections for the isobaric overlap of ^{176}Hf by ^{176}Y and ^{176}Lu.

Detector	Mass #	Isotopes
H1	177	^{177}Hf
H2	178	^{178}Hf
H3	179	^{179}Hf
H4	180	^{180}Hf
H5	182	^{182}W
Axial	176	^{176}Hf ^{176}Y ^{176}Lu
L1	175	^{175}Lu
L2	174	^{174}Hf ^{174}Yb
L3	172	^{172}Lu

Table 9-1: LA-ICPMS-MC detector setup

Mud tank and temora standards were used as reference materials. Runs of approximately 12 unknowns were bracketed by Mud Tank samples, with Temora samples included every 20 to 25 unknown samples. The average $^{176}Hf/^{177}Hf$ ratio over the 30 Mud Tank analyses

undertaken was 0.282509 ± 0.000132 which is within error of the published value of 0.282523 ± 0.000043 (Griffin et al., 2006). For Temora, the average over 8 analyses was 0.282675 ± 0.000059 which also is within error of the published value of 0.282686 ± 0.000008 (Woodhead & Jergt, 2007).

9.2 RESULTS

The initial $^{176}Hf/^{177}Hf$ ($^{176}Hf/^{177}Hf_i$) ratios were calculated using the measured $^{176}Hf/^{177}Hf$ and $^{176}Lu/^{177}Hf$ ratios, an ^{176}Lu decay constant of 1.865×10^{-11} (Scherer et al., 2001) and the $^{207}Pb/^{206}Pb$ age where the age is greater than 1Ga or the $^{206}Pb/^{238}U$ age where the ages is less than 1Ga. This initial ratio was used in conjunction with the initial ratio for CHUR at that age to determine the ε_{Hf} value using the following equation:

$$\varepsilon Hf = \frac{\left(\frac{^{176}Hf}{^{177}Hf}\right)_{zircon} - CHUR_{Ti}}{CHUR_{Ti}}$$

A T_{DM} model age was calculated for the initial age of the sample assuming it has evolved from depleted mantle. This used values of 0.28325 for $^{176}Hf/^{177}Hf$ and 0.0384 for $^{176}Lu/^{177}Hf$, which represent current values (that is at age 0). Where relevant, a model $T_{DM}^{crustal}$ was also calculated based on a magma source similar to average continental crust which has an evolving $^{176}Hf/^{177}Hf$ ratio of 0.015.

The graphs for the Hf data all include a line depicting the evolution of the initial Hf ratios for DM and CHUR from 3500 Ma to present day. Where the ages are less reliable (shown as open icons in the graphs), the Hf ratios are valid data, but care should be taken interpreting where this is in the horizontal axis of the graphs. The x and y-axis scales on the initial graphs have been kept constant for comparison purposes.

Vertical arrays of zircons at similar ages on the $^{176}Hf/^{177}Hf_i$ graphs indicate variation due to mixing of two components in the magma. Horizontal arrays of zircons at similar $^{176}Hf/^{177}Hf_i$ ratios suggests the same source with variation in the U/Pb age caused by lead loss (Halpin, 2012). That is, there was one crystalisation event with variable amounts of lead loss.

Negative εHf values represent an event with generally continental crust magma by reworking existing continental crust or a mixed magma of continental crust and DM. Conversely, positive εHf values indicate a DM magma (Griffin et al., 2004).

Zircon analysis sites are included as blue circles in CL images of the zircons in Chapter 7.

9.2.1 DR3-1: Two feldspar-quartz orthogneiss

Hf isotope analysis was attempted on 26 zircons where the U/Pb date has been determined (Chapter 8). Figure 9-1 shows the samples form two groups with 2 anomalous samples (#242 and #1). The signals achieved for zircon #242 were very short, though the ratios for both zircons are believed to be valid. The mean T_{DM} for the sample is 2.515±0.296 Ga, while the mean $T_{DM}^{crustal}$ is 3.353±0.402 Ma. Zircon #242 was omitted from this mean, as if it is a valid analysis, it has a much younger source, with a T_{DM} of ~1490 Ma.

Positive εHf values (Figure 9-1B) for the older aged zircons indicates those have a predominantly DM source, while negative εHf values for the younger zircons suggests those are reworked continental crust. The vertical arrays indicate more than a single source was mixed in the magma.

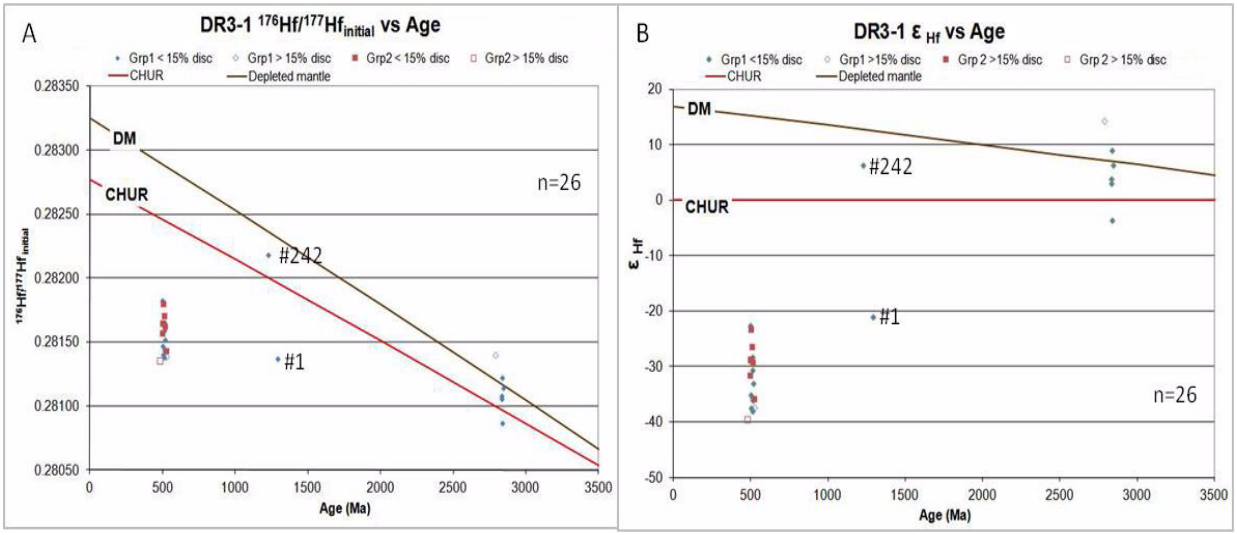

Figure 9-1: DR3-1 hafnium vs. age graphs

9.2.2 DR3-2: Quartz-feldspar-biotite orthogneiss

Hafnium isotope data was obtained on 17 zircons that were previously dated. This sample has only 8 relatively concordant ages. Figure 9-2A shows all the samples with the exception of zircon #241 have a similar $^{176}Hf/^{177}Hf_i$ ratio. Omitting #241, the mean of the group is 0.282127 with sd of 0.000101, with a mean T_{DM} of 1.565±0.142 Ga and a mean $T_{DM}^{crustal}$ of 1.967±0.312 Ga. Zircon #241 has a much lower initial Hf ratio, so gives a much older T_{DM} of 2.44Ga and a $T_{DM}^{crustal}$ of 3.53Ga. The predominance of positive ε_{Hf} values (Figure 9-2B) for the older zircons suggest these are from a depleted mantle source magma. In the previous chapter zircons #233 and #42 were both found to be a mix of core and rim, so the age given is unreliable.

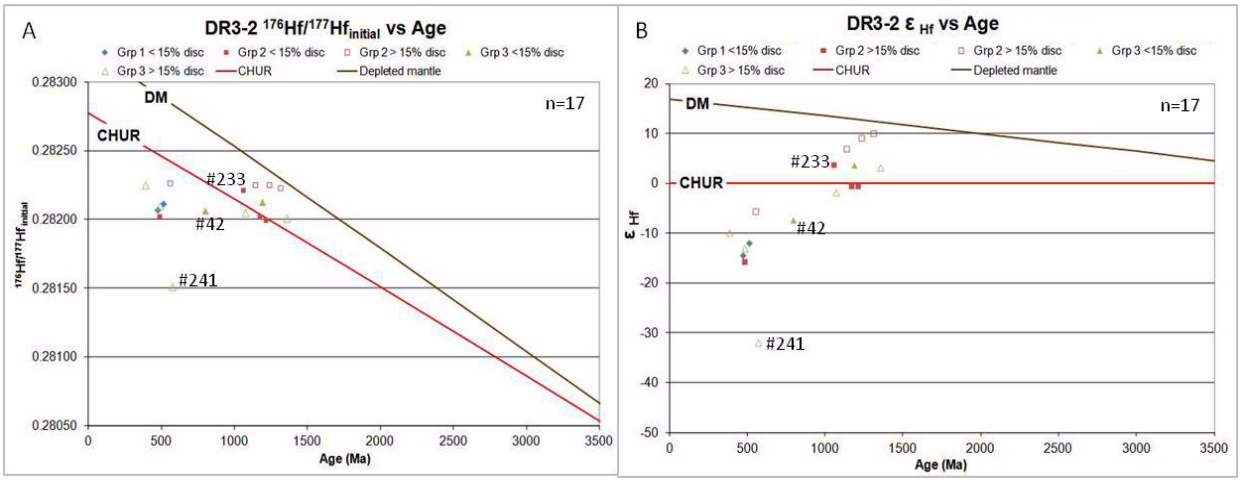

Figure 9-2: DR3-2 hafnium vs. age graphs

9.2.3 DR3-6: Two feldspar-quartz orthogneiss

Of the 45 samples that were U/Pb dated in the last chapter, 36 samples, with one core-rim pair were analysed for Hf isotopes. These all have very similar $^{76}Hf/^{177}Hf_i$ ratios with a mean of 0.282065 with sd of 0.000050. The core-rim pair also have very similar ratios within one sd of the mean. The predominance of positive ε_{Hf} values (Figure 9-3B) for the population suggests the zircons are from a DM source magma, with mean T_{DM} of 1.640±0.070 Ga and $T_{DM}^{crustal}$ of 1.902 ±0.131 Ga.

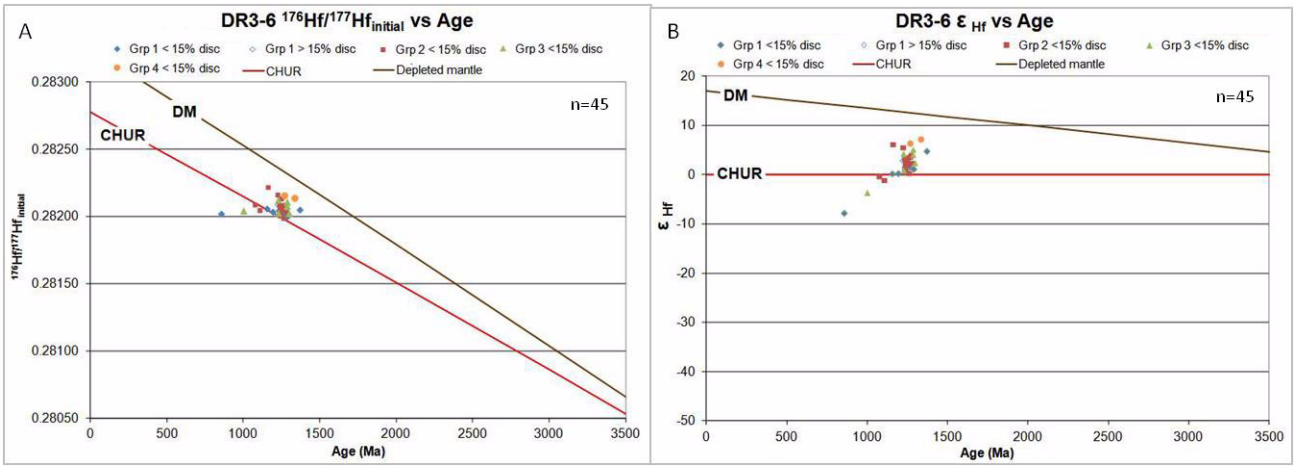

Figure 9-3: DR3-6 hafnium vs. age graphs

9.2.4 DR3-15: Garnet-sillimanite-biotite paragneiss

In the previous chapter, DR3-15 had only 4 zircons that gave ages with discordance less than 15%. Of these only three were successfully analysed for Lu-Hf isotopes. Two populations were found in the age data, and these are still visible in the Hf data (Figure 9-4) though the size of the population is very small overall, at 7 samples, with only 1 sample (#213) in the younger ~500 Myr population. The small dataset and unreliability of the age data means any conclusions from the data is necessarily general. All except zircon #92 have negative ε_{Hf} values (Figure 9-4B) suggesting the zircons are from a continental crust source magma. The $^{76}Hf/^{177}Hf_i$ ratios are also very similar, with a mean of 0.281276 and standard deviation of 0.000264. The mean T_{DM} is 2.7236±0.3276 Ga while the mean $T_{DM}^{crustal}$ is 3.2128±0.3577 Ga.

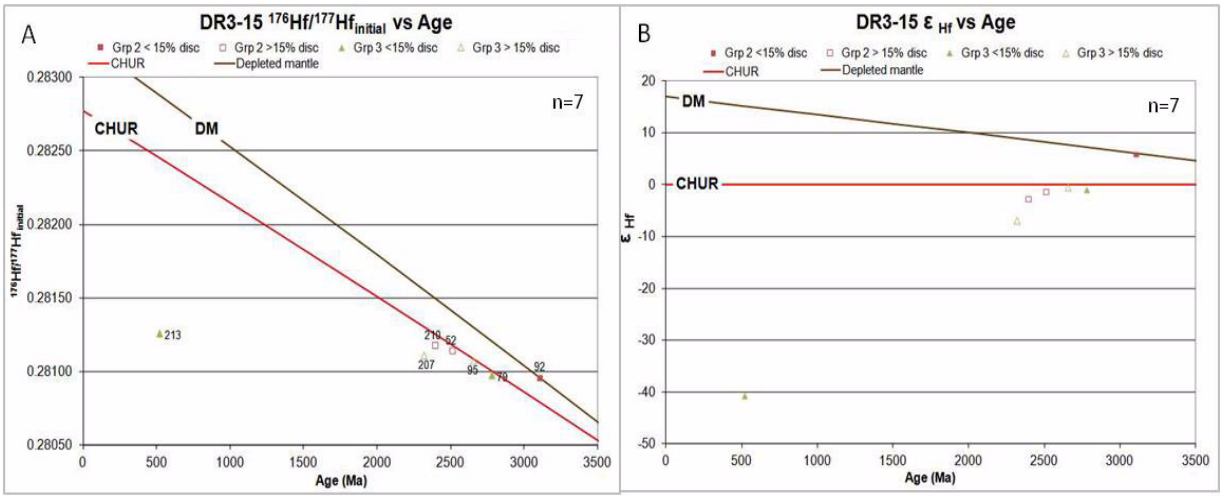

Figure 9-4: DR3-15 hafnium vs. age graphs

9.3 DISCUSSION

In DR3-1 the group 1 cores were formed during an igneous event with magma from DM with some continental crust input and an emplacement age of at least 2800 Ma. Zircons #1 and #242 may indicate some impact of a partial remelting event at ~1290 Ma, with the anomalous Hf values for #242 due to a localised phase change removing Hf (for example garnet growth). The bulk of the zircons were impacted around 500 Ma when the original rocks were subject to a second event which partially melted and reset the isotope systematics of the older zircons and formed the younger zircons and rims.

Sample DR3-2 has two distinct populations, one with ages of ~500 Myr and the other of ~1200 Myr. The similarity of $^{176}Hf/^{177}Hf_i$ for both populations, as seen in Figure 9-5, suggests the same source with variation in the U/Pb age caused by lead loss (Halpin, 2012). That is, there was one crystalisation event, little recrystalisation and variable amounts of lead loss. Due to the unreliable age data on most of the zircons, these have been re-plotted to align with the oldest reliable age for the sample at 1215 Ma. The low $^{176}Hf/^{177}Hf_i$ for zircon #241 (Figure 9-2) is possibly due to a localised phase change releasing Hf (for example, garnet breakdown). The DR3-2 zircons have formed during an igneous event prior to 1215 Ma, from a DM source with some continental crust input.

In the previous chapter DR3-6 was found to have a single population with robust ages (<2% discordant) to 1287±12Ma. Figure 9-6 shows that this is a minimum age for the sample. The zircons have been replotted with the rim age of zircon #81, that is 1370 Ma, and 1500 Ma as examples of the range of ages possible for the DR3-6 zircon population. The upper limit for the age is 1630 Ma where the mean $^{176}Hf/^{177}Hf_i$ crosses the depleted mantle model line. So, the DR3-6 zircons were formed in an igneous event prior to 1287 Ma from a source magma that contained both DM and continental crust.

The similarity of $^{176}Hf/^{177}Hf_i$ and ages for DR3-2 and DR3-6 suggests that these samples could have been formed during the same tectonic event. The anomalous DR3-1 zircons (#1 and #242) could also have formed at this time.

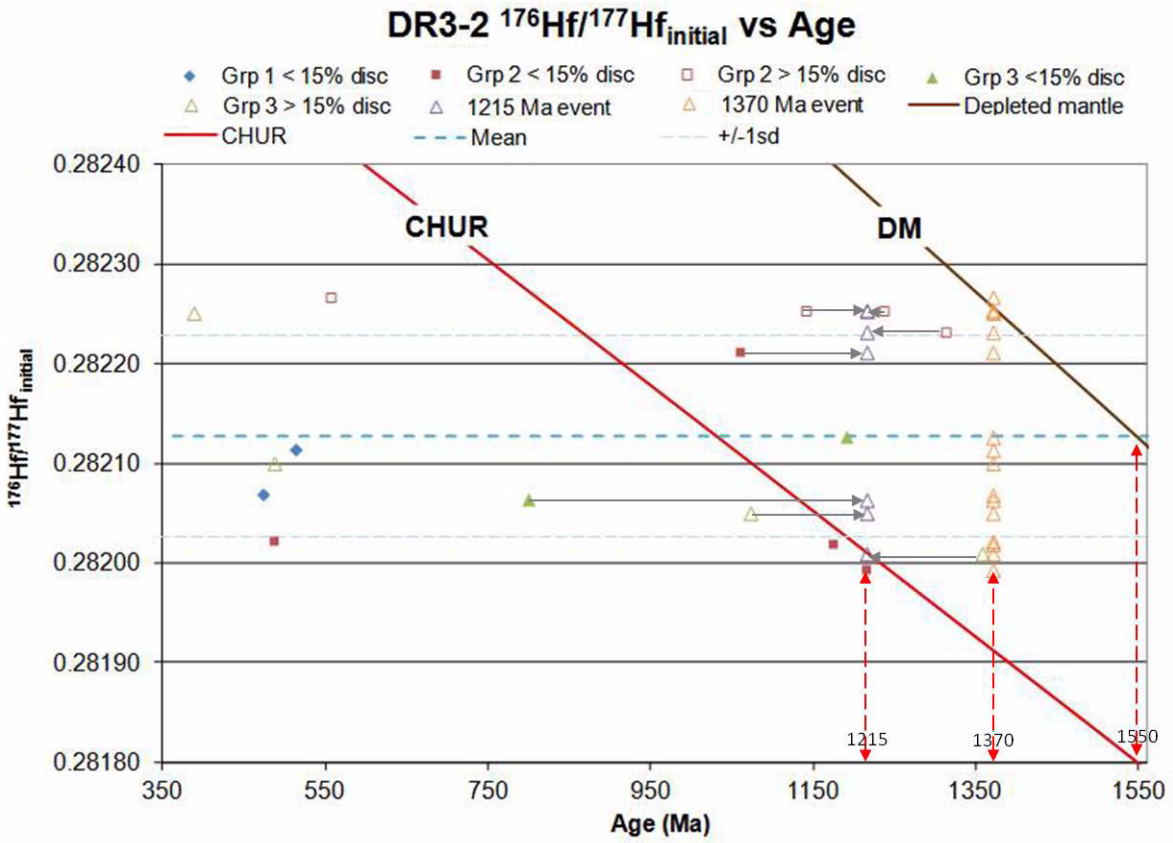

Figure 9-5: DR3-2 hafnium ratio vs. age with mean and possible formation ages

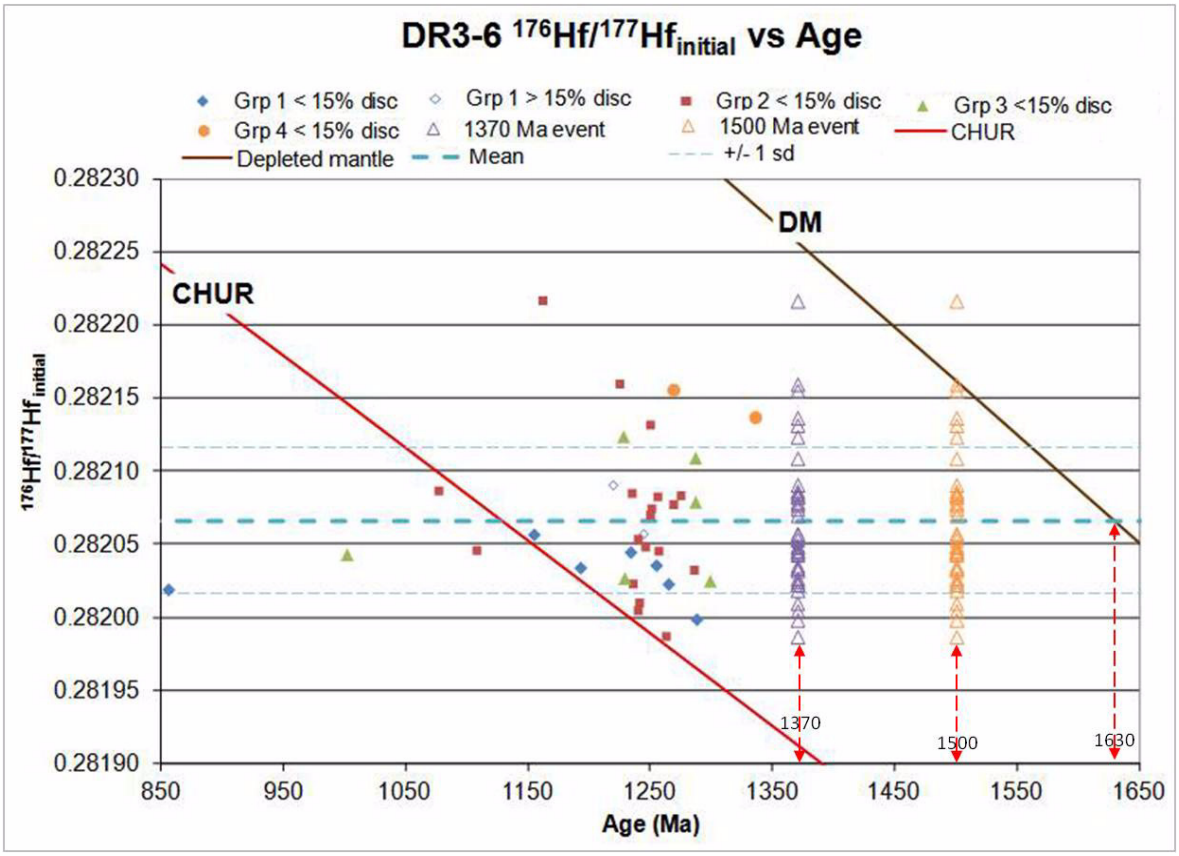

Figure 9-6: DR3-6 hafnium ratio vs. age with mean and possible formation ages

In the previous chapter the most robust zircon age in sample DR3-15 was found to be #79 at 2782 Myr with discordance of 2.3%. As the ages for those zircons with discordance greater than 15% (#52, #95, #207 and #210) is very unreliable, these zircons were replotted using the 2782 Ma age (Figure 9-7). This suggests that they may be the same population as #79, and have formed from depleted magma mixed with continental crust. The mean $^{176}Hf/^{177}Hf_i$ of the older population is 0.281074 with a standard deviation of 0.000091. Zircon #92, could be from this population or an older separate population. It may be detrital in origin.

Zircon #213 (CL image in Figure 7-16) with a U/Pb age of ~522 Ma has a marginally higher $^{176}Hf/^{177}Hf_i$ value than the 2782 Ma population. The age has been taken on the rim of the zircon which has very faint impressions of oscillatory zoning and appears to have a metamorphic edge. This suggests that there were three growth periods: the first when the core was formed, the second when the rim grew (this could be a similar age to the first growth period), and the third when the edge grew as part of a 522 Ma metamorphic event which has caused lead loss and reset the U-Pb system.

The sediments which formed DR3-15 are older than 522 Ma, but may not be as old as the early zircon population at 2782 Ma.These are most likely detrital, though from possibly a single or small number of sources as there is not great variation within the sampled zircons.

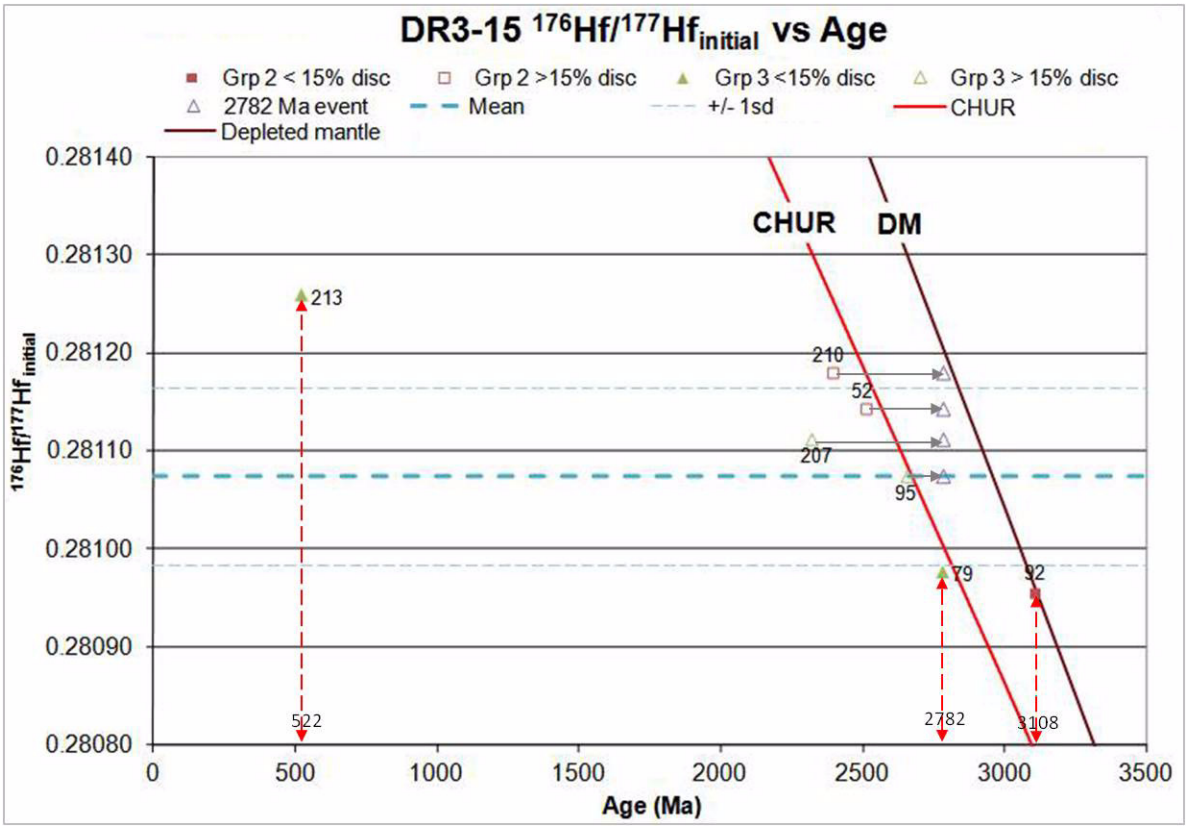

Figure 9-7: DR3-15 hafnium ratio vs. age with mean and possible formation ages

CHAPTER 10: CONCLUSIONS

The information from the previous chapters has been consolidated into a geochronology (summarised in Table 10-1) which has then been correlated with major tectonic events occurring in the region. The Gulden Draak sample geochronology most closely matches that of the Nornalup Complex in the Albany-Fraser Orogen, which suggests the Albany-Fraser Orogen is much more extensive than originally conceived.

Age		Event	Sample affected	Correlation
Archaen	~2800 Ma	Igneous emplacement of radiogenic magma	DR3-1	Yilgarn or Mawson craton
		Detrital zircons formed	DR3-15	
Archaen to Mesoproterozoic	~2800 to ~1200 Ma	Sedimentation of metapelite protolith	DR3-15	Albany-Fraser Orogen Malcolm Gneiss?
Mesoproterozoic	~1290 Ma	Igneous emplacement of radiogenic magma	DR3-6	Early Albany-Fraser Orogen Stage 1
		Granulite facies metamorphism	DR3-1; DR-6; DR3-15; DR3-16	
	~1200 to ~1290 Ma	Igneous emplacement of radiogenic magma	DR3-2	Late Albany-Fraser Orogen Stage 1 or Stage 2
		Amphibolite facies metamorphism	DR3-2	
Cambrian	~500 Ma	High temperature metamorphism with partial re-melting of zircon and resetting of isotope systematics	DR3-1; DR3-2; DR3-6; DR3-15	Kuunga Orogen
Cretaceous	~136 Ma	Greater India starts to rift off Gondwana	DR3-2; DR3-6; DR3-15; metamorphic dome complex profile	Gondwana breakup
	~108 Ma	Ridge jump -> Gulden Draak left on Australian plate	?	

Table 10-1: Summary of DR3 sample geochronology

The radiogenic granite protolith of DR3-1 was emplaced in either the Yilgarn or Mawson craton during the Archaean, sometime prior to ~2800 Ma in an unknown orogenic event. The sedimentary protolith for DR3-15 must have been deposited prior to the granulite facies event, so has occurred sometime between when the zircons were formed, prior to ~2800 Ma and the granulite metamorphism prior to the emplacement of DR3-2 as that sample saw only amphibolite facies metamorphism.

During the Mesoproterozoic, in the first stage of the Albany-Fraser Orogen (~1290 Ma), perhaps shortly after the initial collision of the Yilgarn and Mawson cratons, the radiogenic tonalite protolith for DR3-6 was emplaced. It is likely that granulite facies metamorphism occurred in conjunction with this initial collision. The radiogenic granite protolith of DR3-2 was emplaced later in the first stage or subsequently during the second stage of the Albany-Fraser Orogen (~1200 Ma). The minor element analysis for the sample suggests it may be syn-collisional. Metamorphism to amphibolite facies occurred sometime after the DR3-2 emplacement.

All samples were impacted by the Kuunga Orogen which occurred during the Cambrian, prior to ~500 Ma. Lead loss and partial remelting of the zircons occurred, resetting the isotope systematics in all samples to variable extents. Samples DR3-2, DR3-6 and DR3-15 all show possible lead loss due to the breakup of Gondwana in the Cretaceous, at ~136 Ma.

The suggested position of Gulden Draak at 200 Ma by Gibbons et al., (2012, Figure 6a) (reproduced in Figure 10-1) is to the west of the Darling Fault which suggests the knoll should be in the Pinjarra Orogen. However, no solid evidence for Pinjarra Orogen ages, 1080 Ma to 900 Ma were found, though is one concordant DR3-6 group 3 zircon age at ~975 Ma (#16). Gulden Draak could have been in an area of low stress during the active period of the orogen thereby having little impact on the isotope systematics.

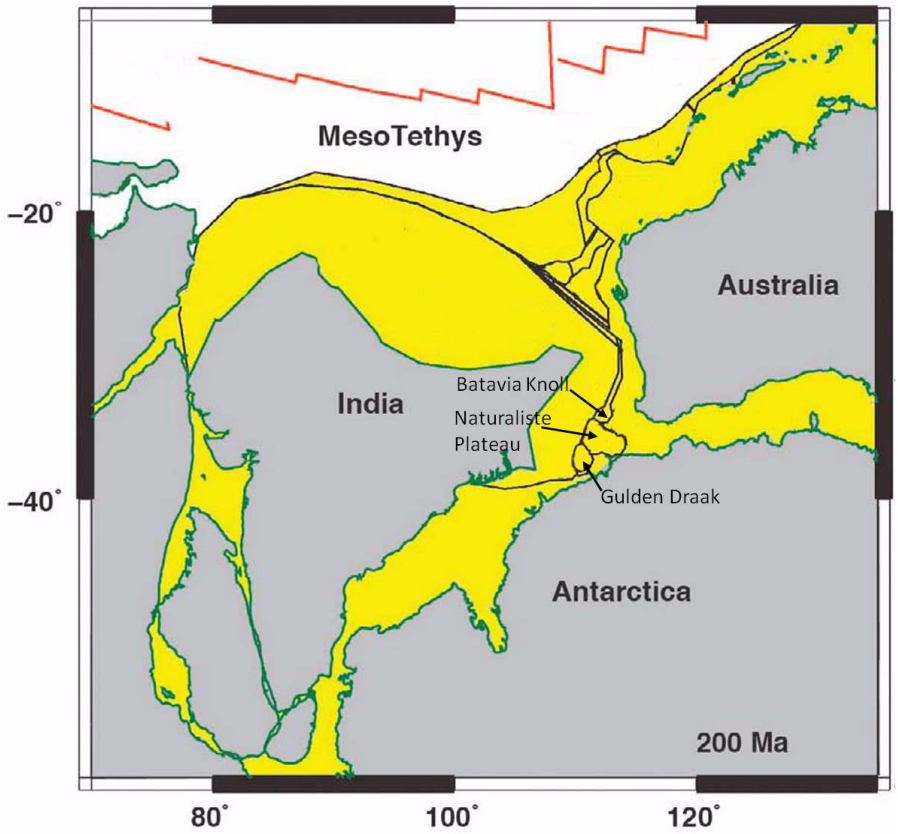

Figure 10-1: Gondwana prior to breakup ~200 Ma showing location of Gulden Draak (from Gibbons et al., 2012 Figure 6a).

Both DR3-1 and DR3-6 have rounded shapes (Chapter 4) and have most likely formed in situ in a cobble beach while the margin was being tectonically uplifted. The profile of the knoll (Figure 3-2) suggests it is a metamorphic dome complex which formed during the rifting event lifting and thinning the ductile continental basement rocks via listric faults (Daczko, 2012). Further investigation of this aspect needs to be undertaken.

This research has provided additional evidence to inform the debate over the nature and position of the triple point where Australia, Antarctica and Greater India were connected during the period of the Gondwana supercontinent and its subsequent breakup. It also emphasises the complexity of supercontinent amalgamation and the orogenic zones formed and the difficulty in specifying definitive ages for events in a metamorphic terrane.

BIBLIOGRAPHY

Andersen T 2002 Correction of common lead in U-Pb analyses that do not report ^{204}Pb *Chemical Geology 192:* 59-79.

Barrat J A Zanda B Moynier F Bollinger C Liorzou C and Bayon G 2012 Geochemistry of CI chondrites: major and trace elements and Cu and Zn isotopes *Geochimica et Cosmochimica Acta 83:*79-92.

Black L P and Gulson B L 1978 The age of the Mud Tank carbonatite, Strangeways Range, Northern Territory *BMR Journal of Australian Geology and Geophysics 3:*227-232.

Blatt H and Tracy R J 1996 Petrology: igneous, sedimentary and metamorphic. 2nd Ed. W.H Freeman, 529 pp.

Boger S D 2011 Antarctica- before and after Gondwana *Gondwana Research 19:*335-371.

Bucher K and Frey M 2002 Petrogenesis of Metamorphic Rocks. 7th Ed. Springer-Verlag, Berlin, 341 pp.

Carlson W D 2002 Presidential address: Scales of disequilibrium and rates of equilibration during metamorphism *American Mineralogist 87:* 185-204.

Chappell B W and White A J R 2001 Two contrasting granite types: 25 years later *Australian Journal of Earth Sciences 48:* 489-499.

Chatterjee N Mazumdar A C Bhattacharya A and Saikia R R 2007 Mesoproterozoic granulites of the Shillong-Meghalaya Plateau: evidence of westward continuation of the Prydz Bay Pan-African suture into Northeastern India *Precambrian Research 152:* 1-26.

Clark D J Hensen B J and Kinny P D 2000 Geochronological constraints for a two-stage history of the Albany-Fraser Orogen, Western Australia *Precambrian Research 102:* 155-183.

Corfu F Hanchar J M Hoskin P W O Kinny P 2003 Atlas of zircon textures *Reviews in Mineralogy and Geochemistry 51(1):*469-500.

Daczko N 2012 personal communication 6Jun2012.

Deer W A Howie R A and Zussman J 1966 *An introduction to the rock forming minerals* Longman Group (FE) Ltd., Harlow England.

Dobmeier C J and Raith M M 2003 Crustal architecture and evolution of the Eastern Ghats Belt and adjacent regions of India *Geological Society, London, Special Publications 206:* 145-168.

Duebendorfer E M 2002 Regional correlation of Mesoproterozoic structures and deformational event sin the Albany-Fraser orogen, Western Australia *Precambrian Research 116:* 129-154.

Elhlou S Belousova E Griffin W L Pearson N J and O'Reilly S Y 2006 Trace element and isotopic composition of GJ-red zircon standard by laser ablation *Goldschmidt Conference Abstracts:* A158.

Ernst W G and Liu J 1998 Experimental phase-equilibrium study of Al- and Ti-contents of calcic amphibole in MORB - a semiquantitative thermobarometer *American Mineralogist 83:*952-969.

Fitzsimons I C W 2003 Proterozoic basement provinces of southern and southwestern Australia and their correlation with Antarctica from Yoshida M Windley B F and Dasgupta S (eds) *Proterozoic East Gondwana: supercontinent assembly and breakup Geological Society, London, Special Publications 206:* 93-130.

Geisler T Schaltegger U and Tomaschek F 2007 Re-equilibration of zircon in aqueous fluids and melts *Elements 3:*43-50.

Gibbons A D Barckhausen U van den Bogaard P Hoernle K Werner R Whittaker J M and Muller D 2012 Constraining the Jurassic extent of Greater India: Tectonic evolution of the West Australian margin *Geochemistry Geophysics Geosystems 13(5):*1-25.

Google Earth 2012 *Google* http://earth.google.com (15 March 2012).

Griffin W L Belousova E A Shee S R Pearson N J and O'Reilly S Y O 2004 Archaean crustal evolution in the northern Yilgarn Craton: U-Pb and Hf-isotope evidence from detrital zircons *Precambrian Research 131:* 231-282.

Griffin W L Pearson N J Belousova E A and Saeed A 2006 Comment: Hf-isotope heterogeneity in zircon 91500 *Chemical Geology 233(3-4):* 358-363.

Halpin J A Gerakiteys C L Clarke G L Belousova E A and Griffin W L 2005 In-situ U-Pb geochronology and Hf isotope analyses of the Rayner Complex, east Antarctica *Contributions to Mineralogy and Petrology 148:* 689-706.

Halpin J A Crawford A J Direen N G Coffin M F Forbes C J and Borissova I 2008 Naturaliste Plateau, offshore Western Australia: a submarine window into Gondwana assembly and breakup *Geology 36:*807-810.

Halpin J A 2011 Sample photos taken on board RV Southern Surveyor personal communication 12Nov2011.

Halpin J Daczko N R Milan L A and Clarke G L 2012 Decoding near-concordant U-Pb zircon ages spanning several hundred million years: recrystallisation, metamictisation or diffusion? *Contributions to Mineralogy and Petrology 163:* 67-85.

Henry D J Guidotti C V and Thomson J A 2005 The Ti-saturation surface for low-to medium pressure metapelitic biotites: Implications for geothermometry and Ti-Substitution mechanisms *American Mineralogist 90(2-3):* 316-328 http://www.geol.lsu.edu/henry/Research/biotite/TiInBiotiteGeothermometer.htm (02May12).

Hofmann A E Valley J W Watson E B Cavosie A J and Eiler J M 2009 Sub-micron scale distributions of trace elements in zircon *Contributions to Mineralogy and Petrology 158:*317-335.

Hoskin P W O and Schaltegger U 2003 The composition of zircon and igneous and metamorphic petrogenesis *Reviews in Mineralogy and Geochemistry 53(1):27062.*

Hu Z and Gao S 2008 Upper crustal abundances of trace elements: a revision and update *Chemical Geology 253:*205-221.

Jackson S E Pearson N J Griffin W L and Belousova E A 2004 The application of laser ablation -inductively coupled plasma-mass spectrometry to in situ U-Pb zircon geochronology *Chemical Geology 211(1-2):* 47-69.

Janousek V Farrow C M and Erban V 2006 Interpretation of whole-rock geochemical data in igneous geochemistry: Introducing Geochemical Data Toolkit (GCDkit) *Journal of Petrology 47:*1255-1259. http://www.gcdkit.org/ (13Apr2012).

Leak B E Woolley A R Arps C E S Birch W D Gilbert M C Grice J D Hawthorne F C Kato A Kisch H J Krivovichev V G Linthout K Laird J Mandarino J A Maresch W V Nickel E H Rock N M S Schumacher J C Smith D C Stephenson N C N Ungaretti L Whittaker E J W Guo Y 1997 Nomenclature of amphiboles: report of the subcommittee on amphiboles of the International Mineralogical Association, commission on new minerals and mineral names *The Canadian Mineralogist 35:*219-246.

Ludwig K R 2008 Isoplot V3.71 A geochronological toolkit for Microsoft Excel Berkeley Geochonology Center, Berkeley, California USA http://www.bgc.org/isoplot_etc/ isoplot.html (22May2012).

Martin T 2011 Personal communication (7Nov2011).

Meert J G 2002 A synopsis of events related to the assembly of eastern Gondwana *Tectonophysics 6800:* 1-40.

Middlemost E A K 1994 Naming materials in the magma/igneous rock system *Earth-Science Reviews 37:* 215-224.

Morimoto N Fabries J Ferguson A K Ginzburg I V Ross M Siefert F A Zussman J Aoki K Gottardi G 1988 Nomenclature of pyroxenes *American Mineralogist 73:*1123-1133.

Müller R D 2010 Tectonics: sinking continents *Nature Geoscience 3:*79-80.

Nelson D R Myers J S and Nutman 1995 Chronology and evolution of the Middle Proterozoic Albany-Fraser orogen, Western Australia *Australian Journal of Earth Sciences 42:* 481-495.

Passchier C W and Trouw R A J 1996 *Microtectonics* Springer-Verlag, Berlin.

Pearce J 1996 Sources and settings of granitic rocks *Episodes 19(4):120-125.*

Raase P 1974 Al and Ti contents of hornblende, indicators of pressure and temperature of regional metamorphism *Contributions to Mineralogy and Petrology 45(3):*231-236.

Rollinson H 1993 *Using geochemical data: evaluation presentation interpretation* Longman Scientific and Technical Essex, England UK 352 pp.

Rubatto D and Hermann J 2007 Zircon behaviour in deeply subducted rocks *Elements 3:*31-35.

Rudnick R L and Gao S 2003 Composition of the continental crust in *Treatise On Geochemistry 3:*1-64.

Scherer E Münker C Mezger K 2001 Calibration of the Lutetium-Hafnium clock *Science 293(5530):* 683-687.

Scherer E E Whitehouse M J and Münker C 2007 Zircon as a monitor of crustal growth *Elements 3:*19-24.

Speer J A (1982) Zircon in *Volume 5: Orthosilicates* 2nd Ed Ribbe P Mineralogical Society of America: 67-112.

Vansutre S and Hari K R 2010 Granulite belts of Central India with special reference to the Bhopalpatnam Granulite Belt: significance in crustal evolution and implications for Columbia supercontinent *Journal of Asian Earth Sciences 39:* 794-803.

Vernon R 2004 *A Practical Guide to Rock Microstructure* Cambridge University Press New York USA 594 pp.

Vernon R H and Clarke G L 2008 *Principles of Metamorphic Petrology* Cambridge University Press New York USA 446 pp.

Wiedenbeck M Hanchar J M Peck W H Sylvester P Valley J Whitehouse M Kronz A Morishita Y Nasdala L Fiebig J Franchi I Girard J-P Greenwood R C Hinton R Kita N Mason P R D Norman M Ogasawara M Piccoli P M Rhede D Satoh H Schulz-Dobrick B Skar O Spicuzza M J Terada K Tindle A Togashi S Vennermann T Xie Q and Zheng Y-F 2004 Further characterisation of the 91500 zircon crystal *Geostandards and Geoanalytical Research 28(1):* 9-39.

Williams S 2012 Voyage Summary for SS2011_06 personal communication 26Mar2012 (to be available at: www.marine.csiro.au/nationalfacility/voyagedocs/2011).

Wilson S A 1997 Data compilation for USGS reference material BHVO-2, Hawaiian Basalt *U.S. Geological Survey* http://crustal.usgs.gov/geochemical_reference_standards/basaltbhvo2.html#recommended (9Apr2012).

Wilson S A 1997b The collection, preparation and testing of USGS reference material BCR-2, Columbia River Basalt *U.S. Geological Survey* http://crustal.usgs.gov/geochemical_reference_standards/basaltbcr2.html#bibliography (4June2012).

Winter J D 2001 Principles of Igneous and Metamorphic Petrology 2nd Ed. Pearson Prentice Hall, New Jersey USA, 702pp.

Woodhead J D and Hergt J M 2007 A preliminary appraisal of seven natural zircon reference materials for in situ Hf isotope determination *Geostandards and Geoanalytical Research 29(2):* 183-195.

APPENDIX A ABBREVIATIONS

Af	Afif Terrane (Arabian-Nubian Shield)	MP	Maud Province
AFB	Albany-Fraser Belt	NBS	Nabitah Suture
BH	Bunger Hills	NC	Napier Complex
BR	Bongolava-Ranotsara shear zone	ND	Najd fault
BS	Betsimisaraka suture zone	nPCSM	Northern Prince Charles Mountains
DB	Damara Belt	NQ	Namaqua Belt
DDS	Darling-Denman suture	OSH	Onib-Sol Hamed suture
DG	Denman Glacier	PBB	Prydz Bay Belt
DMS	Dronnning Maud suture	PC	Paughat-Cauvery
EG	Eastern Ghats	SB	Saldania Belt
GB	Gariep Belt	SR	Shachelton Range
HC	Highland Complex	UAA	Urd Al Amar suture
LA	Lufilian Arc	VC	Vijayan Complex
LG	Lambert Glacier	WC	Wanni Complex
LHB	Lützow-Holm Belt	WI	Windmill Islands
MD	Mwembeshi Dislocation	ZB	Zambezi Belt

Table Appx-1: Abbreviations used in Figure 2-3 (Meert, 2002)

AAP	Argo Abyssal Plain	NP	Naturaliste Plateau
B	Batavia Knoll	PAP	Perth Abyssal Plain
CAP	Cuvier Abyssal Plain	WB	Wharton Basin
EP	Exmouth Plateau	WP	Wallaby Plateau
G	Gulden Draak	ZP	Zenith Plateau
GAP	Gascoyne Abyssal Plain		

Table Appx-2: Abbreviations used in Figure 2-4 (Gibbons et al., 2012)

Amph	Amphibole	Grt	Garnet
Ap	Apatite	Haem	Haematite
Aug	Augite	Kfsp	K-Feldspar
Bt	Biotite	Monz	Monazite
Chl	Chlorite	Opx	Orthopyroxene
Cpx	Clinopyroxene	Plag	Plagioclase
Diop	Diopside	Qtz	Quartz

Table Appx-3: Abbreviations used Figures in Chapters 4&5

APPENDIX B DR3 SAMPLE LIST

Sample #	Lithology	Thin section	XRF	Zircon dating	Notes
DR3-1	Orthogneiss cobble	Y	Y	Y	Cobble ~40cm across, coarse+fine-grained patches
DR3-2	Orthogneiss	Y	Y	Y	interpreted basement
DR3-3	Granite gneiss	Y			
DR3-4	Orthogneiss cobble	Y			Cobble ~15cm across
DR3-5	Granite (ksp-rich, fine-grained)	Y			
DR3-6	Orthogneiss cobble	Y	Y	Y	Cobble ~20cm across
DR3-7	Altered granodiorite(?) gneiss	Y			
DR3-8	Granite (qtz-rich)				
DR3-9	Clay-altered siltstone(?) or granite(?)				
DR3-10	Clay-altered siltstone(?) or granite(?)				
DR3-11	Red sandstone				
DR3-12	Purple-clay altered (?)basalt				
DR3-13	Purple-clay altered (?)basalt				
DR3-14	Felsic gneiss	Y			epidote+qtz?, stongly foliated and lineated
DR3-15	Garnet-sillimanite-biotite gneiss	Y	Y	Y	Giant boulder ~1m wide, broken up, interpreted basement
DR3-16	Weathered biotite gneiss	Y			
DR3-17	Weathered biotite gneiss				
DR3-18	Yellow-brown finely laminated sand-silstone				
DR3-19	Yellow-brown sandstone				Includes rip-up clasts
DR3-20	Yellow-brown sandstone				
DR3-21	Grey-brown siltstone				
DR3-22	Turbidite				Sand-silt layers, sand similar to DR3-23, silt mauve-brown
DR3-23	Biotite-rich sandstone				
DR3-24	Biotite-rich sandstone				
DR3-25	Biotite-rich sandstone				
DR3-26	Yellow-brown fossiliferous sandstone				

Table Appx-4: DR3 sample list

APPENDIX C WHOLE ROCK

CHEMISTRY CALCULATION FOR DR3-2

	Measured DR3-2	Calculated DR3-2 mineral averages					Calculated average DR3-2 rock
		Plag	Qtz	K-fsp	Bt	Op	
SiO_2	89.78	60.41	99.63	63.12	36.21	0.07	67.84
TiO_2	0.09	0.01	0.02	0.01	3.10	5.35	0.38
Al_2O_3	4.92	24.45	0.01	18.55	15.80	0.05	15.82
Fe_2O_3	0.67	0.07	0.03	0.04	19.48	85.75	2.85
MnO	<LLD	0.01	0.02	0.01	0.27	0.02	0.04
MgO	< 0.01	0.00	0.01	0.00	11.09	<LLD	1.11
CaO	0.33	6.20	<LLD	0.12	0.03	0.01	2.51
Na_2O	< 0.02	8.34	0.01	0.85	0.10	0.01	3.55
K_2O	1.76	0.14	<LLD	15.30	9.57	0.01	4.69
P_2O_5	0.12	0.10	0.02	0.07	0.01	<LLD	0.06
SO_3	0.029						
Total	97.696	99.73	99.74	98.09	95.66	91.28	98.85
Mode		40%	25%	24%	10%	1%	

Table Appx-5: Data for calculation of DR3-2 whole rock major oxide concentrations

SAMPLE MINERAL MODES

	DR3-1	DR3-2 (calc)	DR3-6	DR3-15
Plagioclase	5	40	10	25
K-Feldspar	50	24	43	12
Quartz	40	25	40	30
Biotite		10		5
Opaques	5	1	7	1
Garnet				12
Pinite				15
Total	100	100	100	100

Table Appx-6: Sample mineral modes

WHOLE ROCK ANALYSIS: MINOR ELEMENTS

Element	units	BHVO-2	BHVO-2 published*		BCR-2	BCR-2 published#		LLD
			Value	sd		Value	sd	
V	µg/g	327	317	11	442.9			1
Cr	µg/g	311.7	280	19	< 1.6	18	2	0.3
Mn	µg/g	1281	1290	40	1452	1520	60	
Fe	%	8.633	8.63	0.14	9.307	9.66	0.15	
Co	µg/g	41	45	3	34.6	37	3	0.4
Ni	µg/g	115.5	119	7	11.6			0.3
Cu	µg/g	128.5	127	7	19.4	19	2	0.3
Zn	µg/g	98.2	103	6	123.3	127	9	0.3
Ga	µg/g	20.4	21.7	0.9	23.6	23	2	0.3
Ge	µg/g	< 0.3			0.7			0.2
As	µg/g	< 0.3			1.6			0.3
Se	µg/g	< 0.2			< 0.2			0.2
Rb	µg/g	8.9	9.8	1	47.6	48	2	0.3
Sr	µg/g	390.7	389	23	341.5	346	14	0.2
Y	µg/g	26.6	26	2	35.9	37	2	0.2
Zr	µg/g	165.5	172	11	181.1	188	16	0.2
Nb	µg/g	16.6	18	2	10.9			0.2
Mo	µg/g	3.7			200.1	248	17	0.2
Ag	µg/g	< 0.8			< 0.8			
Cd	µg/g	0.5			0.4			0.2
Sn	µg/g	1.7	1.9	0.4	1.9			0.4
Sb	µg/g	< 0.5			< 0.5			0.5
Te	µg/g	< 0.2			< 0.2			1
Cs	µg/g	< 1.5			< 1.5	1.1	0.1	1.5
Ba	µg/g	129.7	130	13	689	683	28	1.5
La	µg/g	11.6	15	1	21.9	25	1	2
Ce	µg/g	32.5	38	2	44.5	53	2	3
Pr	µg/g	< 5.0			14	6.8	0.3	
Nd	µg/g	22.4	25	1.8	33.3	28	2	
Hf	µg/g	< 2.0	4.1	0.3	3.3	4.8	0.2	2
Ta	µg/g	< 2.0	1.4		< 2.0			
Tl	µg/g	< 0.7			< 0.7			0.7
Pb	µg/g	< 0.5			8	11	2	0.2
Bi	µg/g	< 0.5			< 0.5			0.5
Th	µg/g	< 0.5	1.2	0.3	4.9	6.2	0.7	0.5
U	µg/g	< 0.5			< 0.5	1.69	0.19	0.5

Table Appx-7: Whole rock analyses of minor elements in BHVO-2 and BCR-2 standards (*Wilson 1997, #Wilson,1997b)

Element	units	DR3-1	DR3-2	DR3-6	DR3-15
V	µg/g	9.8	10	< 4.7	120.8
Cr	µg/g	11.1	8.5	< 1.6	179.2
Mn	µg/g	208.8	158.1	68.3	418.8
Fe	%	2.053	1.031	1.677	3.739
Co	µg/g	106.5	68.8	56.2	76.7
Ni	µg/g	< 0.8	< 0.8	9.9	22.6
Cu	µg/g	9.4	3.8	1.9	38.3
Zn	µg/g	39.6	< 0.4	23.2	25.1
Ga	µg/g	23.7	15.6	25.5	18.8
Ge	µg/g	8.1	1.9	1.4	4.3
As	µg/g	2.5	< 0.3	1.7	1.4
Se	µg/g	0.9	1.1	0.6	0.4
Rb	µg/g	125.4	209.8	186.3	129.4
Sr	µg/g	50.6	289.1	78.8	78.7
Y	µg/g	52.9	14.8	43.4	28.2
Zr	µg/g	542.2	156.4	582.6	164.1
Nb	µg/g	15.2	5	29.5	8.1
Mo	µg/g	2.8	0.5	4.6	0.9
Ag	µg/g	< 0.8	< 0.8	< 0.8	< 0.8
Cd	µg/g	< 0.2	< 0.2	< 0.2	< 0.2
Sn	µg/g	1.1	1.9	0.4	1.7
Sb	µg/g	< 0.5	< 0.5	< 0.5	< 0.5
Te	µg/g	< 0.2	< 0.2	< 0.2	< 0.2
Cs	µg/g	1.3	3.5	< 1.5	1.8
Ba	µg/g	825.3	1002	458	605.9
La	µg/g	68.9	66.2	222.6	35
Ce	µg/g	134.7	122	412.5	61
Pr	µg/g	7	< 5.0	56	7.5
Nd	µg/g	50.8	43.7	150.6	20.1
Hf	µg/g	9.7	< 2.0	13.6	< 2.0
Ta	µg/g	< 2.0	6	9.3	< 2.0
Tl	µg/g	4	5.4	2.4	< 0.7
Pb	µg/g	10.1	44.6	21.7	14.3
Bi	µg/g	0.6	1.1	0.7	< 0.5
Th	µg/g	6.2	49.1	32.7	14.4
U	µg/g	< 0.5	< 0.5	< 0.5	< 0.5

Table Appx-8: Whole rock analyses of minor elements in dredged samples

APPENDIX D HAFNIUM %RSD

Sample/Group			Core						Rim					
			Count	HfO_2	SiO_2	ZrO_2	Y_2O_3	Total	Count	HfO_2	SiO_2	ZrO_2	Y_2O_3	Total
DR3-1	Grp 1	mean	53	1.47	31.41	64.95	0.29	98.11	11	1.47	31.49	65.54	0.12	98.63
		std dev		0.21	1.41	2.47	0.49	3.51		0.19	2.15	2.12	0.06	4.34
		rsd %		14.04	4.49	3.80	168.02	3.58		13.04	6.84	3.24	51.01	4.40
	Grp 2	mean	10	1.55	32.14	66.15	0.14	99.98	1					
		std dev		0.08	0.15	0.39	0.08	0.35						
		rsd %		5.06	0.46	0.58	58.03	0.35						
DR3-2	Grp 1	mean	19	1.64	30.84	64.59	0.28	97.36						
		std dev		0.09	1.90	2.79	0.38	4.34						
		rsd %		5.49	6.16	4.32	134.85	4.46						
	Grp 2	mean	50	1.63	30.42	63.50	0.33	95.87	7	1.72	31.44	65.49	0.22	98.87
		std dev		0.34	4.62	9.45	0.40	14.24		0.32	0.93	1.19	0.18	1.78
		rsd %		20.66	15.18	14.89	123.53	14.86		18.42	2.96	1.82	79.75	1.80
	Grp 3	mean	17	1.60	30.69	63.96	0.45	96.70	7	1.73	31.81	65.98	0.13	99.65
		std dev		0.23	2.49	4.12	0.63	6.02		0.23	0.40	0.78	0.07	1.05
		rsd %		14.21	8.12	6.45	139.59	6.23		13.37	1.26	1.19	52.45	1.05
DR3-6	Grp 1	mean	26	2.20	31.31	63.55	0.48	97.54	22	1.70	32.07	65.97	0.20	99.93
		std dev		0.97	1.10	1.79	0.32	1.89		0.18	0.37	0.63	0.13	0.88
		rsd %		44.22	3.53	2.82	66.88	1.94		10.59	1.14	0.96	66.01	0.88
	Grp 2	mean	42	1.45	32.19	66.00	0.34	99.98	20	1.76	32.21	65.85	0.20	100.02
		std dev		0.20	0.30	0.98	0.18	1.18		0.28	0.54	0.92	0.25	1.07
		rsd %		13.81	0.92	1.49	53.12	1.18		15.75	1.69	1.40	124.06	1.07
	Grp 3	mean	20	1.61	32.07	65.22	0.21	99.11	5	1.75	32.27	66.07	0.16	100.25
		std dev		0.26	0.66	2.12	0.17	2.64		0.40	0.29	0.32	0.06	0.57
		rsd %		15.99	2.05	3.25	82.69	2.66		23.11	0.91	0.48	40.05	0.56
	Grp 4	mean	6	1.61	32.19	66.22	0.24	100.26						
		std dev		0.16	0.24	0.48	0.09	0.58						
		rsd %		9.82	0.76	0.72	38.14	0.58						
	Grp 5	mean	8	1.49	32.09	66.06	0.17	99.81	2	1.63	32.45	66.51	0.14	100.73
		std dev		0.21	0.57	1.38	0.11	1.63		0.06	0.06	0.09	0.08	0.13
		rsd %		14.34	1.76	2.09	65.66	1.63		3.73	0.19	0.14	60.10	0.13
DR3-15	Grp 1	mean	48	1.57	28.79	62.42	1.30	94.08						
		std dev		0.12	2.87	3.41	1.19	5.03						
		rsd %		7.83	9.98	5.46	91.57	5.35						
	Grp 2	mean	69	1.40	30.18	63.54	0.85	95.97	16	1.57	27.85	61.07	1.68	92.17
		std dev		0.19	2.56	3.68	0.97	5.12		0.08	2.65	3.25	1.19	4.80
		rsd %		13.84	8.50	5.80	114.10	5.34		5.07	9.52	5.33	70.61	5.21
	Grp 3	mean	60	1.56	29.71	62.68	0.99	94.95	7	1.56	27.59	60.28	1.78	91.22
		std dev		0.16	2.73	3.85	1.05	5.32		0.07	4.06	5.10	0.92	8.17
		rsd %		10.23	9.19	6.14	105.69	5.60		4.69	14.72	8.46	51.37	8.96

Key:

rsd % variation	
<25%	Minor
<100%	Moderate
>100%	Extensive

Table Appx-9: EMP data: Y and Hf variation in morphological groups